NONLINEAR DYNAMICAL ANALYSIS IN MAGNETIC HYPERTHERMIA

Filipe Eduard Leite Ossege

Master's Dissertation
Mechanical Sciences

UNIVERSITY OF BRASÍLIA

Faculty of Technology
Department of Mechanical Engineering

ANÁLISE DINÂMICA NÃO-LINEAR EM MAGNETOHIPERTERMIA

Filipe Eduard Leite Ossege

Dissertação de Mestrado

Ciências Mecânicas

UNIVERSIDADE DE BRASÍLIA

Faculdade de Tecnologia

Departamento de Engenharia Mecânica

UNIVERSIDADE DE BRASÍLIA
FACULDADE DE TECNOLOGIA
DEPARTAMENTO DE ENGENHARIA MECÂNICA

NONLINEAR DYNAMICAL ANALYSIS IN MAGNETIC HYPERTHERMIA

Filipe Eduard Leite Ossege

Orientadora: Profa. Dra. Aline Souza de Paula (ENM/UnB)
Coorientador: Prof. Dr. Rafael Gabler Gontijo (ENM/UnB)

DISSERTAÇÃO DE MESTRADO

BRASÍLIA/DF: 06 de fevereiro de 2023

UNIVERSIDADE DE BRASÍLIA
FACULDADE DE TECNOLOGIA
DEPARTAMENTO DE ENGENHARIA MECÂNICA

Nonlinear Dynamical Analysis in Magnetic Hyperthermia

Filipe Eduard Leite Ossege

DISSERTAÇÃO DE MESTRADO SUBMETIDA AO DEPARTAMENTO DE
ENGENHARIA MECÂNICA DA FACULDADE DE TECNOLOGIA DA
UNIVERSIDADE DE BRASÍLIA COMO PARTE DOS REQUISITOS NECESSÁRIOS
PARA A OBTENÇÃO DO GRAU DE MESTRE EM CIÊNCIAS MECÂNI-
CAS.

APROVADA POR:

_____

Profa. Dra. Aline Souza de Paula (ENM/UnB)
(Orientadora)

_____

Prof. Dr. Marcelo Amorim Savi (COOPE/UFRJ)
(Examinador Externo)

_____

Prof. Dr. Yuri Dumaresq Sobral (IE/UnB)
(Examinador Externo)

BRASÍLIA/DF, 06 DE FEVEREIRO DE 2023.

FICHA CATALOGRÁFICA

Ossege, F. E. L.
Nonlinear Dynamical Analysis in Magnetic Hyperthermia
[Distrito Federal] 2023.
  xxviii, 103p. (ENM/FT/UnB, Mestre, Ciências Mecânicas, 2023.
  Dissertação de Mestrado - Universidade de Brasília.
  Faculdade de Tecnologia.
  Departamento de Engenharia Mecânica.
Palavras-chave:

1. Magnetic Hyperthermia	2. Particulate System
3. Dynamical Analyzis	4. Nonlinear System
I. ENM/FT/UnB	II. Título (série)

REFERÊNCIA BIBLIOGRÁFICA

CESSÃO DE DIREITOS

NOME DO AUTOR: Filipe Eduard Leite Ossege.

TÍTULO DA DISSERTAÇÃO DE MESTRADO: Nonlinear Dynamical Analysis in Magnetic Hyperthermia.

GRAU / ANO: MESTRE / 2023

_____

Filipe Eduard Leite Ossege

À minha irmã, Carol, e à minha esposa, Gláucia,
minhas eternas companheiras de vida.

Agradecimentos

Gostaria de agradecer à minha querida irmã, Carol. Engraçado pensar que, no começo da nossa infância, a gente brigava muito. Com o passar dos anos, Carol se tornou minha melhor amiga e me ajudava, sem exagero, em todas as áreas da minha vida. Carol me adiantou conteúdo de matemática, me ensinando divisão com frações antes que meu professor da escola. Me ajudou durante a adolescência, quando saímos de casa e dividimos o mesmo quarto durante 4 anos. Me ensinou a cuidar do nosso pai idoso, tendo paciência em me orientar como fazer as tarefas de casa. Enfrentamos a pandemia de COVID-19 juntos e conseguimos proteger nosso pai. Adotamos uma cachorrinha de rua chamada Sol para cuidarmos juntos. Minha irmã, obrigado por me acompanhar durante toda a minha existência.

Agradeço muito à minha esposa, Gláucia. Nossa relação sempre foi marcada por muito apoio, carinho, compreensão e brincadeiras (provavalmente a única pessoa que aguenta as minhas loucuras). Obrigado por me fazer acreditar no amor novamente. Que nosso casamento seja sempre baseado em uma boa comunicação, gentileza e sinceridade. Wir passen perfekt zusammen.

Quero agradecer à minha mãe, Albany, por ter me ensinado disciplina e rigor para cumprir minhas tarefas. Você sempre batalhou para oferecer uma educação de qualidade para mim e eu não teria chegado aqui sem a sua ajuda. Um agradecimento também ao meu pai, Franz, por ter me ensinado a ser humilde e simples com todas as pessoas.

Gostaria de agradecer à minha orientadora Aline Souza de Paula pelos acompanhamentos e pelo apoio, tanto academicamente quanto pessoalmente. Lembro-me da primeira vez que encontrei a professora Aline, na disciplina Vibrações 1. Na aula, as fórmulas apareciam como se fosse um passo de mágica e a Aline, com uma didática excepcional, foi sempre bem receptiva a qualquer dúvida dos alunos. Então, decidi pedir à professora uma iniciação científica. Por sorte, estávamos no final do período de inscrição e eu consegui o projeto. Aline, obrigado por ser um exemplo de professora. Em um mundo acadêmico onde muitos colegas reclamam de relações tóxicas com os orientadores, posso ter o privilégio de dizer que minha relação com você é extremamente saudável e que me impulsiona a continuar na carreira acadêmica. Caso um dia eu consiga ser um pesquisador com metade da sua dedicação e didática, eu já vou me considerar um profissional bem-sucedido.

Quero agradecer também ao meu coorientador Rafael Gabler Gontijo, por fazer

"Our journey may have been meaningless.
Our past may have been a mistake.
But, we're not going back.
Even if this world comes to an end.
Because this... This is the world with the people we cherish."
Kainé and Emil - NieR Replicant ver.1.22474487139...

Abstract

NONLINEAR DYNAMICAL ANALYSIS IN MAGNETIC HYPERTHERMIA

Author: Filipe Eduard Leite Ossege

Supervisor: PhD Aline Souza de Paula (ENM/UnB)

Co-supervisor: PhD Rafael Gabler Gontijo (ENM/UnB)

Graduate Program in Mechanical Sciences

Brasília, February 06, 2023

Magnetic hyperthermia is a cancer treatment based on heating tumors using ferrofluids. Motivated by this therapy, this work evaluates different nonlinear dynamical responses seeking the better performance in terms of temperature increase. Through a system with 250 lattices with 300 particles each, a ferrofluid is simulated numerically under several circumstances. Due to the random effect, 50 realizations of the same system are applied and average time response is obtained. Three different excitation are applied: pure alternating magnetic field, alternating magnetic field with alternating shear rate and pure chaotic magnetic field. In the case of pure alternating magnetic field, system response is evaluated for different values of the Péclet number, volume fraction, Langevin parameter, dipolar interaction parameter and magnetic field's angular frequency. The best situation is associated with a more intense magnetic field. In the case of alternating magnetic field with alternating shear motion, the shear rate's amplitude and angular frequency are the varied parameters. The results indicate that the shear motion brings no benefits for magnetic hyperthermia. In the case of pure chaotic magnetic field, system response is evaluated for different values of the Langevin parameter. From the 3 excitations considered, the pure alternating magnetic field produced the best dynamical behavior for this cancer treatment. It is also important to highlight that, beyond the goal of temperature increase, this work brings a better understanding of dynamical response of FF's in MH.

Keywords: Magnetic Hyperthermia; Particulate System; Dynamical Analyzis; Nonlinear System

Resumo

ANÁLISE DINÂMICA NÃO-LINEAR EM MAGNETOHIPERTERMIA

Autor: Filipe Eduard Leite Ossege

Orientadora: Profa. Dra. Aline Souza de Paula (ENM/UnB)

Coorientador: Prof. Dr. Rafael Gabler Gontijo (ENM/UnB)

Programa de Pós Graduação em Ciências Mecânicas

Brasília, 06 de fevereiro de 2023

Magnetohipertermia é um tratamento de câncer baseado no aquecimento de tumores usando ferrofluidos. Motivado por essa terapia, esse trabalho avalia diferentes respostas dinâmicas não-lineares, a fim de aprimorar seu desempenho em termos do aumento de temperatura. Através de um sistema com 250 caixas com 300 partículas cada, um ferrofluido é simulado numericamente sob diversas circunstâncias. Devido ao efeito randômico, 50 realizações do mesmo sistema são aplicadas e a resposta temporal média é obtida. Três forçamentos distintos são aplicados: campo magnético alternado puro, campo magnético alternado com cisalhamento alternado e campo magnético caótico puro. Para o caso do campo magnético alternado puro, a resposta do sistema foi avaliada para diferentes valores do número de Péclet, da concentração de partículas, do parâmetro de Langevin, do parâmetro de interação dipolar e da frequência angular do campo magnético. A melhor situação obtida está associada a um campo magnético mais intenso. Para o caso do campo magnético alternado com cisalhamento alternado, a amplitude e a frequência angular da taxa de cisalhamento são os parâmetros variados. Os resultados indicam que o cisalhamento não traz benefícios para a magnetohipertermia. Para o caso do campo magnético caótico, o paramêtro de Langevin é avaliado. Dos três forçamentos considerados, o campo magnético alternado puro é o comportamento mais apropriado para esse tratamento de câncer. É importante destacar que, além do objetivo de aumentar a temperatura, esse trabalho permite um melhor entendimento da resposta dinâmica de ferrofluidos em magnetohipertermia.

Palavras-chaves: Magnetohipertermia; Sistema Particulado; Análise Dinâmica; Sistema

Não-linear.

Summary

List of Figures

List of Tables

Acronyms

FF Ferrofluid. viii, 2–6, 10, 11, 44

MH Magnetic Hyperthermia. viii, 1–6, 21, 23, 51, 70, 86, 87

MNP Magnetic Nanoparticles. xiv, 2, 3, 6, 8–12, 17–19, 24, 29, 62, 80, 86

NASA National Aeronautics and Space Administration. 2

Nomenclature

Mathematical Notation

Symbol	Description	Unit or value used in this work
M	Scalar quantity	$\mathrm{A\,m^{-1}}$
M^*	Dimensionless quantity	Dimensionless
$|M|$	Absolute value of M	$\mathrm{A\,m^{-1}}$
$[M]$	Scalar measure of M (Poincaré map of M)	$\mathrm{A\,m^{-1}}$
$\mathbf{M}$	Vector quantity	$\mathrm{A\,m^{-1}}$
$\|\mathbf{M}\| = M$	Modulus of $\mathbf{M}$ (euclidian norm of $\mathbf{M}$)	$\mathrm{A\,m^{-1}}$
$\hat{\mathbf{M}}$	Unit vector at the direction of $\mathbf{M}$	Dimensionless
$\dot{M} = \dfrac{\mathrm{d}M}{\mathrm{d}t}$	Total derivative of M with respect to time	$\mathrm{A\,m^{-1}\,s^{-1}}$
$\dfrac{\partial M}{\partial x}$	Partial derivative of M with respect to the variable x	Depends of x
∇	Gradient operator	$\mathrm{m^{-1}}$
∇^*	Dimensionless gradient operator	Dimensionless
$\nabla_{\hat{\mathbf{d}}_i}$	Gradient operator with derivatives with respect to the dipole orientation of the i-th particle	Dimensionless
$\times$	Cross product	
$\cdot$	Inner product	

Coordinate Systems

$\hat{\mathbf{x}}, \hat{\mathbf{y}}, \hat{\mathbf{z}}$	Cartesian coordinates	Dimensionless
M_x, M_y, M_z	$\hat{\mathbf{x}}$, $\hat{\mathbf{y}}$ and $\hat{\mathbf{z}}$ components of the vector $\mathbf{M}$	$\mathrm{A\,m^{-1}}$
O	Origin of the coordinate system	m

Latin Symbols

a	Hydrodinamic radius of a single magnetic particle	m
$\mathbf{B}$	Induction vector field	$\mathrm{N\,A^{-1}\,s^{-1}}$
$\mathcal{B}$	Scalar function of the periodic lattices simulation	Dimensionless
b	Parameter for the calibration of the contact force between particles	m
C_1	Calibration constant of the repulsive force related to intensity of the field	Dimensionless
C_2	Calibration constant of the repulsive force related to range of the field	m
C_3	Calibration constant of the contact force	Dimensionless
C_4	Calibration constant of the dimensionless contact force	Dimensionless
$\mathcal{C}$	Scalar function of the periodic lattices simulation	Dimensionless
c	Index representing the c-th cycle of the periodic external magnetic field, $\mathbf{H}$	Index
$\mathcal{D}_t$	Translational brownian diffusion coefficient of Stokes-Einstein	$\mathrm{m^2\,s^{-1}}$
$\mathcal{D}_r$	Rotational brownian diffusion coefficient of Stokes-Einstein	$\mathrm{m^2\,s^{-1}}$
$\hat{\mathbf{d}}_i$	Dipole orientation of the i-th particle	Dimensionless
$\mathrm{d}U$	Exact differential of the internal energy per unit volume	$\mathrm{J\,m^{-3}}$
E	Young modulus of particles	$\mathrm{N\,m^{-2}}$
$\mathrm{erfc}()$	Complementary error function	Dimensionless
$\mathbf{F}_{\mathbf{B}i}$	Brownian force applied to the i-th particle	N
$\mathbf{F}_{\mathbf{c}i}$	Contact force applied to the i-th particle	N
$\mathbf{F}_{\mathbf{m}i}$	Magnetic force applied to the i-th particle	N
$\mathbf{F}_{\mathbf{r}i}$	Repulsive force applied to the i-th particle	N
$\mathcal{F}\{\}$	Dimensionless Fourier transform	Dimensionless
$\mathbf{g}$	Gravitational vector field	$\mathrm{m\,s^{-2}}$

$\mathbf{H}$	External magnetic field	$\mathrm{A\,m^{-1}}$
h	Time step for the Runge-Kutta integration method	Dimensionless
$\mathcal{I}$	Moment of inertia of a single magnetic particle	$\mathrm{kg\,m^2}$
i	Index representing the i-th particle	Index
j	Index representing the j-th particle	Index
$\mathscr{J}$	Imaginary unit	$\sqrt{-1}$
K	Number of total realizations	50 (Index)
K_b	Boltzmann's constant	$1.38 \cdot 10^{-23}\,\mathrm{kg\,m^2\,s^{-2}\,K^{-1}}$
k	Index representing the k-th realization	Index
$\hat{\mathbf{k}}$	Wavenumber unit vector in the reciprocal domain	Dimensionless
$\mathbf{M}$	Magnetization vector	$\mathrm{A\,m^{-1}}$
$\mathbf{M}_k$	Magnetization vector for the k-th realization	$\mathrm{A\,m^{-1}}$
$\overline{\mathbf{M}}$	Mean value of the magnetization vector for all K realizations	$\mathrm{A\,m^{-1}}$
M_d	Spontaneous magnetization	$\mathrm{A\,m^{-1}}$
M_s	Saturation magnetization	$\mathrm{A\,m^{-1}}$
$\mathcal{M}$	Mass of a single magnetic particle	kg
m	Magnetic dipole intensity of a single magnetic particle	$\mathrm{A\,m^2}$
$\mathbf{m}_i$	Magnetic moment dipole vector of the i-th particle	$\mathrm{A\,m^2}$
$\overline{\mathbf{m}}$	Mean value of the magnetic moment dipole vector for all N particles	$\mathrm{A\,m^2}$
N	Number of total particles	300 (Index)
n	Density number	$\mathrm{m^{-3}}$
P_c	Parameter which quantify the relation between the contact force and hydrodynamic drag force	Dimensionless
Pe	Translational Peclet number	Dimensionless
Pe_r	Rotational Peclet number	Dimensionless
$\mathbf{r}_{ij}$	Distance vector between the centers of mass of the i-th and the j-th particles	m

$\hat{\mathbf{r}}_{ij}$	Unit vector of the distance between the centers of mass of the i-th and the j-th particles	Dimensionless
$\mathbf{r}_i$	Position vector of the center of mass of the i-th particle with respect to the origin	m
St	Translational Stokes number	0.1
St$_r$	Rotational Stokes number	0.01
T	Temperature	K
$\mathcal{T}$	Period of the magnetic field, $\mathbf{H}$	s
$\mathcal{T}_1(x)$	Function from the physical domain for periodic lattices.	Dimensionless
$\mathcal{T}_2(x)$	Function from the reciprocal domain for periodic lattices.	Dimensionless
$\mathbf{T}_{\mathbf{B}i}$	Brownian torque upon the i-th particle	N m
$\mathbf{T}_{\mathbf{m}i}$	Magnetic torque upon the i-th particle	N m
$\mathbf{T_{mp}}_i^*$	Dimensionless magnetic torque upon the i-th particle for periodic lattices simulations	Dimensionless
t	Time	s
t_f^*	Dimensionless final time of the simulation	Dimensionless
U_{st}	Particle's terminal velocity from Stokes' law	m s^{-1}
$\mathbf{u}_i$	Velocity of the i-th particle	m s^{-1}
$\mathbf{u_{sh}}_i$	Velocity of the i-th particle under shear motion	m s^{-1}
V	Total volume of the system (Ferrofluid's sample) or volume of the central cell.	m^3
V_p	Volume occupied by all particles.	m^3
v_i	Volume of the i-th magnetic nanoparticle	m^3

Greek Symbols

α	Langevin parameter	Dimensionless
$\dot{\gamma}$	Shear rate	s^{-1}
δQ	Inexact differential of the heat per unit volume	J m^{-3}
δW	Inexact differential of the work per unit volume	J m^{-3}

$\delta\tau$	Time step associated with brownian thermal fluctuations	s
ΔU	Total variation of internal energy per unit volume	$\mathrm{J\,m^{-3}}$
Δt	Total variation of time during the simulation	s
$\Delta U/\Delta t$	Average rate of change in internal energy per unit volume (production of internal energy per unit volume)	$\mathrm{J\,m^{-3}\,s^{-1}}$
$\Delta\rho$	Density difference between magnetic particles and fluid carrier	$\mathrm{kg\,m^{-3}}$
ϵ_{ij}	Distance between the surfaces of the i-th and the j-th particles	m
ε	Material constant of the contact force	Dimensionless
η	Dynamic viscosity of the liquid carrier	$\mathrm{Pa\,s}$
λ	Dipolar interaction parameter	Dimensionless
λ_c	Control parameter	Depends of λ_c
μ_0	Vacuum permeability	$1.26 \cdot 10^{-6}\,\mathrm{H\,m^{-1}}$
ν	Poisson's ratio of particles	Dimensionless
ξ	Convergence parameter of the periodic cells simulation.	Dimensionless
$\boldsymbol{\xi}$	Unitary random vector with uniform distribution	Dimensionless
π	Ratio of a circle's circumference to its diameter	3.1416
ρ_f	Density of the fluid carrier	$\mathrm{kg\,m^{-3}}$
ρ_s	Density of the magnetic particles	$\mathrm{kg\,m^{-3}}$
Σ	Poincaré section with reference to $\hat{\mathbf{H}}$ of the dynamical system in the phase space	
ϕ	Magnetic volume fraction	Dimensionless
ψ_{p_i}	Potential of the i-th particle due to dipole-dipole interactions	$\mathrm{N\,m}$
ψ_{f_i}	Potential of the i-th particle due to field-dipole interactions	$\mathrm{N\,m}$
ω_H^*	Dimensionless angular frequency of the dimensionless magnetic field	Dimensionless

ω_S^*	Dimensionless angular frequency of the dimensionless shear rate	Dimensionless
$\boldsymbol{\omega}_i$	Angular velocity vector of the i-th particle	$\mathrm{rad\,s^{-1}}$
$\boldsymbol{\omega}_{\mathbf{sh}i}$	Angular velocity vector of the i-th particle under shear motion	$\mathrm{rad\,s^{-1}}$

1 Introduction

In medicine, hyperthermia is a term which describes the treatment of tumors by increasing temperature in various ways (Hildebrandt et al., 2002). Normally, a biological tissue is heated above 40°C, as cancer growth is interrupted in high temperatures (Périgo et al., 2015). Hyperthermia is commonly used as a complementary method for cancer therapy, accompanied mostly by radiotherapy and chemotherapy (Hildebrandt et al., 2002). It is believed that the first use of hyperthermia was around 3,000 years B.C. (Périgo et al., 2015), as a papyrus of the ancient Egypt describes the treatment of breast cancer (Hajdu, 2011). Several procedures have been developed based on hyperthermia, such as radio-frequency, ultrasound irradiation and local thermal contact (Odenbach, 2009). According to Odenbach (2009), the main disadvantage of common hyperthermia methods are the side effects in healthy tissues, due to the high temperature.

The heating can also be achieved by magnetic means with Magnetic Hyperthermia (MH) or Magnetic Nanoparticle Hyperthermia, in which a biocompatible magnetic fluid is injected in the organic unhealthy tissue and subjected to a time dependent magnetic field (Liu et al., 2020). Due to hysteresis losses, the energy of the magnetic field is dissipated, increasing the temperature locally (Rosensweig, 2002), (Carrey; Mehdaoui; Respaud, 2011). MH presents fewer side effects in comparison with other hyperthermia methods, as the heating region can be controlled by the magnetic field (Thiesen; Jordan, 2008). Furthermore, MH is commonly used in combination with other treatments to increase efficacy. In a nanoscopic scale, a localized temperature rise is promoted by the action of an applied magnetic field in a continuum medium filled with magnetic particles. Present challenges of MH consist on increasing heating power and controlling the cancer temperature (Peiravi et al., 2022).

Some of the physical mechanisms associated with MH are the energy dissipation of the magnetic field; the blood perfusion rate, which varies depending on healthy and cancerous cells (Tang; Jin; Flesch, 2020); the densities of blood, healthy cells, cancerous cells; the thermal conductivity inside the organic tissue; the metabolic heat of healthy

cells and cancerous cells; the specific heat capacity; properties of the magnetic fluid and so on. The blood perfusion rate acts in MH maintaining the temperature of 36°C in the human body, cooling the effect of MH. But the multiplication of tumors cells affects the blood flow, which decreases the perfusion rate and its effect in the temperature. Because of this, it is easier to heat cancerous cells than healthy cells.

To apply the MH, a magnetic suspension is used, that is, a particle conglomerate dispersed in a liquid carrier (Gontijo; Cunha, 2015). Such suspensions are called either a magnetorheological suspension or a Ferrofluid (FF) (also know as magnetic fluid), depending on the magnetic particles' diameter (Gontijo, 2013). More specifically, magnetorheological suspensions have non-colloidal particles with typical size of 100 μm, whereas FFs are made with colloidal particles with typical size of 10 nm (ROURE NETO, 2018). Furthermore, FFs are considered smart nanomaterials whose particles are named Magnetic Nanoparticles (MNP) (Huang et al., 2017), (Coisson et al., 2017).

MH was first highlighted by Gilchrist et al. (1957), who conducted experiments of sickly beef livers under alternating magnetic field. At that time, magnetorheological suspensions were applied in the treatment. However, problems such as biocompatibility with the human body still persisted (Blanco-Andujar; Teran; Ortega, 2018). Later, the treatment was greatly improved by nanotechnology, as the magnetic particles' diameter became smaller and FF was created (Liu et al., 2020). Therefore, most of the problems regarding MH were solved and the method could be applied with human patients (Blanco-Andujar; Teran; Ortega, 2018).

The first FF was fabricated by Papell (1965), at the National Aeronautics and Space Administration (NASA), with the objective of creating a rocket fuel capable of being controlled by a magnetic field in zero gravity environments. In the composition of a FF, a surfactant envelops the MNPs to prevent such particles to agglomerate with each other due to the magnetic forces (Huang et al., 2017). According to Huang et al. (2017), the brownian random motion avoids the particle sedimentation when a gravitational or a magnetic field is applied. To exemplify the structure of a FF, Figure 1.1 shows a MNP, with its core and the additional layer provided by the surfactant. The common diameter of the magnetic core is 10 nm and the diameter considering the surfactant layer (also called hydrodynamic diameter) can reach 25 nm (Finlayson, 2013). Thus, a common size for the hydrodinamic radius is $a = 25/2$ nm $= 12.5$ nm.

Furthermore, in the early stages of the FF manufacture, wet grinding of magnetite (Fe_3O_4) mixed with surfactant was used, along with centrifugation (Sezer et al., 2021). As reported by the Sezer et al. (2021), such method demanded long periods of time and high amounts of energy, so that new processes were developed. For example, coprecipitation (Lee et al., 2004), thermal decomposition (Maity et al., 2009) and hydrothermal synthesis (Haw et al., 2010) were applied.

The MH method has shown potential, as it decreases the cancer's mass and increases
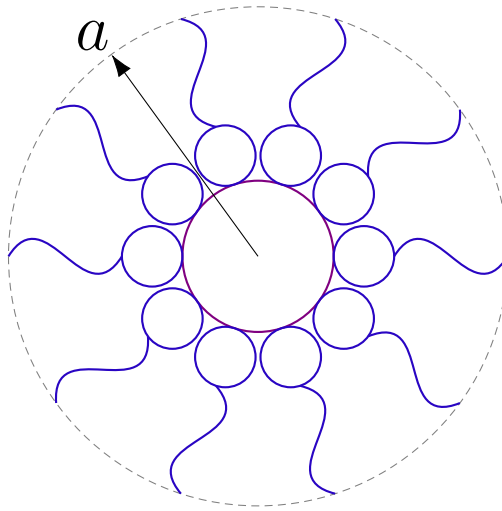
Figure 1.1 – Representation of a magnetic particle: magnetic core (in violet) and organic surfactant shell that prevents conglomeration (in blue), where a is the particle's hydrodynamic radius. Figure adapted from Arias et al. (2018).

the life expectancy of animals in experiments (Silva et al., 2010). For example, cancerous cells of mice under an alternating magnetic field with magnitude 30,6 kA/m and frequency 118 kHz have achieved a temperature of 46°C using magnetite particles (Ito et al., 2001). Concerning experiments with humans, cerebral tumors of male patients have reached a temperature of 65.6°C with a magnetic field with magnitude from 2.5 to 18 kA/m and frequency 100 kHz using iron oxide nanoparticles (Landeghem et al., 2009). The MH treatment has an edge, considering that is effective and minimally invasive and can destroy the cancer or detain its expansion (Silva et al., 2010).

The performance of the MH technique depends upon the increase of the FF's temperature. From a dynamical point of view, the temperature increase is associated with the particles agitation intensity. The collision of the MNPs under magnetic attraction and their dynamics can influence greatly the cancer treatment, thus, it is important to evaluate the dynamical response and understand its influence in the temperature variation.

1.1 State of the Art

The applications of FFs are separated by Sezer et al. (2021) in 4 groups: biomedical, environmental, energy and mechanical. Regarding the biomedical use, some implementations are drug delivery (Polyak; Friedman, 2009), hyperthermia in cancer therapy for lungs (Sadhukha; Wiedmann; Panyam, 2013), prostate (Johannsen et al., 2010), liver (Wang; Song; Zhang, 2009) and breast (Hilger; Hergt; Kaiser, 2005). In the medical area, compounds of maghemite ($\gamma-\mathrm{Fe_2O_3}$) and magnetite ($\mathrm{Fe_3O_4}$) are mostly utilized (Sezer et al., 2021), (Neuberger et al., 2005).

In relation to the environmental applications, FFs are used as a method of separating

mixtures, with the purpose of separating garbage from the ecosystem. To do so, one can identify magnetic separation (Nogueira et al., 2019) and adsorption (Kakavandi et al., 2015). Concerning the energy applications, magnetic fluids are used in energy harvesting systems (Bibo et al., 2012) and in heat transfer, such as in thermomagnetic convection (Nkurikiyimfura; Wang; Pan, 2013).

Regarding the mechanical applications, FFs are applied in dampers (Wang; Liu; Li, 2018), dynamic vibration absorbers (active (Ohno; Suzuki; Sawada, 2011), semi-active (Kondo; Ikari; Sawada, 2016) and passive (Zhu et al., 2015)), vibration isolators (active (Kamiyama; Okamoto; Oyama, 2002) and passive (Liu, 2009)) and lubrication (Huang et al., 2011). For this topic, the article of Huang et al. (2017) is recommended. In addition, there are others industrial applications of FFs in computer hard disks (Scherer; Neto, 2005), robotics (Hsu; Wong-Foy; Pelrine, 2018) and loudspeakers (Bottenberg; Melillo; Raj, 1980). For this subject, the article of Kole and Khandekar (2021) is recommended.

Concerning the dynamical analysis of FFs, the bifurcation of a superparamagnetic magnetic fluid has been investigated numerically using the eulerian description and linear stability analysis (Pérez et al., 2011). Chaotic behavior was identified in a system described by a gas bubble immersed in FF by means of Lyapunov exponent (Malvar; Gontijo; Cunha, 2018). The temperature profile of a FF under chaotic regime was investigated using bifurcation diagrams, Lyapunov exponents, phase space and Fourier power spectrum (Laroze; Siddheshwar; Pleiner, 2013).

1.2   Objectives

The main goal of this work is to perform a dynamical analysis of the system, linking its dynamical behavior with the highest production of internal energy. Lastly, the specific objectives are:

- Evaluate the dynamical response and the internal energy production for 3 different types of excitations:

  - Pure alternating magnetic field;
  - Alternating magnetic field with alternating shear rate;
  - Pure chaotic magnetic field.

- For each case, identify the parameters that most contribute for the internal energy production of the system, enhancing the MH;

- Identify the most appropriate behavior from the three excitation.

1.3   Methodology

To achieve the goals described in the Objectives, Fig. 1.2 shows the flowchart summarizing the methodology. For the first branch, through numerical simulation, an alternating magnetic field is applied. The time response of the system and its internal energy production are obtained and evaluated. Then, the best case for this excitation is determined. For the second branch, an alternating magnetic field along with alternating shear motion is applied, the response and internal energy are evaluated and the best case for this excitation is determined. For the third branch, a pure chaotic magnetic field is imposed, the response and internal energy are evaluated and the best case for this excitation is determined. Lastly, the best case from all three excitation is determined.
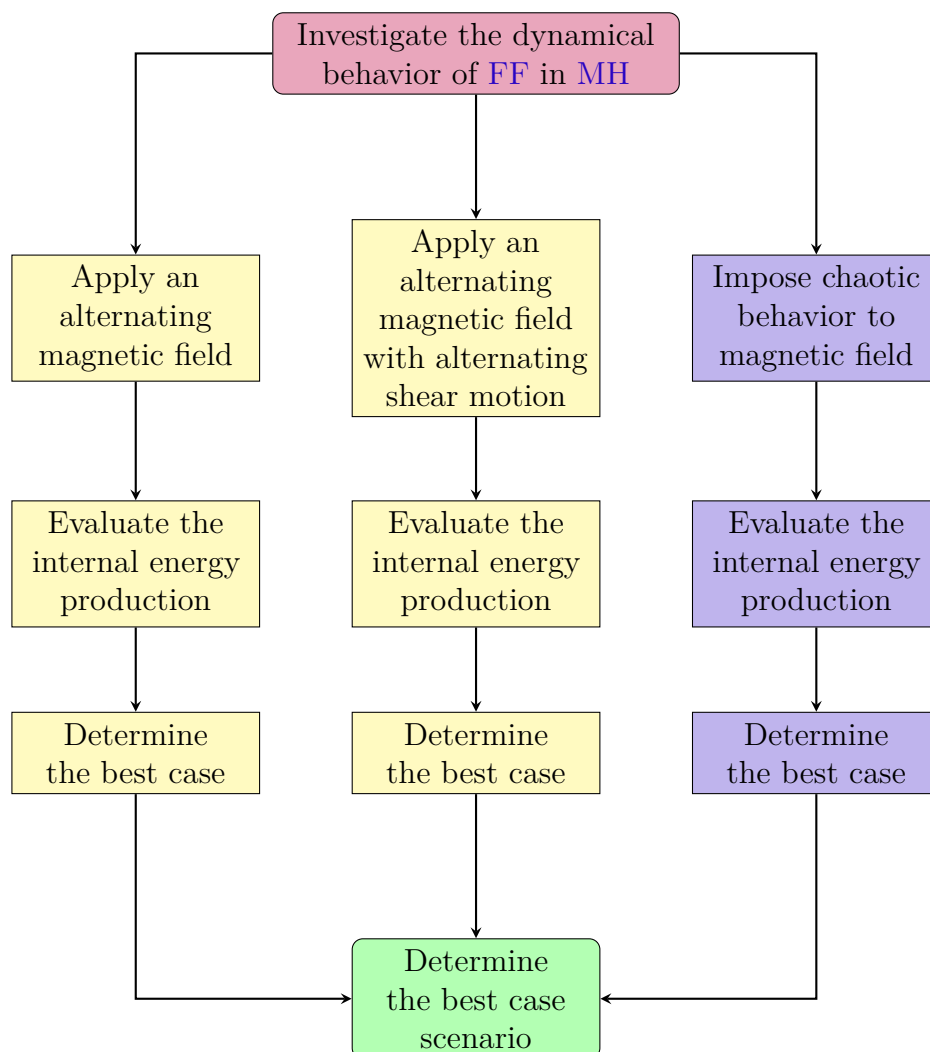
Figure 1.2 – Flowchart representing the methodology of this work.

1.4 Contribution

Although some authors in the literature carry out a dynamical analysis of FFs, none of them considers a FF under MH. This work contributes to filling this gap, evaluating a dynamical analysis of FF used in MH. To simulate a FF, it is considered a dynamical system made with MNPs and governed by nonlinear differential equations. The internal energy per unit volume produced by the MNPs is quantified for different parameters and types of excitation, with the main purpose of defining the best scenario for MH, i.e., the case in which the internal energy production is the highest.

1.4.1 Scope of the Work

Figure 1.3 displays a flowchart of the structure of this dissertation. Chapter 2: Ferrohydrodynamics and Description of the System presents the derivation of the equations of motion that govern the MNPs' system, as well as the numerical methodology applied in order to achieve faster convergence. Chapter 3: Nonlinear Dynamics and Signal Processing describes the dynamical tools and nonlinear concepts used in this work, such as bifurcation diagram, Poincaré map, and Fourier Transform. Gathering Chapters 2 and 3, Chapter 4: Results of Alternating Magnetic Field displays the results for a system with only an alternating magnetic field as excitation. Chapter 5: Results of Alternating Magnetic Field with Shear Motion shows the results with both magnetic field and an alternating shear flow as excitation. Chapter 6: Results of Chaotic Magnetic Field displays the results for a imposed chaotic magnetic field. Chapter 7: Conclusion and Future Work shows the conclusion of the work and insights for future work.
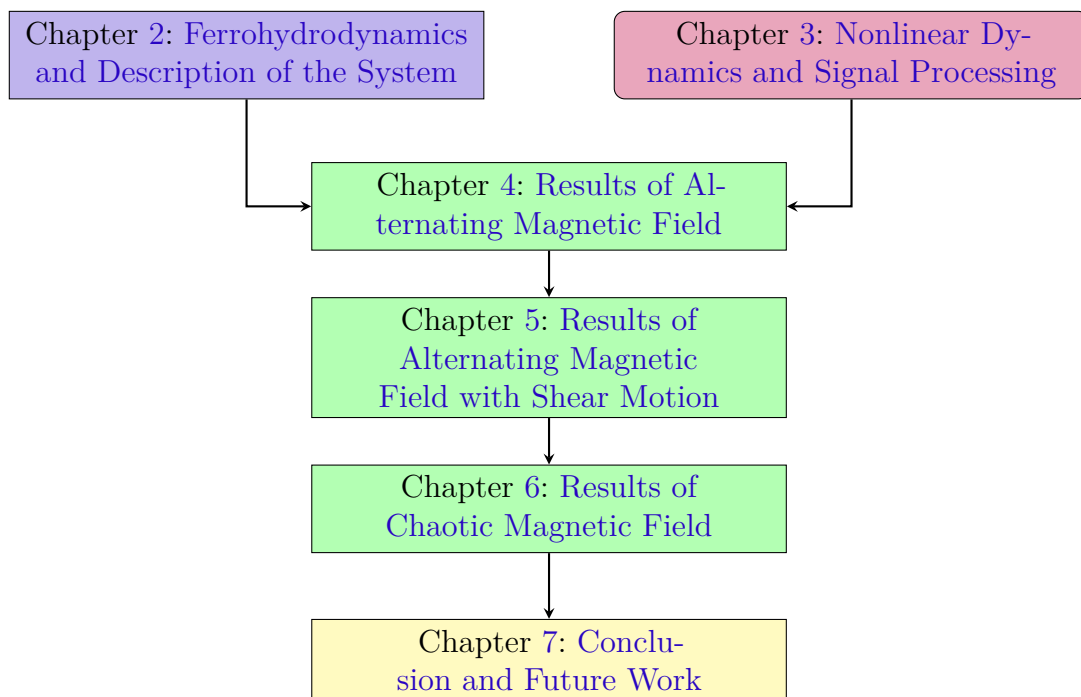
Figure 1.3 – Schematic representation of the chapters in this dissertation.

2 Ferrohydrodynamics and Description of the System

"When you yourself are responsible for some new application in mathematics in your chosen field, then your reputation, possibly millions of dollars and long delays in the work, and possibly even human lives, may depend on the results you predict. It is then the need for mathematical rigor will become painfully obvious to you."

Richard Hamming

2.1 Spatial description

The system consists of MNPs dispersed in a newtonian fluid under low Reynolds number, analyzed by the lagrangean description (Gontijo; Cunha, 2015). Each particle is a rigid body with mass and volume, subjected to translation and rotation. Hence, a many-body problem is carried out.

A sample of 300 MNPs is simulated in a volume represented by a cubic box, shown in Fig. 2.1. The boundary of the box is displayed by gray lines, while the MNPs are represented by black spheres with red magnetic moments. A monodisperse suspension is considered, that is, all the MNPs have the same volume (same radius).

The magnetic response of the system depends on the average of all magnetic dipole moments. The MNPs initially have an homogeneous random distribution, such that the magnetic response of the system is equal to zero - Fig. 2.1 (a). When an external magnetic field is applied, the MNPs align in the direction of the magnetic field and the system presents a magnetic response - Fig. 2.1 (b). A complete three-dimensional view of the system is shown in Fig. 2.1 (c).
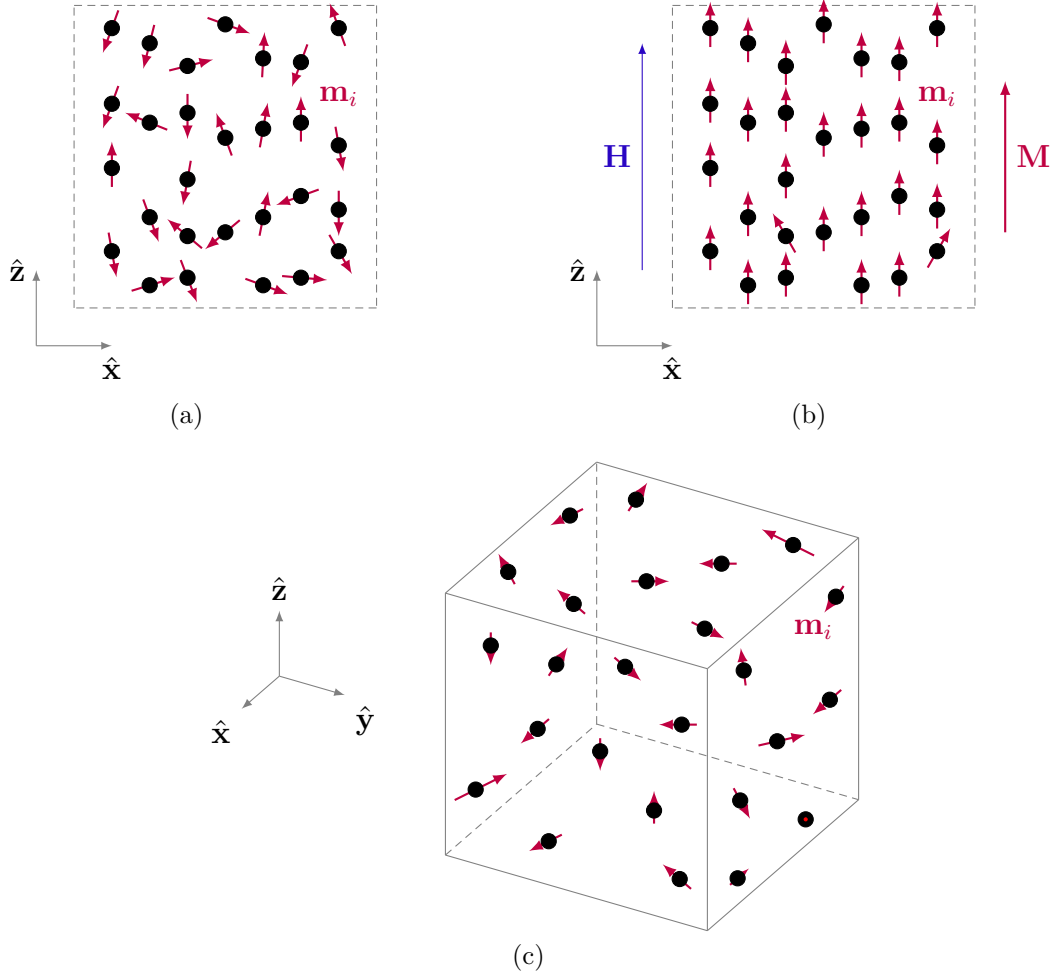
Figure 2.1 – Representation of MNPs dispersed in a liquid carrier. Each particle contains a magnetic moment dipole vector ($\mathbf{m}_i$) with its own orientation, illustrated in red. (a) MNPs initially randomly distributed. (b) MNPs after the application of an external magnetic field ($\mathbf{H}$) represented in blue, such that the particles show a preferential direction and magnetization vector can be observed ($\mathbf{M}$). (c) Three-dimensional view of the MNPs' domain.

Each MNP has a permanent magnetic dipole moment, $\mathbf{m}_i$, where $i \in \mathbb{N} \mid 1 \leq i \leq N$ is a natural number that represents the index of each particle and $N = 300$ is the total number of particles. Thus,

$$\mathbf{m}_i = m\hat{\mathbf{d}}_i, \quad i = 1, \ldots, N, \tag{2.1}$$

where m is a scalar quantity named dipole intensity and $\hat{\mathbf{d}}_i$ is an unit vector representing the i-th particle dipole orientation and N is the total number of MNPs.

For any given configuration of particles, the system's magnetic response can be calculated by Eq. (2.2),

$$\mathbf{M} = \frac{1}{V} \sum_{i=1}^{N} \mathbf{m}_i = \frac{N}{V} \left(\frac{1}{N} \sum_{i=1}^{N} \mathbf{m}_i \right) = n\overline{\mathbf{m}}, \tag{2.2}$$

where $\mathbf{M}$ is the magnetization vector, V is the total volume of the system, $n = N/V$ is the density number and $\overline{\mathbf{m}}$ is the mean value of all magnetic dipole vectors. To represent a cartesian coordinate system, $\hat{\mathbf{x}}$, $\hat{\mathbf{y}}$ and $\hat{\mathbf{z}}$ are, respectively, the unit vectors in the x, y, and z directions, such that $\mathbf{M} = M_x\hat{\mathbf{x}} + M_y\hat{\mathbf{y}} + M_z\hat{\mathbf{z}}$.

For example, in Fig. 2.1a, there is no magnetic field applied, consequently, the sum of all magnetic dipole moments results in a magnetization equal to zero ($\|\mathbf{M}\| = 0$) and the system behaves like a newtonian fluid (Gontijo; Cunha, 2015). On the other hand, in Fig. 2.1b, if one applies a magnetic field, $\mathbf{H}$, most magnetic dipole moments orient themselves at the same direction of the field. As a result, the magnetization in the system is greater than zero ($\|\mathbf{M}\| > 0$) and the fluid behaves like a non-newtonian fluid (Rosensweig, 2013).

When all magnetic moments are in the same direction, due to a high magnitude magnetic field, $\mathbf{H}$, the system reaches the saturation magnetization, M_s, that is, the maximum magnetization possible from the FF, given by Eq. (2.3),

$$M_s = \phi M_d, \tag{2.3}$$

where ϕ is the magnetic volume fraction and M_d is the spontaneous magnetization of the magnetic material, i.e., the solid from which the particles are made (Odenbach, 2009). For instance, the spontaneous magnetization of magnetite is $M_d = 4,5 \cdot 10^5 \mathrm{A/m}$.

2.1.1 Volume Estimation

The volume fraction of MNPs is calculated by Eq. (2.4),

$$\phi = \frac{V_p}{V} = \frac{1}{V} \sum_{i=1}^{N} v_i, \tag{2.4}$$

where V_p is the volume occupied by all MNPs and v_i is the volume of the i-th MNP.

Considering that all MNPs are perfect spheres with same radius, a,

$$V_p = \sum_{i=1}^{N} \frac{4\pi}{3} a^3 = \frac{4\pi}{3} N a^3. \tag{2.5}$$

The substitution of Eq. (2.5) into Eq. (2.4) yields

$$\phi = \frac{4\pi a^3}{3} \frac{N}{V}. \tag{2.6}$$

Hence, the volume of the box is given by

$$V = \frac{4\pi a^3}{3} \frac{N}{\phi}. \tag{2.7}$$

Applying the values $N = 300$, $\phi = 1\%$ and $a = 12.5$ nm gives $V \approx 2.45 \cdot 10^{-19}$ m^3 as estimation of the FF's volume. Thus, a very small sample is simulated in this work.

2.1.2 Boundary Conditions

Periodic boundary conditions are applied in each boundary of the box, such that, when a particle reaches a boundary, it is translated to opposing side. The goal of this boundary condition is to simulate an infinite suspension, that is, a continuous media of the FF, without the influence of boundaries, given that particles near walls have their motion greatly affected (Gontijo; Cunha, 2015). Figure 2.2 shows the moment when a particle crosses the boundary.
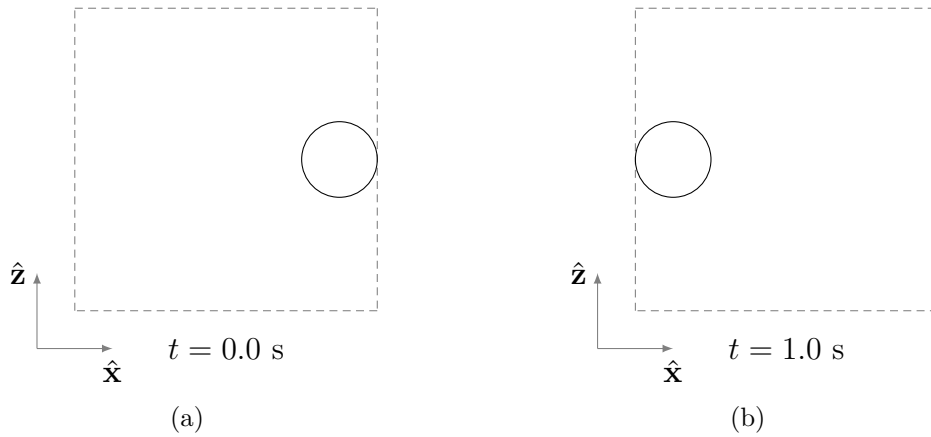
Figure 2.2 – Representation of a periodic boundary condition, as a MNP crosses the border. (a) Before the MNP reaches the rightmost boundary. (b) After the MNP reaches the rightmost boundary.

2.2 Time description

2.2.1 Initial Condition

A uniform distribution of MNPs is applied as initial condition, with random and independent positions and dipole moments.

Whenever particle overlap occurs during the generation of the initial condition, a random displacement based on brownian motion is applied to separate the particles, so that the particle distribution in space is statistically homogeneous (Gontijo; Cunha, 2015).

Fig. 2.3 shows a case of particle agglomeration in the initial condition and the procedure to separate them.

(a)   (b)
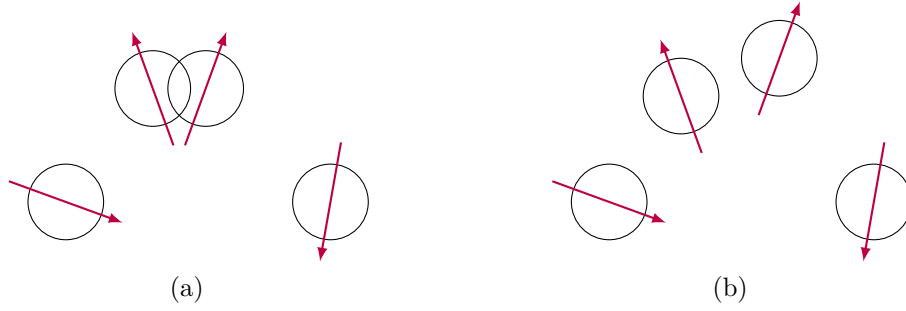
Figure 2.3 – Representation of the superposition of two particles in the generation of the initial condition. a) Overlapped particles. b) Particles separated after brownian motion.

2.2.2   Equations of Motion

The motion of each MNP is governed by the Newton's second law (Newton-Euler equations), given by Eq. (2.8) and Eq. (2.9) (Gontijo; Cunha, 2015). Regarding the translational motion, there is Eq. (2.8),

$$\mathcal{M}\frac{\mathrm{d}\mathbf{u}_i}{\mathrm{d}t} = -6\pi\eta a\mathbf{u}_i + \frac{4}{3}\pi a^3\Delta\rho\mathbf{g} + \mathbf{F}_{\mathbf{B}i} + \mathbf{F}_{\mathbf{m}i} + \mathbf{F}_{\mathbf{r}i} + \mathbf{F}_{\mathbf{c}i}, \tag{2.8}$$

in which $\mathbf{u}_i$ is the linear velocity of the i-th MNP, $\mathcal{M}$ is its mass (all MNPs have the same volume and mass), t is the time, $\Delta\rho = \rho_s - \rho_f$ is the difference between the density of the particles, ρ_s, and the density of the fluid carrier, ρ_f, η is the dynamic viscosity of the fluid carrier, $\mathbf{g}$ is the gravitational vector field, such that $\mathbf{g} = -g\hat{\mathbf{z}}$, where $g = 9.8$ m/s^2 is the magnitude of gravity, $\mathbf{F}_{\mathbf{B}i}$ is the brownian force imposed in the i-th particle, $\mathbf{F}_{\mathbf{m}i}$ is the magnetic force applied upon the i-th particle, $\mathbf{F}_{\mathbf{r}i}$ is the repulsive force in the i-th particle and $\mathbf{F}_{\mathbf{c}i}$ is the contact force applied in the i-th particle.

Concerning rotational motion, Eq. (2.9) shows the governing equation,

$$\mathcal{I}\frac{\mathrm{d}\boldsymbol{\omega}_i}{\mathrm{d}t} = -8\pi\eta a^3\boldsymbol{\omega}_i + \mathbf{T}_{\mathbf{B}i} + \mathbf{T}_{\mathbf{m}i}, \tag{2.9}$$

where $\mathcal{I}$ is the i-th particle's moment of inertia, $\boldsymbol{\omega}_i$ is its angular velocity, $\mathbf{T}_{\mathbf{B}i}$ is the brownian torque imposed in the i-th particle and $\mathbf{T}_{\mathbf{m}i}$ is the magnetic torque upon the i-th particle.

Thus, the kinematics of each magnetic moment is given by Eq. (2.10)

$$\frac{\mathrm{d}}{\mathrm{d}t}\hat{\mathbf{d}}_i = \boldsymbol{\omega}_i \times \hat{\mathbf{d}}_i, \tag{2.10}$$

where $\times$ is the cross product between two vectors.

Each force and torque from Eqs. (2.8) and (2.9) is described in the next sections.

2.2.2.1   Magnetic Force and Torque

To calculate the magnetic forces, one must consider the interactions between particles and the interaction of each particle with an external magnetic field. For the first one, the potential under the i-th particle due to dipole-dipole interaction, ψ_{p_i}, is given by Eq. (2.11),

$$\psi_{p_i} = m_i \sum_{\substack{j=1 \\ j \neq i}}^{N} \frac{\mu_0 m_j}{4\pi r_{ij}} \left[\hat{\mathbf{d}}_i \cdot \hat{\mathbf{d}}_j - 3 \left(\hat{\mathbf{d}}_i \cdot \hat{\mathbf{r}}_{ij} \right) \left(\hat{\mathbf{d}}_j \cdot \hat{\mathbf{r}}_{ij} \right) \right], \tag{2.11}$$

where the index j represents all the other particles that influence the motion of the i-th particle, $\mu_0 = 1.26 \cdot 10^{-6}$ H m^{-1} is the vacuum permeability, m_i is the magnetic dipole intensity of the i-th particle and r_{ij} is the distance between the center os mass of the i-th particle and the j-th particle. Lastly, the vector $\mathbf{r}_{ij}$ represents the distance between the centers of mass of both particles, such that the vector begins at the j-th particle and end at the i-th particle. In this manner, Eqs. (2.12) and (2.13) show the relation of such vector,

$$\mathbf{r}_{ij} = \mathbf{r}_i - \mathbf{r}_j, \tag{2.12}$$

$$\mathbf{r}_{ij} = r_{ij} \hat{\mathbf{r}}_{ij}, \tag{2.13}$$

in which $\mathbf{r}_i$ and $\mathbf{r}_j$ are, respectively, the position vector of the i-th and the j-th particle with respect to the origin, $\hat{\mathbf{r}}_{ij}$ is the unitary vector in the direction between those two particles and $r_{ij} = \|\mathbf{r}_{ij}\|$.

Fig. 2.4 exemplifies the process of calculating the potential of the i-th particle (on left) upon the presence of another particle (on right). Note that the distance vector $\mathbf{r}_{ij}$ begins at the j-th particle and ends at the i-th particle.
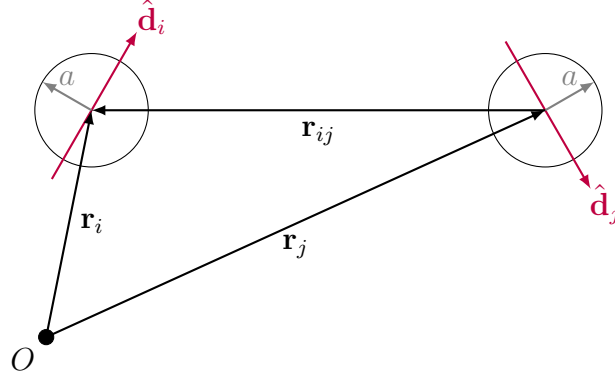
Figure 2.4 – Representation of the dipole-dipole potential for the i-th particle (on left), where the j-th particle (on right) influences the motion of the former. O is the origin, a is the hydrodynamic radius, $\hat{\mathbf{d}}_i$ is the dipole direction for the i-th particle, $\mathbf{r}_i$ and $\mathbf{r}_j$ are, respectively, the position vectors for the i-th and j-th particle, $\mathbf{r}_{ij}$ is the vector of the distance between the centers of mass of both particles.

For the second interaction, the potential upon the i-th particle due to an external magnetic field, ψ_{f_i}, is given by Eq. (2.14)

$$\psi_{f_i} = -\mu_0 m_i H \left(\hat{\mathbf{d}}_i \cdot \hat{\mathbf{H}} \right), \tag{2.14}$$

where $\mathbf{H}$ is the external magnetic field vector, such that $\mathbf{H} = H\hat{\mathbf{H}}$, in which H is its intensity and $\hat{\mathbf{H}}$ is its direction.

From Eqs. (2.11) and (2.14), the magnetic force for the i-th particle, $\mathbf{F}_{\mathbf{m}i}$, is given by Eq. (2.15),

$$\mathbf{F}_{\mathbf{m}i} = - \left(\nabla \psi_{f_i} + \nabla \psi_{p_i} \right), \tag{2.15}$$

where $\nabla = \dfrac{\partial}{\partial x}\,\hat{\mathbf{x}} + \dfrac{\partial}{\partial y}\,\hat{\mathbf{y}} + \dfrac{\partial}{\partial z}\,\hat{\mathbf{z}}$ is the gradient operator.

Similarly, the magnetic torque upon the i-th particle, $\mathbf{T}_{\mathbf{m}i}$, is stated by Eq. (2.16),

$$\mathbf{T}_{\mathbf{m}i} = -\hat{\mathbf{d}}_i \times \left(\nabla_{\hat{\mathbf{d}}_i} \psi_{f_i} + \nabla_{\hat{\mathbf{d}}_i} \psi_{p_i} \right), \tag{2.16}$$

in which $\nabla_{\hat{\mathbf{d}}_i} = \dfrac{\partial}{\partial \hat{d}_{i_x}}\,\hat{\mathbf{x}} + \dfrac{\partial}{\partial \hat{d}_{i_y}}\,\hat{\mathbf{y}} + \dfrac{\partial}{\partial \hat{d}_{i_z}}\,\hat{\mathbf{z}}$ represents the gradient so that the derivatives are taken with respect to the dipole orientation (Gontijo; Cunha, 2015).

The development of Eqs. (2.15) and (2.16) yields Eqs. (2.17) and (2.18)

$$\mathbf{F_{m}}_i = \left\{ \frac{3\mu_0 m_i}{4\pi} \sum_{\substack{j=1 \\ j \neq i}}^{N} \frac{m_j}{r_{ij}^4} \left[\left(\hat{\mathbf{d}}_i \cdot \hat{\mathbf{d}}_j \right) \hat{\mathbf{r}}_{ij} + \left(\hat{\mathbf{d}}_i \cdot \hat{\mathbf{r}}_{ij} \right) \hat{\mathbf{d}}_j + \left(\hat{\mathbf{d}}_j \cdot \hat{\mathbf{r}}_{ij} \right) \hat{\mathbf{d}}_i + \right. \right.$$

$$\left. \left. - 5 \left(\hat{\mathbf{d}}_i \cdot \hat{\mathbf{r}}_{ij} \right) \left(\hat{\mathbf{d}}_j \cdot \hat{\mathbf{r}}_{ij} \right) \hat{\mathbf{r}}_{ij} \right] \right\} + \mu_0 m_i H \left(\hat{\mathbf{d}}_i \cdot \nabla \hat{\mathbf{H}} \right), \quad (2.17)$$

$$\mathbf{T_{m}}_i = \left\{ \frac{3\mu_0 m_i}{4\pi} \sum_{\substack{j=1 \\ j \neq i}}^{N} \frac{m_j}{r_{ij}^3} \left[- \frac{1}{3} \left(\hat{\mathbf{d}}_i \times \hat{\mathbf{d}}_j \right) + \left(\hat{\mathbf{d}}_j \cdot \hat{\mathbf{r}}_{ij} \right) \left(\hat{\mathbf{d}}_i \times \hat{\mathbf{r}}_{ij} \right) \right] \right\} + \mu_0 m_i H \hat{\mathbf{d}}_i \times \hat{\mathbf{H}}. \quad (2.18)$$

Under the hypothesis that all magnetic particles have the same magnetic moment intensity, such that $m_i = m_j = m$, and that the external magnetic field does not depend on the position, such that $\nabla \mathbf{H} = \mathbf{0}$, Eqs. (2.17) and (2.18) are simplified to Eqs. (2.19) and (2.20),

$$\mathbf{F_{m}}_i = \left\{ \frac{3\mu_0 m^2}{4\pi} \sum_{\substack{j=1 \\ j \neq i}}^{N} \frac{1}{r_{ij}^4} \left[\left(\hat{\mathbf{d}}_i \cdot \hat{\mathbf{d}}_j \right) \hat{\mathbf{r}}_{ij} + \left(\hat{\mathbf{d}}_i \cdot \hat{\mathbf{r}}_{ij} \right) \hat{\mathbf{d}}_j + \left(\hat{\mathbf{d}}_j \cdot \hat{\mathbf{r}}_{ij} \right) \hat{\mathbf{d}}_i + \right. \right.$$

$$\left. \left. - 5 \left(\hat{\mathbf{d}}_i \cdot \hat{\mathbf{r}}_{ij} \right) \left(\hat{\mathbf{d}}_j \cdot \hat{\mathbf{r}}_{ij} \right) \hat{\mathbf{r}}_{ij} \right] \right\}, \quad (2.19)$$

$$\mathbf{T_{m}}_i = \left\{ \frac{3\mu_0 m^2}{4\pi} \sum_{\substack{j=1 \\ j \neq i}}^{N} \frac{1}{r_{ij}^3} \left[- \frac{1}{3} \left(\hat{\mathbf{d}}_i \times \hat{\mathbf{d}}_j \right) + \left(\hat{\mathbf{d}}_j \cdot \hat{\mathbf{r}}_{ij} \right) \left(\hat{\mathbf{d}}_i \times \hat{\mathbf{r}}_{ij} \right) \right] \right\} + \mu_0 m H \hat{\mathbf{d}}_i \times \hat{\mathbf{H}}. \quad (2.20)$$

Due to the dependence on $1/r_{ij}^4$ and $1/r_{ij}^3$, the magnetic force and torque are nonlinear terms of the differential governing equations, Eq. (2.8) and Eq. (2.9).

2.2.2.2 Brownian Force and Torque

The brownian force is calculated by the stochastic Langevin's equation, considering its behavior as a stationary white noise (Poland, 1977), (Gontijo; Cunha, 2015). For an isolated particle (Guimarães; Cunha; Gontijo, 2020), the stochastic brownian force is given by Eq. (2.21),

$$\mathbf{F_{B}}_i = 6\pi \eta a \left(6 \frac{\mathcal{D}_t}{\delta \tau} \right)^{1/2} \boldsymbol{\xi}, \quad (2.21)$$

where $\mathcal{D}_t = \dfrac{K_b T}{6\pi \eta a}$ is the translational brownian diffusion coefficient of Stokes-Einstein (Einstein, 1956), K_b is the Boltzmann's constant, T is the temperature in Kelvin, $\delta \tau$ is

the time step related to brownian thermal fluctuations (Guimarães; Cunha; Gontijo, 2020) and $\boldsymbol{\xi}$ is a random unitary vector, defined by Eq. (2.22),

$$\boldsymbol{\xi} = \frac{1}{\|\boldsymbol{\xi}\|} \left(\xi_x \hat{\mathbf{x}} + \xi_y \hat{\mathbf{y}} + \xi_z \hat{\mathbf{z}} \right), \tag{2.22}$$

where ξ_x, ξ_y and ξ_z are 3 distinct random numbers with uniform distribution between $[1, -1]$ and $\|\boldsymbol{\xi}\| = \sqrt{\xi_x^2 + \xi_y^2 + \xi_z^2}$.

In a similar way to Eq. (2.21), stochastic brownian torque is given by Eq. (2.23), (Gontijo; Cunha, 2015)

$$\mathbf{T}_{\mathbf{B}i} = 8\pi\eta a^3 \left(6 \frac{\mathcal{D}_r}{\delta\tau} \right)^{1/2} \boldsymbol{\xi}, \tag{2.23}$$

where $\mathcal{D}_r = \dfrac{K_b T}{8\pi\eta a^3}$ is the rotational brownian diffusion coefficient of Stokes-Einstein (Einstein, 1956).

The terms $6\pi\eta a \left(6 \frac{\mathcal{D}_t}{\delta\tau} \right)^{1/2}$ and $8\pi\eta a^3 \left(6 \frac{\mathcal{D}_r}{\delta\tau} \right)^{1/2}$ represent the modeling of the stochastic force and torque, respectively, while the term $\boldsymbol{\xi}$ represents the algorithm variable implemented to simulate the force and torque. The brownian force and torque are stochastic terms of the differential governing equations, Eq. (2.8) and Eq. (2.9).

2.2.2.3 Repulsive and Contact Forces

During the computational simulation, overlapping of particles must be avoided. Because there are no lubrication forces, a numerical fictitious force is added to the system (Cunha et al., 2002). This force is described by Eqs. (2.24) and (2.25),

$$\mathbf{F}_{\mathbf{r}i} = C_1 \left(6\pi\eta a \right) u_i \exp\left(-\frac{\epsilon_{ij}}{C_2} \right) \hat{\mathbf{r}}_{ij}. \tag{2.24}$$

$$\epsilon_{ij} = |r_{ij} - 2a| \tag{2.25}$$

in which C_1 and C_2 are calibrations constants associated with intensity and range of the near field interaction, exp is the exponential function with Euler's number as the base number, $\hat{\mathbf{r}}_{ij}$ is the unitary vector in the particle's radial direction, ϵ_{ij} is the distance between the surfaces of the near particles, $u_i = \|\mathbf{u}_i\|$ is the magnitude of the i-th particle's velocity and $r_{ij} = \|\mathbf{r}_{ij}\|$ (Gontijo; Cunha, 2015). Figure 2.5 shows a schematic drawing of 2 near particles and the repulsive force applied in both to avoid superposition.

Due to the dependence on $u_i \exp\left(-\frac{\epsilon_{ij}}{C_2} \right)$, the repulsive force is a nonlinear term of the governing equations of motion, Eq. (2.8) and Eq. (2.9).
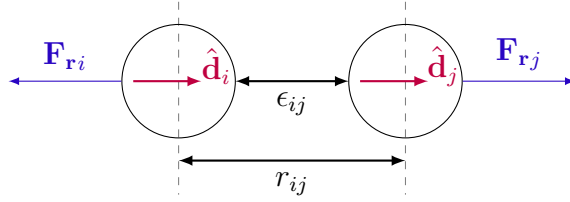
Figure 2.5 – Representation of the repulsive forces ($\mathbf{F_{r}}_i$ and $\mathbf{F_{r}}_j$) added to two particles under attraction movement, due to the position of the magnetic dipoles ($\hat{\mathbf{d}}_i$ and $\hat{\mathbf{d}}_j$). Figure adapted from Gontijo and Cunha (2015)

As the particle's inertia is not negligible in the simulations, a contact force must also be considered in the system, representing the particles' collision with each other (Gontijo; Cunha, 2015). This condition of Hertz contact force is shown at Eqs. (2.26) and (2.27),

$$\mathbf{F_{c}}_i = C_3 \varepsilon b^{1/2} \epsilon_{ij}^{3/2} \; \hat{\mathbf{r}}_{ij}. \tag{2.26}$$

$$\varepsilon = \frac{E}{2\left(1 - \nu\right)} \tag{2.27}$$

where C_3 is a calibration constant, ε is a material constant, E is the particles' Young modulus, ν is the particles' Poisson's ratio and b is a parameter equal to $a/2$ for the case of monodisperse suspensions. During the collision, $r_{ij} < 2a$, such that $\epsilon_{ij} = 2a - r_{ij}$. Figure 2.6 displays a schematic drawing of the collision of two particles and the position of each contact reppeling force at the radial direction.
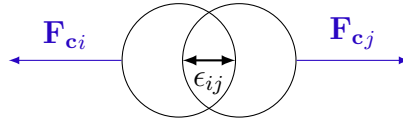
Figure 2.6 – Representation of two particles collision and their contact forces ($\mathbf{F_{c}}_i$ and $\mathbf{F_{c}}_j$). Figure adapted from Gontijo and Cunha (2015)

Due to the dependence on $\epsilon_{ij}^{3/2}$, the contact force is a nonlinear term of the governing equations of motion, Eq. (2.8) and Eq. (2.9).

2.3   Shear Rate

Shear rate is a condition both spatial and time dependent. In this study, MNPs are subjected to oscillatory simple shear, so that translation of particles depends on the height. When shear motion is activated in the simulations, a shear flow is added in the $\hat{\mathbf{y}}$ direction, such that the velocity of each particle is given by a new variable, $\mathbf{u_{sh}}_i$,

$$\mathbf{u_{sh}}_i = \mathbf{u}_i + \left(0, \dot{\gamma}z, 0\right), \tag{2.28}$$

in which $\mathbf{u}_{\mathbf{sh}i}$ is the velocity of the system under shear flow, $\dot{\gamma}$ is the shear rate, z is the height of the particle (position at the $\hat{\mathbf{z}}$ direction). In a similar way, for the rotational motion, shear rate yields

$$\boldsymbol{\omega}_{\mathbf{sh}i} = \boldsymbol{\omega}_i + \left(\frac{\dot{\gamma}}{2}, 0, 0\right), \tag{2.29}$$

where $\boldsymbol{\omega}_{\mathbf{sh}i}$ is the angular velocity of the i-th particle when the system is under shear flow.

Hence, the kinematics of each dipole orientation, $\hat{\mathbf{d}}_i$, is

$$\frac{\mathrm{d}}{\mathrm{d}t}\hat{\mathbf{d}}_i = \boldsymbol{\omega}_{\mathbf{sh}i} \times \hat{\mathbf{d}}_i \tag{2.30}$$

To exemplify the shear motion, Fig. 2.7 shows a system under simple shear motion, without the magnetic mechanisms and for a constant shear rate $\dot{\gamma}$. The MNPs start aligned in the $\hat{\mathbf{z}}$ direction at $t = 0$. For $t > 0$, the shear motion begins. The particles at the bottom do not translate, but only rotate, while the ones at the top experience both translation and rotation.
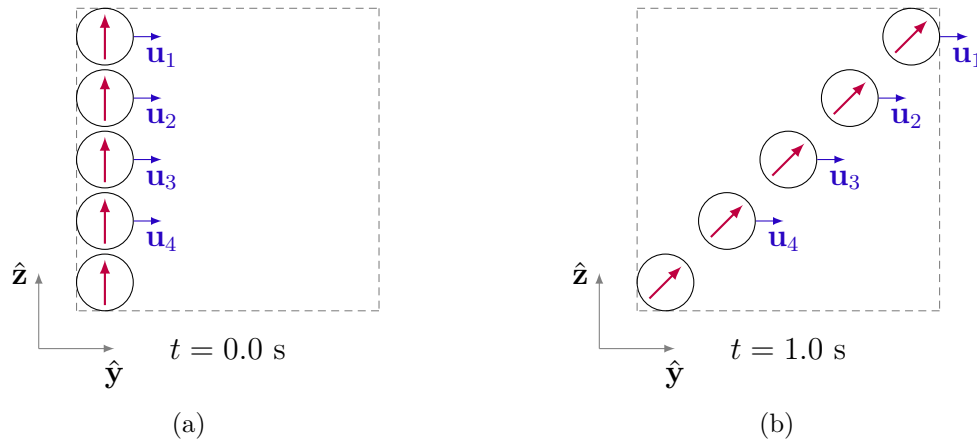
Figure 2.7 – Representation of the simple shear motion. Velocities of each particle in blue and magnetic moments in red. (a) Particles aligned in the initial condition, at $t = 0$ s. (b) Particles after the start of the shear motion, at $t = 1$ s.

If an oscillatory simple shear is imposed, the motion reverses direction indefinitely. Fig. 2.8 shows an example of MNPs subjected to oscillatory simple shear, that is, for a shear rate dependent of time, $\dot{\gamma}(t) = \dot{\gamma}_0 \sin(\omega_S t)$, in which $\dot{\gamma}_0$ and ω_S are, respectively, the shear rate's amplitude and frequency.
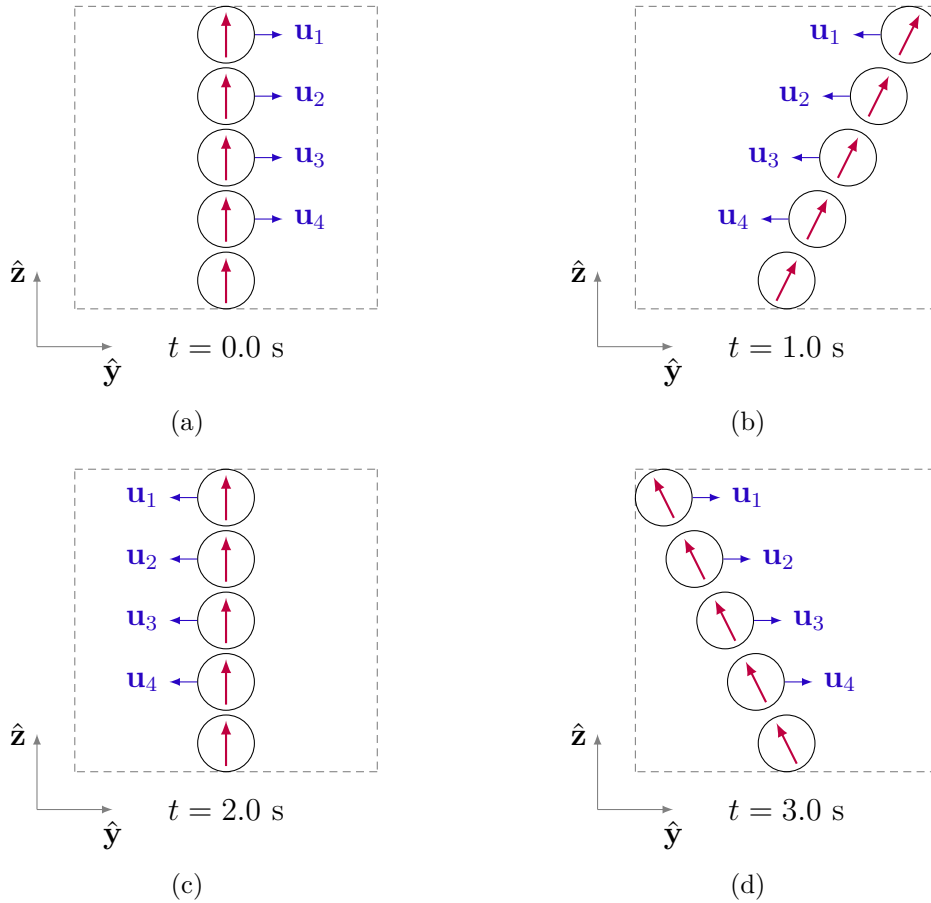
Figure 2.8 – Representation of the oscillatory simple shear mechanism. Velocities of each particle in blue and magnetic moments in red. (a) Particles aligned in the initial condition ($t = 0$ s). (b) Particles after the start of the shear motion, moving to the right ($t = 1$ s). (c) Particles when the shear motion changes direction, moving from the right to the left ($t = 2$ s). (d) Particles after the reversal shear motion, moving to the left ($t = 3$ s).

2.4 Average Magnetization

The system is random, due to the probabilistic nature of brownian motion, which represents the collision of the MNPs with the newtonian fluid. Because of this, each magnetization can be different from another for the same number of particles. To decrease the random effect in the magnetization, several realizations of the system are performed for each moment of time and a mean value of all theses samples is obtained, as specified by Eq. (2.31),

$$\overline{\mathbf{M}}(t) = \frac{1}{K} \sum_{k=1}^{K} \mathbf{M}_k(t) \tag{2.31}$$

where $k \in \mathbb{N} \mid 1 \leq k \leq K$ is a natural number representing the index of each realization, K is the total number of realizations ($K = 50$ for all simulations), $\mathbf{M}_k$ is the magnetization

for the k-th realization and $\overline{\mathbf{M}}$ is the average magnetization for all realizations.

2.5 Average Rate of Internal Energy Dissipation

From the first law of thermodynamics,

$$\mathrm{d}U = \delta Q + \delta W, \tag{2.32}$$

where $\mathrm{d}U$ is the internal energy per unit volume, δQ is the heat per unit volume and δW is the magnetic work per unit volume under the system.

Under the hypothesis of an adiabatic process, such that $\delta Q = 0$,

$$\mathrm{d}U = \delta W. \tag{2.33}$$

For the magnetic work per unit volume, one can use $\delta W = \mathbf{H} \cdot \mathrm{d}\mathbf{B}$, in which $\mathbf{B}$ is the induction vector field (Stratton, 2007),

$$\mathrm{d}U = \mathbf{H} \cdot \mathrm{d}\mathbf{B}. \tag{2.34}$$

From the definition of the induction vector field,

$$\mathbf{B} = \mu_0 \left(\mathbf{M} + \mathbf{H} \right). \tag{2.35}$$

The substitution of Eq. (2.35) into (2.34) yields

$$\mathrm{d}U = \mu_0 \mathbf{H} \cdot \mathrm{d}\mathbf{M} + \mu_0 \mathbf{H} \cdot \mathrm{d}\mathbf{H}. \tag{2.36}$$

One can note that, by the product rule of derivatives,

$$\mathrm{d}\left(\frac{\|\mathbf{H}\|^2}{2} \right) = \mathrm{d}\left(\frac{\mathbf{H} \cdot \mathbf{H}}{2} \right) = \frac{1}{2} \left(\mathbf{H} \cdot \mathrm{d}\mathbf{H} \right) + \frac{1}{2} \left(\mathbf{H} \cdot \mathrm{d}\mathbf{H} \right) = \mathbf{H} \cdot \mathrm{d}\mathbf{H} \tag{2.37}$$

Applying Eq.(2.37) into (2.36) yields

$$\mathrm{d}U = \mu_0 \mathbf{H} \cdot \mathrm{d}\mathbf{M} + \mu_0 \, \mathrm{d}\left(\frac{\|\mathbf{H}\|^2}{2} \right). \tag{2.38}$$

Considering that $\mathbf{H} = \mathbf{H}(t)$ and $\mathbf{M} = \mathbf{M}(t)$ are both functions of time, by the chain rule, one can obtain

$$\frac{\mathrm{d}U}{\mathrm{d}t}\,\mathrm{d}t = \mu_0 \mathbf{H} \cdot \frac{\mathrm{d}\mathbf{M}}{\mathrm{d}t}\,\mathrm{d}t + \mu_0 \frac{\mathrm{d}}{\mathrm{d}t}\left(\frac{\|\mathbf{H}\|^2}{2}\right)\mathrm{d}t. \tag{2.39}$$

Then, Eq. (2.39) is integrated from the time $t = 0$ to $t = t_f$, where t_f is the final time of the simulation

$$\int_0^{t_f} \frac{\mathrm{d}U}{\mathrm{d}t}\,\mathrm{d}t = \mu_0 \int_0^{t_f} \mathbf{H} \cdot \frac{\mathrm{d}\mathbf{M}}{\mathrm{d}t}\,\mathrm{d}t + \mu_0 \int_0^{t_f} \frac{\mathrm{d}}{\mathrm{d}t}\left(\frac{\|\mathbf{H}\|^2}{2}\right)\mathrm{d}t \tag{2.40}$$

$$\Longrightarrow U(t_f) - U(0) = \mu_0 \int_0^{t_f} \mathbf{H} \cdot \frac{\mathrm{d}\mathbf{M}}{\mathrm{d}t}\,\mathrm{d}t + \frac{\mu_0}{2}\left[\|\mathbf{H}\|(t_f)^2 - \|\mathbf{H}\|(0)^2\right] \tag{2.41}$$

$$\Longrightarrow \Delta U = \mu_0 \int_{\mathbf{M}(0),\mathbf{H}(0)}^{\mathbf{M}(t_f),\mathbf{H}(t_f)} \mathbf{H} \cdot \mathrm{d}\mathbf{M} + \frac{\mu_0}{2}\left[\|\mathbf{H}\|(t_f)^2 - \|\mathbf{H}\|(0)^2\right] \tag{2.42}$$

where $\Delta U := U(t_f) - U(0)$ is the total variation of the magnetic contribution of internal energy per unit volume of the system.

Normally, studies of MH assume that the external magnetic field is a periodic function with period $\mathcal{T}$ (Rosensweig, 2002). Hence, if the final time of the simulation is chosen as one multiple of the period $(t_f = c\mathcal{T})$, the expression of Eq. (2.42) is simplified,

$$\Delta U = \mu_0 \int_{\mathbf{M}(0),\mathbf{H}(0)}^{\mathbf{M}(c\mathcal{T}),\mathbf{H}(c\mathcal{T})} \mathbf{H} \cdot \mathrm{d}\mathbf{M} + \frac{\mu_0}{2}\left[\|\mathbf{H}\|(c\mathcal{T})^2 - \|\mathbf{H}\|(0)^2\right]. \tag{2.43}$$

For a periodic magnetic field, $\mathbf{H}(t) = \mathbf{H}(t + c\mathcal{T})$, where $\mathcal{T}$ is the period of $\mathbf{H}$ and $c \in \mathbb{N}$ is the number of elapsed cycles of $\mathbf{H}$. Thus, $\mathbf{H}(c\mathcal{T}) = \mathbf{H}(0)$, such that

$$\Longrightarrow \Delta U = \mu_0 \int_{\mathbf{M}(0),\mathbf{H}(0)}^{\mathbf{M}(c\mathcal{T}),\mathbf{H}(c\mathcal{T})} \mathbf{H} \cdot \mathrm{d}\mathbf{M} + \frac{\mu_0}{2}\left[\|\mathbf{H}\|(0)^2 - \|\mathbf{H}\|(0)^2\right] \tag{2.44}$$

$$\Longrightarrow \Delta U = \mu_0 \int_{\mathbf{M}(0),\mathbf{H}(0)}^{\mathbf{M}(c\mathcal{T}),\mathbf{H}(c\mathcal{T})} \mathbf{H} \cdot \mathrm{d}\mathbf{M} + 0 \tag{2.45}$$

$$\Longrightarrow \Delta U = \mu_0 \int_{\mathbf{M}(0),\mathbf{H}(0)}^{\mathbf{M}(c\mathcal{T}),\mathbf{H}(c\mathcal{T})} \mathbf{H} \cdot \mathrm{d}\mathbf{M} \tag{2.46}$$

Separating each component of the inner product $\mathbf{H} \cdot \mathrm{d}\mathbf{M}$, considering each contribution as $\mathbf{H} = H_x\hat{\mathbf{x}} + H_y\hat{\mathbf{y}} + H_z\hat{\mathbf{z}}$ and $\mathbf{M} = M_x\hat{\mathbf{x}} + M_y\hat{\mathbf{y}} + M_z\hat{\mathbf{z}}$, yields

$$\Longrightarrow \Delta U = \mu_0\left[\int_{M_x(0),H_x(0)}^{M_x(c\mathcal{T}),H_x(c\mathcal{T})} H_x\,\mathrm{d}M_x + \int_{M_y(0),H_y(0)}^{M_y(c\mathcal{T}),H_y(c\mathcal{T})} H_y\,\mathrm{d}M_y + \right.$$
$$\left. + \int_{M_z(0),H_z(0)}^{M_z(c\mathcal{T}),H_z(c\mathcal{T})} H_z\,\mathrm{d}M_z\right]. \tag{2.47}$$

Equation (2.47) indicates that the internal energy is calculated through the sum of the areas under the curve delimited by $\overline{M}_x$, H_x; $\overline{M}_y$, H_z; and $\overline{M}_z$, H_z (hysteresis curves). Applying integration by parts in Eq. (2.46), one can obtain

$$\Delta U = \mu_0 \Big[\mathbf{H} \cdot \mathbf{M} \Big]_0^{c\mathcal{T}} - \mu_0 \int_{\mathbf{M}(0),\mathbf{H}(0)}^{\mathbf{M}(c\mathcal{T}),\mathbf{H}(c\mathcal{T})} \mathbf{M} \cdot \mathrm{d}\mathbf{H} \tag{2.48}$$

$$= \mu_0 \Big[\mathbf{H}\left(c\mathcal{T}\right) \cdot \mathbf{M}\left(c\mathcal{T}\right) - \mathbf{H}\left(0\right) \cdot \mathbf{M}\left(0\right) \Big] - \mu_0 \int_{\mathbf{M}(0),\mathbf{H}(0)}^{\mathbf{M}(c\mathcal{T}),\mathbf{H}(c\mathcal{T})} \mathbf{M} \cdot \mathrm{d}\mathbf{H} \tag{2.49}$$

$$= \mu_0 \mathbf{H}\left(0\right) \cdot \Big[\mathbf{M}\left(c\mathcal{T}\right) - \mathbf{M}\left(0\right) \Big] - \mu_0 \int_{\mathbf{M}(0),\mathbf{H}(0)}^{\mathbf{M}(c\mathcal{T}),\mathbf{H}(c\mathcal{T})} \mathbf{M} \cdot \mathrm{d}\mathbf{H}. \tag{2.50}$$

Under the hypothesis that the magnetization is a periodic function with the same period as $\mathbf{H}$ (Rosensweig, 2002), such that $\mathbf{M}\left(c\mathcal{T}\right) = \mathbf{M}\left(0\right)$, from Eq. (2.50), one can conclude that

$$\Delta U = -\mu_0 \int_{\mathbf{M}(0),\mathbf{H}(0)}^{\mathbf{M}(c\mathcal{T}),\mathbf{H}(c\mathcal{T})} \mathbf{M} \cdot \mathrm{d}\mathbf{H}. \tag{2.51}$$

Separating each component of the inner product,

$$\Delta U = -\mu_0 \bigg[\int_{M_x(0),H_x(0)}^{M_x(c\mathcal{T}),H_x(c\mathcal{T})} M_x \, \mathrm{d}H_x + \int_{M_y(0),H_y(0)}^{M_y(c\mathcal{T}),H_y(c\mathcal{T})} M_y \, \mathrm{d}H_y + \\ + \int_{M_z(0),H_z(0)}^{M_z(c\mathcal{T}),H_z(c\mathcal{T})} M_z \, \mathrm{d}H_z \bigg]. \tag{2.52}$$

If the magnetic field is one-dimensional (only present at the $\hat{\mathbf{z}}$ direction), such that $H_x = H_y = 0$, only the area of $\overline{M}_z$ and H_z contributes for the internal energy, that is,

$$\Delta U = -\mu_0 \int_{M_z(0),H_z(0)}^{M_z(c\mathcal{T}),H_z(c\mathcal{T})} M_z \, \mathrm{d}H_z, \tag{2.53}$$

which is the same equation deduced by Rosensweig (2002) under the same set of hypothesis. For a longer time of simulation, more cycles of $\mathbf{M}$ and $\mathbf{H}$ are elapsed and the value of ΔU increases indefinitely, considering an ideal system without loss of energy. To solve this problem, it is defined the average rate of the magnetic contribution of internal energy dissipation of the system, $\dfrac{\Delta U}{\Delta t}$,

$$\frac{\Delta U}{\Delta t} = \frac{\Delta U}{t_f - 0} = -\frac{\mu_0}{t_f} \int_{\mathbf{M}(0),\mathbf{H}(0)}^{\mathbf{M}(c\mathcal{T}),\mathbf{H}(c\mathcal{T})} \mathbf{M} \cdot \mathrm{d}\mathbf{H} \tag{2.54}$$

In such manner, it is guaranteed that $\Delta U / \Delta t_f$ is a converging value that that measures the thermic state of the system, when enough time of simulation and a steady-state condition are reached.

However, some assumptions made in usual MH studies are no longer valid in this work. Because the system studied is nonlinear, the periodic behavior for the magnetization can not be imposed. Furthermore, one of the objectives of the work is to impose a chaotic behavior for the magnetic field, such that the periodic assumption of $\mathbf{H}$ is not valid. Several conditions of $\mathbf{H}$ and $\mathbf{M}$ are considered in this work. Because of this, one must use the most general expression for ΔU, which leads to Eq. (2.55),

$$\Delta U = \mu_0 \int_{\mathbf{M}(0),\mathbf{H}(0)}^{\mathbf{M}(t_f),\mathbf{H}(t_f)} \mathbf{H} \cdot \mathrm{d}\mathbf{M} + \frac{\mu_0}{2} \left[\|\mathbf{H}\| \left(t_f\right)^2 - \|\mathbf{H}\| \left(0\right)^2 \right] \tag{2.55}$$

In this work, the average magnetization, $\overline{\mathbf{M}}$, is used instead of $\mathbf{M}$. Only the steady-state response of $\overline{\mathbf{M}}$ is considered, that is, the initial part of the time response is discarded,

$$\Delta U = \mu_0 \int_{\overline{\mathbf{M}}(0),\mathbf{H}(0)}^{\overline{\mathbf{M}}(t_f),\mathbf{H}(t_f)} \mathbf{H} \cdot \mathrm{d}\overline{\mathbf{M}} + \frac{\mu_0}{2} \left[\|\mathbf{H}\| \left(t_f\right)^2 - \|\mathbf{H}\| \left(0\right)^2 \right] \tag{2.56}$$

such that the average rate of internal energy in steady-state is

$$\frac{\Delta U}{\Delta t} = \frac{1}{t_f} \left\{ \mu_0 \int_{\overline{\mathbf{M}}(0),\mathbf{H}(0)}^{\overline{\mathbf{M}}(t_f),\mathbf{H}(t_f)} \mathbf{H} \cdot \mathrm{d}\overline{\mathbf{M}} + \frac{\mu_0}{2} \left[\|\mathbf{H}\| \left(t_f\right)^2 - \|\mathbf{H}\| \left(0\right)^2 \right] \right\} \tag{2.57}$$

Equation (2.57) is the most general expression for the average rate of internal energy dissipation of the system. In Chapter 4: Results of Alternating Magnetic Field and Chapter 5: Results of Alternating Magnetic Field with Shear Motion, a one-dimensional ($\hat{\mathbf{z}}$ direction) periodic magnetic field is applied, such that the average rate of internal energy is given by

$$\frac{\Delta U}{\Delta t} = \frac{\mu_0}{t_f} \left[\int_{\overline{M}_z(0),H_z(0)}^{\overline{M}_z(t_f),H_z(t_f)} H_z \, \mathrm{d}\overline{M}_z \right] \tag{2.58}$$

In Chapter 6: Results of Chaotic Magnetic Field, a two-dimensional ($\hat{\mathbf{y}}$ and $\hat{\mathbf{z}}$ directions) chaotic magnetic field is applied, such that the average rate of internal energy dissipation is given by

$$\frac{\Delta U}{\Delta t} = \frac{1}{t_f} \left\{ \mu_0 \left[\int_{\overline{M}_y(0),H_y(0)}^{\overline{M}_y(t_f),H_y(t_f)} H_y \, \mathrm{d}\overline{M}_y + \int_{\overline{M}_z(0),H_z(0)}^{\overline{M}_z(t_f),H_z(t_f)} H_z \, \mathrm{d}\overline{M}_z \right] + \right.$$
$$\left. + \frac{\mu_0}{2} \left[H_y \left(t_f\right)^2 + H_z \left(t_f\right)^2 - H_y \left(0\right)^2 - H_z \left(0\right)^2 \right] \right\} \tag{2.59}$$

Thus, to determine the most efficient way of generating internal energy in MH, the condition of the system which maximizes the value of $\Delta U/\Delta t$ will be considered as the best case scenario for the MH cancer treatment.

2.6 Dimensionless Equations

2.6.1 Dimensionless Governing Equations

In this section, the dimensionless forms of Eqs. (2.8) and (2.9) are obtained. To do so, dimensionless variables are introduced in Eq. (2.60),

$$t^* = \frac{tU_{st}}{a}, \quad \mathbf{u}_i^* = \frac{\mathbf{u}_i}{U_{st}}, \quad \boldsymbol{\omega}_i^* = \frac{\boldsymbol{\omega}_i a}{U_{st}} \quad \text{and} \quad \mathbf{g}^* = \frac{\mathbf{g}}{g}, \tag{2.60}$$

where the superscript $*$ indicates a dimensionless quantity, $U_{st} = \dfrac{2\Delta\rho g a^2}{9\eta}$ is the particle's terminal velocity from Stokes' law and $g = \|\mathbf{g}\|$.

Thus, with a process detailed in appendix A, one can obtain the dimensionless governing equations of the system, given by Eqs. (2.61) and (2.62),

$$\text{St}\,\frac{\mathrm{d}\mathbf{u}_i^*}{\mathrm{d}t^*} = -\mathbf{u}_i^* + \mathbf{g}^* + \mathbf{F_{B}}_i^* + \mathbf{F_{m}}_i^* + \mathbf{F_{r}}_i^* + \mathbf{F_{c}}_i^*, \tag{2.61}$$

$$\text{St}_r\,\frac{\mathrm{d}\boldsymbol{\omega}_i^*}{\mathrm{d}t^*} = -\boldsymbol{\omega}_i^* + \mathbf{T_{B}}_i^* + \mathbf{T_{m}}_i^* \tag{2.62}$$

where $\text{St} = \dfrac{\mathcal{M}U_{st}}{6\pi\eta a^2} = 0.1$ is the translational Stokes number, which is defined by the ratio between scales of the relaxation time of particle and its convection time. Similarly, $\text{St}_r = \dfrac{\mathcal{I}U_{st}}{8\pi\eta a^4} = 0.01$ is the rotational Stokes number. For the dimensionless forces and torques, consider the dimensionless constants given by Eq. (2.63),

$$\text{Pe} = \frac{U_{st}a}{\mathcal{D}_t}, \quad \text{Pe}_r = \frac{U_{st}}{a\mathcal{D}_r}, \quad \alpha = \frac{\mu_0 m H}{K_b T}, \quad \text{and} \quad \lambda = \frac{\mu_0 m^2}{4\pi K_b T \left(2a\right)^3}, \tag{2.63}$$

in which Pe is the translational Peclet number, which indicates the ratio between the brownian difusion time and the convection time of the MNP, Pe_r is the rotational Peclet number, α is the Langevin parameter, defined as the ratio between the magnetic force due to the external magnetic field (dipole-field interaction) with the brownian force, and λ is the dipolar interaction parameter, that measures the ratio of the magnetic force from dipole-dipole interactions and brownian force (Gontijo; Cunha, 2015). Diving Pe_r and Pe, one can obtain $\dfrac{\text{Pe}_r}{\text{Pe}} = \dfrac{4}{3}$, such that it is applied the value $\text{Pe}_r = \dfrac{4}{3}\text{Pe}$ in this study.

The dimensionless magnetic force and torque from Eqs. (2.61) and (2.62) are given by Eqs. (2.64) and (2.65),

$$\mathbf{F_m}_i^* = \frac{24\lambda}{\mathrm{Pe}}\Bigg\{ \sum_{\substack{j=1 \\ j\neq i}}^{N} \frac{1}{r_{ij}^{*\,4}} \Big[\left(\hat{\mathbf{d}}_i \cdot \hat{\mathbf{d}}_j\right)\hat{\mathbf{r}}_{ij} + \left(\hat{\mathbf{d}}_i \cdot \hat{\mathbf{r}}_{ij}\right)\hat{\mathbf{d}}_j + \left(\hat{\mathbf{d}}_j \cdot \hat{\mathbf{r}}_{ij}\right)\hat{\mathbf{d}}_i +$$

$$- 5\left(\hat{\mathbf{d}}_i \cdot \hat{\mathbf{r}}_{ij}\right)\left(\hat{\mathbf{d}}_j \cdot \hat{\mathbf{r}}_{ij}\right)\hat{\mathbf{r}}_{ij} \Big] \Bigg\} \quad (2.64)$$

$$\mathbf{T_m}_i^* = \frac{24\lambda}{\mathrm{Pe}_r}\Bigg\{ \sum_{\substack{j=1 \\ j\neq i}}^{N} \frac{1}{r_{ij}^{*\,3}} \Big[-\frac{1}{3}\left(\hat{\mathbf{d}}_i \times \hat{\mathbf{d}}_j\right) + \left(\hat{\mathbf{d}}_j \cdot \hat{\mathbf{r}}_{ij}\right)\left(\hat{\mathbf{d}}_i \times \hat{\mathbf{r}}_{ij}\right) \Big] \Bigg\} +$$

$$+ \frac{\alpha}{\mathrm{Pe}_r}\left(\hat{\mathbf{d}}_i \times \hat{\mathbf{H}}\right) \quad (2.65)$$

The dimensionless brownians force and torque from Eqs. (2.61) and (2.62) are given by Eqs. (2.66) and (2.67),

$$\mathbf{F_B}_i^* = \left(\frac{6}{\mathrm{Pe}\ \delta\tau^*}\right)^{1/2}\boldsymbol{\xi} \quad (2.66)$$

$$\mathbf{T_B}_i^* = \left(\frac{6}{\mathrm{Pe}_r\ \delta\tau^*}\right)^{1/2}\boldsymbol{\xi} \quad (2.67)$$

where $\delta\tau^* = \dfrac{\delta\tau U_{st}}{a}$ is the dimensionless time step related to brownian fluctuations.

The dimensionless contact and repulsive forces from Eq. (2.61) are described by Eqs. (2.68) and (2.69),

$$\mathbf{F_r}_i^* = C_1 u_i^* \exp\left(-\frac{\epsilon_{ij}^*}{C_2^*}\right)\hat{\mathbf{r}}_{ij} \quad (2.68)$$

$$\mathbf{F_c}_i^* = P_c \epsilon_{ij}^{*\,3/2}\,\hat{\mathbf{r}}_{ij}. \quad (2.69)$$

in which $C_2^* = C_2/a$ is the dimensionless calibration constant related to the range of the field, $\epsilon_{ij}^* = \epsilon_{ij}/a$ is the dimensionless distance between the surfaces of the i-th and j-th particles and $P_c = \dfrac{C_3 \varepsilon a^2}{6\sqrt{2}\pi\eta a U_{st}}$ is the dimensionless contact parameter that relates the contact force and hydrodynamics drag force. The value $P_c = 100$ has been adopted for all simulations.

2.6.2 Dimensionless Shear Rate

The translational shear motion is given by

$$\mathbf{u_{sh}}_i = \mathbf{u}_i + (0, \dot{\gamma}z, 0). \quad (2.70)$$

Dividing both sides by U_{st},

$$\frac{\mathbf{u_{sh}}_i}{U_{st}} = \frac{\mathbf{u}_i}{U_{st}} + \left(0, \frac{\dot{\gamma}z}{U_{st}}, 0\right). \tag{2.71}$$

Apply $z = az^*$, where z^* is the nondimensional height of the particle,

$$\frac{\mathbf{u_{sh}}_i}{U_{st}} = \frac{\mathbf{u}_i}{U_{st}} + \left(0, \frac{a\dot{\gamma}}{U_{st}}z^*, 0\right). \tag{2.72}$$

Let $\dot{\gamma}^* = \dfrac{a\dot{\gamma}}{U_{st}}$ be the dimensionless shear rate and $\mathbf{u_{sh}}_i^* = \dfrac{\mathbf{u_{sh}}_i}{U_{st}}$ the dimensionless velocity of the system under shear motion. Thus,

$$\mathbf{u_{sh}}_i^* = \mathbf{u}_i^* + (0, \dot{\gamma}^* z^*, 0). \tag{2.73}$$

For the rotational motion,

$$\boldsymbol{\omega_{sh}}_i = \boldsymbol{\omega}_i + \left(\frac{1}{2}\dot{\gamma}, 0, 0\right). \tag{2.74}$$

Multiply both sides by $\dfrac{U_{st}}{a}$

$$\frac{U_{st}}{a}\boldsymbol{\omega_{sh}}_i = \frac{U_{st}}{a}\boldsymbol{\omega}_i + \left(\frac{U_{st}}{2a}\dot{\gamma}, 0, 0\right). \tag{2.75}$$

Let $\boldsymbol{\omega_{sh}}_i^* = \dfrac{\boldsymbol{\omega_{sh}}_i}{U_{st}}$ be the dimensionless angular velocity of the i-th particle when shear motion is activated. As $\dot{\gamma}^* = \dfrac{a\dot{\gamma}}{U_{st}}$ is the dimensionless shear rate, it is obtained

$$\boldsymbol{\omega_{sh}}_i^* = \boldsymbol{\omega}_i^* + \left(\frac{\dot{\gamma}^*}{2}, 0, 0\right). \tag{2.76}$$

For the kinematics of the dipoles orientation, there is

$$\frac{\mathrm{d}}{\mathrm{d}t}\hat{\mathbf{d}}_i = \boldsymbol{\omega_{sh}}_i \times \hat{\mathbf{d}}_i. \tag{2.77}$$

Substitute $t^* = \dfrac{U_{st}t}{a}$,

$$\frac{a}{U_{st}} \frac{\mathrm{d}}{\mathrm{d}t^*} \hat{\mathbf{d}}_i = \boldsymbol{\omega}_{\mathbf{sh}i} \times \hat{\mathbf{d}}_i, \tag{2.78}$$

$$\implies \frac{\mathrm{d}}{\mathrm{d}t^*} \hat{\mathbf{d}}_i = \left(\frac{U_{st}}{a} \boldsymbol{\omega}_{\mathbf{sh}i}\right) \times \hat{\mathbf{d}}_i. \tag{2.79}$$

As $\boldsymbol{\omega}_{\mathbf{sh}i}^* = \dfrac{U_{st}}{a} \boldsymbol{\omega}_{\mathbf{sh}i}$, it can be concluded that

$$\frac{\mathrm{d}}{\mathrm{d}t^*} \hat{\mathbf{d}}_i = \boldsymbol{\omega}_{\mathbf{sh}i}^* \times \hat{\mathbf{d}}_i. \tag{2.80}$$

2.6.3   Dimensionless Average Magnetization

To calculate the maximum magnetization of the system of particles, consider that all dipoles are aligned in the same direction, such that $\hat{\mathbf{d}}_i = \hat{\mathbf{z}}$. So,

$$\mathbf{m}_i = m\hat{\mathbf{d}}_i, \quad i = 1, \ldots, N \tag{2.81}$$

$$\implies \mathbf{m}_i = m\hat{\mathbf{z}}, \quad i = 1, \ldots, N. \tag{2.82}$$

As such, the maximum magnetization (saturation magnetization) is given by Eq. (2.83)

$$\mathbf{M} = M_s\hat{\mathbf{z}} = \frac{1}{V} \sum_{i=1}^{N} \mathbf{m}_i = \frac{1}{V} \sum_{i=1}^{N} m\hat{\mathbf{z}} = \frac{m}{V} \left(\sum_{i=1}^{N} \hat{\mathbf{z}}\right) = \frac{m}{V} (N\hat{\mathbf{z}}) = \left(\frac{N}{V}\right) m\hat{\mathbf{z}} = nm\hat{\mathbf{z}} \tag{2.83}$$

$$\therefore M_s = nm. \tag{2.84}$$

Hence, the scale M_s is chosen to nondimensionalize the magnetization. Consequently, the dimensionless magnetization, $\mathbf{M}^*$, is given by Eq. (2.85)

$$\mathbf{M}^* = \frac{\mathbf{M}}{M_s} = \frac{\mathbf{M}}{nm}. \tag{2.85}$$

As such, the dimensionless magnetization is determined only by the average of $\hat{\mathbf{d}}_i$,

$$\mathbf{M}^* = \frac{1}{nm} \mathbf{M} = \frac{1}{nm} \left(\frac{n}{N} \sum_{i=1}^{N} \mathbf{m}_i\right) = \frac{1}{nm} \left(\frac{nm}{N} \sum_{i=1}^{N} \hat{\mathbf{d}}_i\right) = \frac{1}{N} \sum_{i=1}^{N} \hat{\mathbf{d}}_i. \tag{2.86}$$

Thus, the dimensionless average magnetization is given by

$$\overline{\mathbf{M}}^* = \frac{1}{K} \sum_{k=1}^{K} \mathbf{M}_k^*. \tag{2.87}$$

2.6.4 Dimensionless Average Rate of Internal Energy Dissipation

To obtain the nondimensionalized form of the average rate of internal energy per unit volume, one must apply equations $\overline{\mathbf{M}} = M_s \overline{\mathbf{M}}^*$, $\mathbf{H} = H\hat{\mathbf{H}}$ and $t_f = at_f^*/U_{st}$ in Eq. (2.57). Thus,

$$\frac{\Delta U}{\Delta t} = \frac{U_{st}}{at_f^*}\left\{\mu_0 \int_{\overline{\mathbf{M}}^*(0),\hat{\mathbf{H}}(0)}^{\overline{\mathbf{M}}^*\left(t_f^*\right),\hat{\mathbf{H}}\left(t_f^*\right)} \left(H\hat{\mathbf{H}}\right) \cdot \mathrm{d}\left(M_s\overline{\mathbf{M}}^*\right) + \right.$$
$$\left. + \frac{\mu_0 H^2}{2}\left[\|\hat{\mathbf{H}}\|\left(t_f^*\right)^2 - \|\hat{\mathbf{H}}\|\,(0)^2\right]\right\} \quad (2.88)$$

$$\implies \frac{\Delta U}{a\Delta t/U_{st}} = \frac{1}{t_f^*}\left\{\mu_0 \int_{\overline{\mathbf{M}}^*(0),\hat{\mathbf{H}}(0)}^{\overline{\mathbf{M}}^*\left(t_f^*\right),\hat{\mathbf{H}}\left(t_f^*\right)} \left(H\hat{\mathbf{H}}\right) \cdot \mathrm{d}\left(M_s\overline{\mathbf{M}}^*\right) + \right.$$
$$\left. + \frac{\mu_0 H^2}{2}\left[\|\hat{\mathbf{H}}\|\left(t_f^*\right)^2 - \|\hat{\mathbf{H}}\|\,(0)^2\right]\right\} \quad (2.89)$$

Let $\Delta t^* = a\Delta t/U_{st}$ be the nondimensionalized variation of time. So,

$$\implies \frac{\Delta U}{\Delta t^*} = \frac{1}{t_f^*}\left\{\mu_0 \int_{\overline{\mathbf{M}}^*(0),\hat{\mathbf{H}}(0)}^{\overline{\mathbf{M}}^*\left(t_f^*\right),\hat{\mathbf{H}}\left(t_f^*\right)} \left(H\hat{\mathbf{H}}\right) \cdot \mathrm{d}\left(M_s\overline{\mathbf{M}}^*\right) + \right.$$
$$\left. + \frac{\mu_0 H^2}{2}\left[\|\hat{\mathbf{H}}\|\left(t_f^*\right)^2 - \|\hat{\mathbf{H}}\|\,(0)^2\right]\right\} \quad (2.90)$$

$$\implies \frac{\Delta U}{\Delta t^*} = \frac{\mu_0 H M_s}{t_f^*}\left\{\int_{\overline{\mathbf{M}}^*(0),\hat{\mathbf{H}}(0)}^{\overline{\mathbf{M}}^*\left(t_f^*\right),\hat{\mathbf{H}}\left(t_f^*\right)} \hat{\mathbf{H}} \cdot \mathrm{d}\overline{\mathbf{M}}^* + \right.$$
$$\left. + \frac{H}{2M_s}\left[\|\hat{\mathbf{H}}\|\left(t_f^*\right)^2 - \|\hat{\mathbf{H}}\|\,(0)^2\right]\right\} \quad (2.91)$$

$$\implies \left(\frac{1}{\mu_0 H M_s}\right)\frac{\Delta U}{\Delta t^*} = \frac{1}{t_f^*}\left\{\int_{\overline{\mathbf{M}}^*(0),\hat{\mathbf{H}}(0)}^{\overline{\mathbf{M}}^*\left(t_f^*\right),\hat{\mathbf{H}}\left(t_f^*\right)} \hat{\mathbf{H}} \cdot \mathrm{d}\overline{\mathbf{M}}^* + \right.$$
$$\left. + \frac{H}{2M_s}\left[\|\hat{\mathbf{H}}\|\left(t_f^*\right)^2 - \|\hat{\mathbf{H}}\|\,(0)^2\right]\right\} \quad (2.92)$$

Let $\Delta U^* = \dfrac{\Delta U}{\mu_0 H M_s}$ be the nondimensionalized variation of internal energy per unit volume. Hence,

$$\implies \frac{\Delta U^*}{\Delta t^*} = \frac{1}{t_f^*}\left\{\int_{\overline{\mathbf{M}}^*(0),\hat{\mathbf{H}}(0)}^{\overline{\mathbf{M}}^*\left(t_f^*\right),\hat{\mathbf{H}}\left(t_f^*\right)} \hat{\mathbf{H}} \cdot \mathrm{d}\overline{\mathbf{M}}^* + \frac{H}{2M_s}\left[\|\hat{\mathbf{H}}\|\left(t_f^*\right)^2 - \|\hat{\mathbf{H}}\|\,(0)^2\right]\right\} \quad (2.93)$$

in which $\dfrac{\Delta U^*}{\Delta t^*}$ is the dimensionless average rate of internal energy.

Note that

$$\frac{\alpha}{24\phi\lambda} = \left(\frac{\mu_0 m H}{K_b T}\right)\left(\frac{4\pi K_b T (2a)^3}{\mu_0 m^2}\right)\frac{1}{24\phi} = \left(\frac{4\pi (2a)^3 H}{m}\right)\frac{1}{24\phi} = \left(\frac{4\pi a^3 H}{m}\right)\frac{1}{3\phi} \quad (2.94)$$

Once $v_i = \dfrac{4\pi a^3}{3}$ is the volume of a MNP,

$$\implies \frac{\alpha}{24\phi\lambda} = \frac{v_i H}{\phi m} \quad (2.95)$$

Using $\phi = \dfrac{N}{V} v_i = n v_i$,

$$\implies \frac{\alpha}{24\phi\lambda} = \frac{v_i H}{n v_i m} = \frac{H}{nm} \quad (2.96)$$

Applying $M_s = nm$,

$$\implies \frac{\alpha}{24\phi\lambda} = \frac{H}{M_s} \quad (2.97)$$

The substitution of Eq. (2.97) into (2.93) yields the most general expression for the dimensionless average rate of internal energy dissipation,

$$\frac{\Delta U^*}{\Delta t^*} = \frac{1}{t_f^*}\left\{\int_{\overline{\mathbf{M}}^*(0),\hat{\mathbf{H}}(0)}^{\overline{\mathbf{M}}^*(t_f^*),\hat{\mathbf{H}}(t_f^*)} \hat{\mathbf{H}} \cdot \mathrm{d}\overline{\mathbf{M}}^* + \frac{\alpha}{48\phi\lambda}\left[\|\hat{\mathbf{H}}\|\left(t_f^*\right)^2 - \|\hat{\mathbf{H}}\|\left(0\right)^2\right]\right\} \quad (2.98)$$

In Chapter 4: Results of Alternating Magnetic Field and Chapter 5: Results of Alternating Magnetic Field with Shear Motion, a one-dimensional ($\hat{\mathbf{z}}$ direction) periodic magnetic field is applied, such that the dimensionless average rate of internal energy is given by

$$\frac{\Delta U^*}{\Delta t^*} = \frac{1}{t_f^*}\left[\int_{\overline{M}_z^*(0),\hat{H}_z(0)}^{\overline{M}_z^*(t_f^*),\hat{H}_z(t_f^*)} \hat{H}_z\, \mathrm{d}\overline{M}_z^*\right] \quad (2.99)$$

In Chapter 6: Results of Chaotic Magnetic Field a two-dimensional ($\hat{\mathbf{y}}$ and $\hat{\mathbf{z}}$ directions) chaotic magnetic field is applied, such that the dimensionless average rate of internal energy is given by

$$\frac{\Delta U^*}{\Delta t^*} = \frac{1}{t_f^*} \left\{ \int_{\overline{M}_y^*(0),\hat{H}_y(0)}^{\overline{M}_y^*\left(t_f^*\right),\hat{H}_y\left(t_f^*\right)} \hat{H}_y \, \mathrm{d}\overline{M}_y^* + \int_{\overline{M}_z^*(0),\hat{H}_z(0)}^{\overline{M}_z^*\left(t_f^*\right),\hat{H}_z\left(t_f^*\right)} \hat{H}_z \, \mathrm{d}\overline{M}_z^* + \right.$$

$$\left. + \frac{\alpha}{48\phi\lambda} \left[\hat{H}_y\left(t_f^*\right)^2 + \hat{H}_z\left(t_f^*\right)^2 - \hat{H}_y(0)^2 - \hat{H}_z(0)^2 \right] \right\} \quad (2.100)$$

In Eq. (2.100), one can see negative terms, such that it is possible to obtain $\frac{\Delta U^*}{\Delta t^*} < 0$. This represents a cooling effect due to magnetic refrigeration.

2.7   Algorithm Methods

2.7.1   Numerical Integration Method

The Runge-Kutta of 4-th order numerical method is applied to integrate the nondimensionlized governing equations. To do so, the system is simulated through an open source in-house Fortran code with fixed time steps (Gontijo; Cunha, 2015). Several realizations of the simulation are performed, with the purpose of acquiring consistent statistical data. The numerical time step used in all simulations is given by Eq. (2.101),

$$h = \min\left(\frac{\mathrm{St}}{10}, \frac{\mathrm{Pe}}{10}, 0.01 \right), \quad (2.101)$$

in which h is the dimensionless time step.

2.7.2   Procedure to Avoid Aggregation of Particles

To prevent particle agglomeration, one must simulate the effect of the surfactant, which stabilizes the ferrofluid (Huang et al., 2017). Thus, the magnetic force is deactivated for near particles (Gontijo; Cunha, 2015). As the attraction dipole-dipole force is proportional to $1/r_{ij}^4$, the magnetic force is extraordinary intense in short distances. As a consequence, if the magnetic force is considered in near particles during the simulation, particle's agglomeration and superposition will occur.

Thus, according to Gontijo and Cunha (2015), the magnetic force is made inactive for the optimized range of $r_{ij} < 10a$. To exemplify this, Fig. 2.9 shows the moment when the magnetic force is disabled for 2 isolated particles. Throughout all time steps in the simulation, the distance between all particles is verified, such that, if a pair of spheres approaches each other, their magnetic forces are equal to zero.
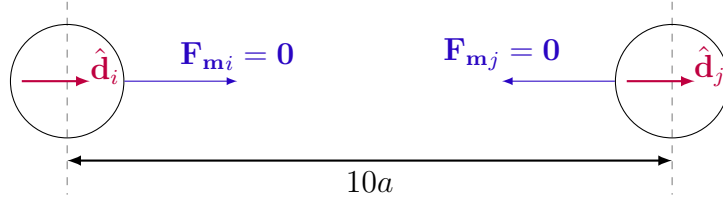
Figure 2.9 – Distance which the dipole-dipole magnetic force between two particles is deactivated to avoid agglomeration. Figure adapted from Gontijo and Cunha (2015).

2.7.3 Periodic Magnetic Torque

This section describes a algorithm method used only for cases with $\phi > 1\%$ and $\lambda > 1$. To compute long range interactions between particles, such as velocities and torques caused by motion, particles cells are periodically replicated through the suspension volume (Gontijo; Cunha, 2015). With this, the effect of an infinite suspension can be simulated (Cunha et al., 2002). As a result, there are hundreds of imaginary cells around a central cell in the simulation. To harvest the results, data is obtained only from the central cell, which is influenced by the neighborhood cells. Fig. 2.10 illustrates a simplified example, with 8 imaginary cells and 1 central cell, to represent a system with particles periodically replicated through the volume.

In Fig. 2.10, because the number of particles increased with the system's replication, the computational time to simulate the system has increased as well. Thus, to compute the calculations of the dipole-dipole interactions in a faster way, Ewald summation on the physical and reciprocal space is applied (Ewald, 1921), (Beenakker, 1986), (Cunha et al., 2002). In this work, 125 lattices are used in the physical domain and 125 lattices in the reciprocal domain, couting 250 lattices in total.

Hence, the nondimensionalized magnetic torque applied in the i-th particle under the influence of particles from the central lattice and neighbor lattices periodically distributed is given by Eqs.(2.102), (2.103), (2.104), (2.105), (2.106) and (2.107),
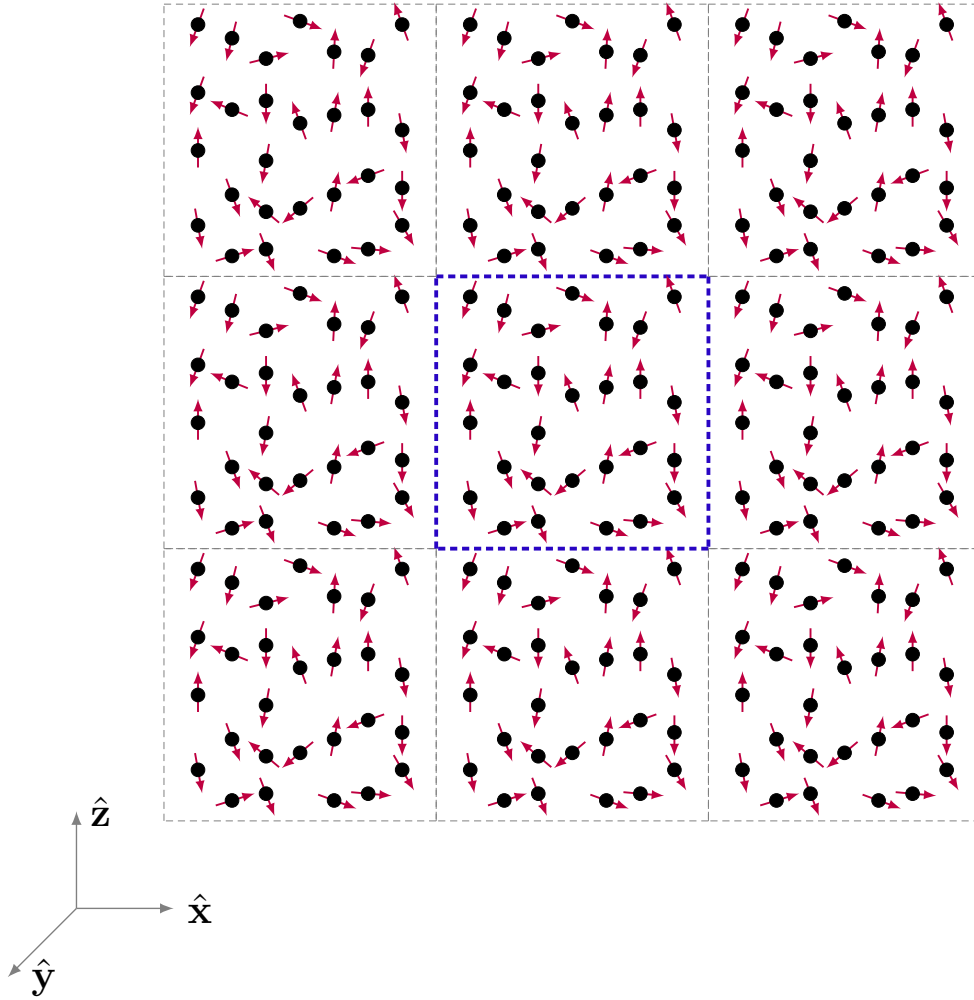
Figure 2.10 – Schematic of the simulation's physical domain. The central cell (in blue) is replicated into imaginary cells (in gray), to compute the effect of a suspension. Figure adapted from Cunha et al. (2002).

$$\mathbf{T_{mp}}_i^* = \left[-\frac{8\lambda}{\mathrm{Pe}_r} \sum_{x \in \mathcal{L}} \boldsymbol{\mathcal{T}}_1(x) + \frac{1}{L^3} \sum_{\substack{x \in \overline{\mathcal{L}} \\ k \neq 0}} \boldsymbol{\mathcal{T}}_2(k) \right] + \frac{\alpha}{\mathrm{Pe}_r} \left(\hat{\mathbf{d}}_i \times \hat{\mathbf{H}} \right), \qquad (2.102)$$

$$\boldsymbol{\mathcal{T}}_1(x) = \left(\hat{\mathbf{d}}_i \times \hat{\mathbf{d}}_j \right) \mathcal{B} \left(r_{ij} \right) - \left(\hat{\mathbf{d}}_i \times \hat{\mathbf{r}}_{ij} \right) \left(\hat{\mathbf{d}}_j \cdot \hat{\mathbf{r}}_{ij} \right) \mathcal{C} \left(r_{ij} \right), \qquad (2.103)$$

$$\boldsymbol{\mathcal{T}}_2(k) = 4\pi \left(\hat{\mathbf{d}}_i \times \hat{\mathbf{k}} \right) \left(\hat{\mathbf{d}}_j \cdot \hat{\mathbf{k}} \right) e^{\left(\pi k / \xi \right)^2} \cos \left(2\pi \hat{\mathbf{k}} \cdot \hat{\mathbf{r}}_{ij} \right), \qquad (2.104)$$

$$\mathcal{B} \left(r_{ij} \right) = \left[\mathrm{erfc}(\xi r_{ij}) + \left(\frac{2\xi r_{ij}}{\sqrt{\pi}} \right) e^{\left(-\xi^2 r_{ij}^2 \right)} \right] r_{ij}^{-3}, \qquad (2.105)$$

$$\mathcal{C} \left(r_{ij} \right) = \left(\frac{2\xi r_{ij}}{r_{ij}^4 \sqrt{\pi}} \right) \left(3 + 2\xi^2 r_{ij}^2 \right) e^{\left(-\xi^2 r_{ij}^2 \right)} + \frac{3 \, \mathrm{erfc}(\xi r_{ij})}{r_{ij}^4}, \qquad (2.106)$$

$$\mathrm{erfc}(x) = 1 - \frac{2}{\sqrt{\pi}} \int_0^x e^{-t^2} \mathrm{d}t, \qquad (2.107)$$

where $\boldsymbol{\mathcal{T}}_1(x)$ is a function from the physical domain, $\boldsymbol{\mathcal{T}}_2(k)$ is a function from the reciprocal domain, $\hat{\mathbf{k}}$ is the wavenumber unit vector, $\mathcal{B} \left(r_{ij} \right)$ and $\mathcal{C} \left(r_{ij} \right)$ are scalar functions and erfc(x) is the complementary error function. The parameter ξ dictates the convergence of

the method (Gontijo; Cunha, 2015). In this work, the value $\xi = \pi^{1/2}V^{-1/3}$ is used, where V is the volume of the central cell (Beenakker, 1986). When the condition of periodic magnetic torques is activated, the magnetic torque $\mathbf{T_{m}}_i^*$ is replaced by $\mathbf{T_{mp}}_i^*$.

3 Nonlinear Dynamics and Signal Processing

> "*Mathematics is the art of giving the same name to different things.*"
>
> Henri Poincaré

This chapter is focused on explaining the nonlinear tools used in this work.

3.1 Poincaré Map

The Poincaré map or return map is a tool used to describe different types of oscillations in dynamical systems (Seydel, 2009). As stated by Seydel (2009), it is usually applied to describe stability for periodic orbits. The Poincaré map transforms a continuous time system into a discrete time system, allowing the study of a lower dimensional problem. To obtain the map, one must define a hypersurface (Poincaré section) in the phase space, such that all trajectories intersects the surface transversally and in the same direction. In other words, the Poincaré map is a stroboscopically portrait of the system. However, there is no general procedure to construct a Poincaré Map, because it is necessary a prior knowledge of the system for each case (Wiggins; Wiggins; Golubitsky, 2003).

In this study, once the system analyzed is non-autonomous and the explicit time dependence is given by the forcing function (magnetic field), the Poincaré section is chosen as

$$\Sigma = \left\{ \hat{H}_z = 0, \frac{\mathrm{d}\hat{H}_z}{\mathrm{d}t} > 0 \right\} \tag{3.1}$$

in which Σ is the Poincaré section.

In other words, the values of the Poincaré map are selected when the magnetic field in the $\hat{\mathbf{z}}$ direction has the same phase. Because the simulation values are discrete, to increase precision, interpolation was applied in the Poincaré mapping, to better approximate the phase of $\hat{H}_z$. As an example, Fig. 3.1 shows a typical time response of the magnetization (in purple) with the Poincaré map selected (in green) for a sinusoidal magnetic field, $\hat{H}_z$.
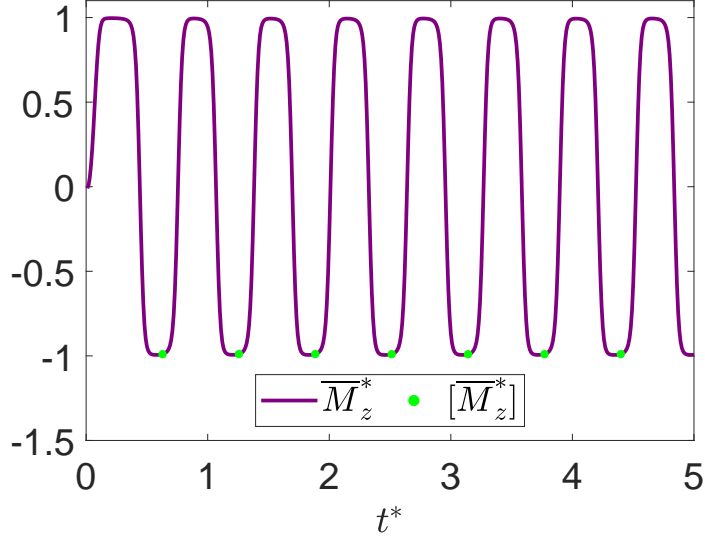
Figure 3.1 – Example of the Poincaré map (in green, $[\overline{M_z}^*]$) of the magnetization time response over time (in purple, $\overline{M_z}^*$).

In Fig. 3.1, as $\overline{\mathbf{M}}^*$ and $\hat{\mathbf{H}}$ are delayed, the point of $[\overline{M_z}^*]$ is reached a little before the complete period of $\overline{M_z}^*$. The time response (in purple) is well-behaved, such that the Poincaré map $[\overline{M_z}^*]$ (in green) is always marked at the same value (approximately $\overline{M_z}^* = -1$). However, if the behavior of two consecutive points is not linear, the points marked by $[\overline{M_z}^*]$ can have very distinct values.

3.2 Bifurcation Diagram

Bifurcation or branching is defined as a qualitative change observed in a system due to the variation of a certain control parameter, λ_c (Seydel, 2009). As this parameter changes and surpasses a threshold value, a different behavior is noticed on the system. As examples of qualitative changes, the system may vary between the state of stable or unstable, regular or irregular, symmetric or asymmetric, ordered or chaotic motions. For instance, the oscillation of an airfoil may achieve chaotic motion as the speed of the plane (control parameter) increases and the condition of turbulence flow is reached.

To observe a qualitative change, a scalar measure of the system's states variables is required. There are several choices for the scalar measure, such as choosing just one arbitrary variable from all states variables at a specific time, selecting the maximum value of all state variables or even the 2-norm of all states variables combined (Seydel, 2009). In this work, the equivalent state variables are the $\hat{\mathbf{x}}$, $\hat{\mathbf{y}}$ and $\hat{\mathbf{z}}$ components of the dimensionless average magnetization, $\overline{\mathbf{M}}^*$. Thus, the notation of scalar measure is given by $[\overline{\mathbf{M}}^*]$ or, more precisely, by its 3 components, $[\overline{M_x}^*]$, $[\overline{M_y}^*]$ and $[\overline{M_z}^*]$.

Hence, the bifurcation diagram, also called as branching diagram or response

35

diagram, is defined as a graph between $\left[\overline{\mathbf{M}}^*\right]$ and λ_c. Regarding the various type of scalar measures, the Poincaré map of $\overline{\mathbf{M}}^*$ is chosen for $\left[\overline{\mathbf{M}}^*\right]$.

For example, two bifurcation diagrams are shown in Fig. 3.2, as the Poincaré map is plotted in the ordinate axis. If the response is periodic, thus, $[u]$ always has the same value (like Fig. 3.1), a bifurcation diagram in Fig. 3.2(a) can be observed (Barbosa et al., 2015). Even with only periodic response, a threshold value of $\lambda_c = \omega \approx 0.4$ is noticed, where the value of $[u]$ is drastically changed, presenting a discontinuity in the bifurcation diagram. If the response is chaotic, the bifurcation diagram in Fig. 3.2(b) can be seen. In this case, the Poincaré map $[u]$ presents various points for the same parameter value after a drastically change from one-to-one map to one-to-many map, as shown by the threshold value of $\lambda_c = f_0 \approx 0.08$. Other threshold values can be observed at $f_0 \approx 0.09$, $f_0 \approx 0.095$ and $f_0 \approx 0.11$.
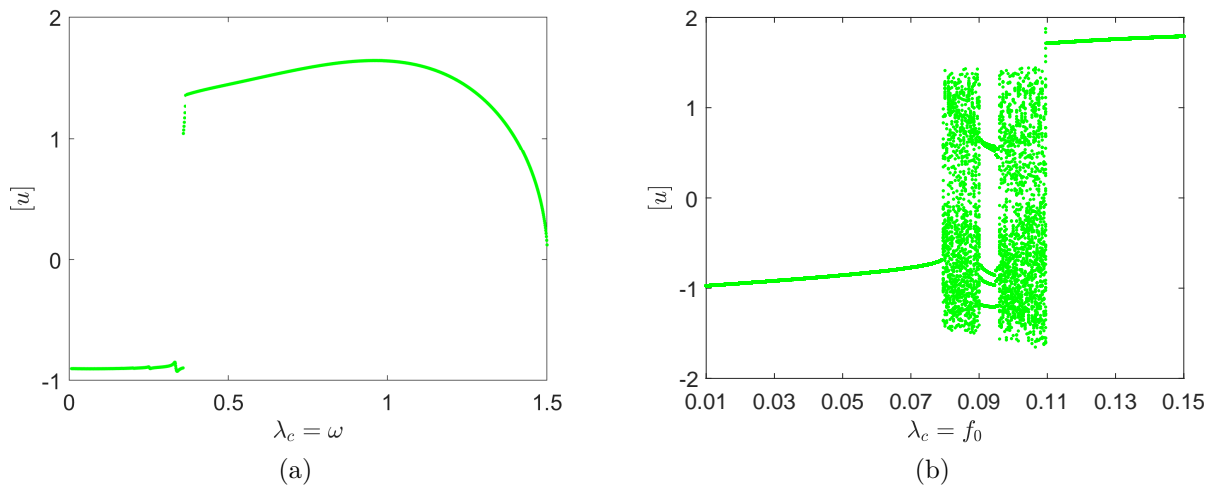
Figure 3.2 – Examples of bifurcation diagrams. (a) Threshold value at $\omega \approx 0.4$. (b) Threshold values at $f_0 \approx 0.08$, $f_0 \approx 0.09$, $f_0 \approx 0.95$ and $f_0 \approx 0.11$

3.3 Fourier Transform

The Fourier transform adopted in this work is given by Eq. (3.2),

$$\mathcal{F}\{M_z^*(t^*)\}(\omega^*) = \int_{-\infty}^{\infty} M_z^*(t^*)e^{-\mathscr{J}\omega^* t^*}\, \mathrm{d}t^*, \tag{3.2}$$

where t^* is the dimensionless time domain, ω^* is the dimensionless angular frequency domain, $\mathscr{J} = \sqrt{-1}$ is the imaginary unit, $M_z^*(t)$ is the time signal and $\mathcal{F}\{M_z^*(t)\}(\omega^*)$ is the Fourier transform of the signal (Shin; Hammond, 2008). The Fast Fourier transform algorithm is applied for discrete time signals.

4 Results of Alternating Magnetic Field

> "*One accurate measurement is worth a thousand expert opinions.*"
>
> Grace Hopper

In this chapter, the magnetization relaxation is evaluated, that corresponds to the system free response just after the magnetic field is turned off. In the sequence, it is analyzed how nondimensional parameters change the system's dynamical behavior. The following one-dimensional alternating magnetic field is considered

$$\hat{\mathbf{H}}(t^*) = \hat{H}_z\hat{\mathbf{z}} = \sin(\omega_H^* t^*)\hat{\mathbf{z}}, \tag{4.1}$$

where ω_H^* is the dimensionless angular frequency associated with the magnetic field. The period of the magnetic field is given by $\mathcal{T}^* = \dfrac{2\pi}{\omega_H^*}$.

As the magnetic field is one-dimensional and periodic, the expression used in this chapter to calculate the dimensionless average rate of internal energy is

$$\frac{\Delta U^*}{\Delta t^*} = \frac{1}{t_f^*}\bigg[\int_{\overline{M}_z^*(0),\hat{H}_z(0)}^{\overline{M}_z^*\left(t_f^*\right),\hat{H}_z\left(t_f^*\right)} \hat{H}_z\,\mathrm{d}\overline{M}_z^*\bigg] = \frac{1}{t_f^*}\bigg[\int_{\overline{M}_z^*(0)}^{\overline{M}_z^*\left(t_f^*\right)} \sin(\omega_H^* t^*)\,\mathrm{d}\overline{M}_z^*\bigg], \tag{4.2}$$

thus, $\dfrac{\Delta U^*}{\Delta t^*}$ is calculated by the hysteresis curve area only in the $\hat{\mathbf{z}}$ direction.

Fig. 4.1 shows the system treated in this chapter. For this case, a one-dimensional sinusoidal magnetic field is applied, given by Eq. (4.1). From the dynamical point of view, the external magnetic vector field can be interpreted as the system excitation.
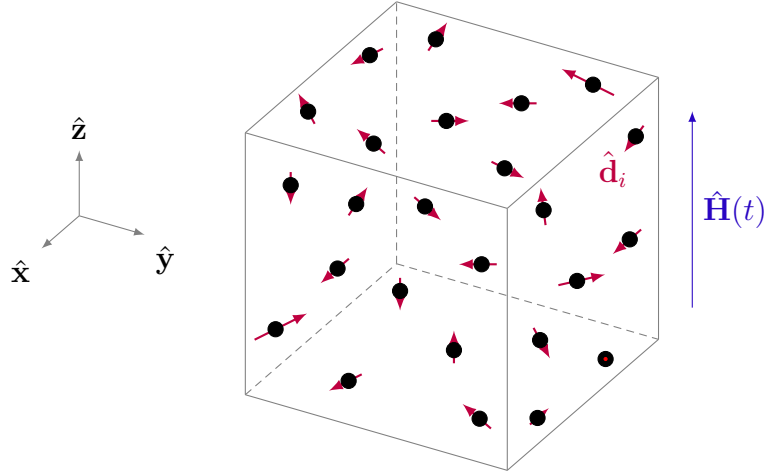
Figure 4.1 – Representation of the system analyzed in this chapter. An external magnetic vector field with harmonic behavior is applied in the $\hat{\mathbf{z}}$ direction, represented by ($\hat{\mathbf{H}}$). Particles are represented by black dots and their dipole vector in red ($\hat{\mathbf{d}}_i$).

4.1 Magnetization Relaxation

In this section, the objective is to study the system's response under relaxation. The system is first excited with an alternating magnetic field, then the effect of the field is deactivated and the system approaches equilibrium. Equation (4.3) shows the applied magnetic field, described as the conditional function

$$\hat{\mathbf{H}}(t^*) = \begin{cases} \sin(\omega_H^* t^*)\hat{\mathbf{z}} & \text{if } 0 \leq t^* < \dfrac{t_f^*}{2}, \\ \mathbf{0} & \text{if } \dfrac{t_f^*}{2} \leq t^* \leq t_f^*, \end{cases} \tag{4.3}$$

where t_f^* is the dimensionless final time of the simulation. The magnetic field becomes inactive when the time of the simulation reaches half of its total. Thus, the magnetization relaxation response correspond to the half final of the response. One can interpret that a rectangular window is applied on the response (Shin; Hammond, 2008). At last, the Fourier transform of the windowed signal is calculated.

4.1.1 Results

Fig. 4.2 shows the results of the magnetization relaxation for $\lambda = 1$, Pe $= 6$ and $\phi = 1\%$ and after a magnetic field with $\alpha = 10$ and $\omega_H^* = 10$ is applied.
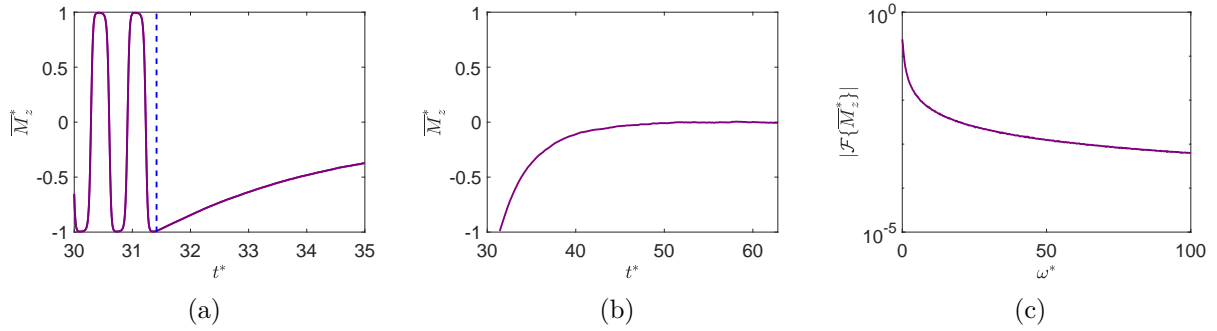
Figure 4.2 – Magnetization relaxation for $\alpha = 10$, $\omega_H^* = 10$, $\lambda = 1$, Pe = 6 and $\phi = 1\%$. (a): Dimensionless time response (in purple) and the cut section used to isolate the relaxation time response. (b): Signal after the cut-off (windowed time response), representing the magnetization under relaxation. (c): Absolute value of the Fourier transform of the windowed signal in logarithm scale.

Fig. 4.2(a) shows the time response, the blue dashed line indicates the moment when the magnetic field is deactivated. When the excited is on, the system oscillates with the same frequency of the magnetic field. After it is turned off, the time response approaches equilibrium. Fig. 4.2(b) shows the time response only in relaxation, when the magnetic field slowly reaches the value of zero. A Fourier transform is constructed from the time response in relaxation, shown in Fig. 4.2(c). One can see that the maximum value of the spectra occurs at $\omega^* = 0$, that is, the system's natural frequency is equal to zero, representing a constant magnetization.

Fig. 4.3 shows the results of the relaxation magnetization varying ϕ for the values: $\alpha = 1$, $\omega_H^* = 1$, $\lambda = 1$ and Pe = 1. Fig. 4.3 (a), (b) and (c) correspond to $\phi = 1\%$ and Fig. 4.3 (d), (e) and (f) correspond to $\phi = 15\%$.
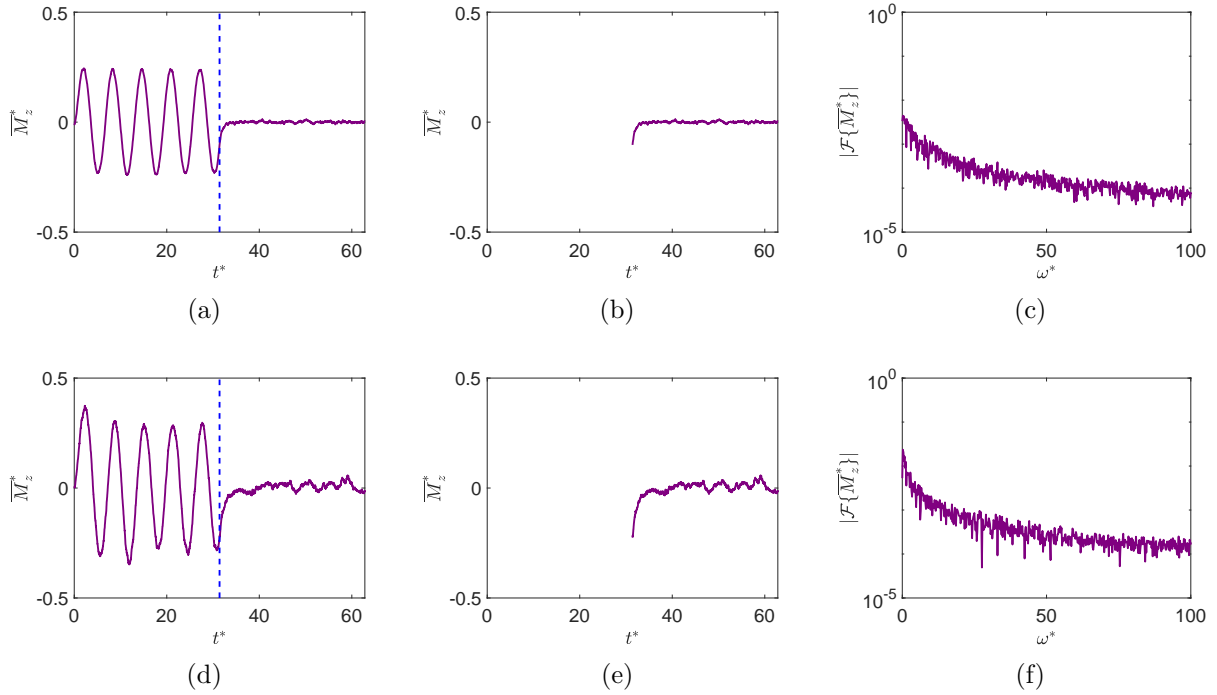
Figure 4.3 – Magnetization relaxation for $\omega_H^* = 1$, $\lambda = 1$, Pe $= 1$ and $\alpha = 1$. (a), (b) and (c): $\phi = 1\%$. (d), (e) and (f): $\phi = 15\%$. (a) and (d): Dimensionless time response (in purple) and the cut section used to isolate the relaxation time response. (b) and (e): Signal after the cut-off (windowed time response), representing the magnetization under relaxation. (c) and (f): Absolute value of the Fourier transform of the windowed signal in logarithm scale.

In Fig. 4.3(a), with $\phi = 1\%$, the system behaves with a well-behaved sine wave before the deactivation of the magnetic field. Analyzing the Fourier transform of the relaxation magnetization in Fig. 4.3(c), the frequency $\omega^* = 0$ has the higher value and the spectra is noisier than 4.2(c). This happens because the influence of the brownian random motion is higher than in the previous case (the lower the Pe, the stronger the brownian force and torque) and the influence of the magnetic field is lower (the lower the α, the weaker the magnetic force and torque).

In Fig. 4.3(d), with $\phi = 15\%$, the system behaves in a very similar way of Fig. 4.3(a), with only a slightly higher amplitude before the relaxation. In Fig. 4.3(e), the system is noisier in the relaxation response, due to the higher number of particles, which increased the particle's collisions with the newtonian fluid. In Fig. 4.3(f), the Fourier transform still indicates the frequency $\omega^* = 0$, but with an even noisier spectra.

As a conclusion, the variation of the volume fraction parameter has not changed significantly the dynamical aspect of the system, as only a null natural frequency is obtained in all cases. The higher the ϕ, the higher the random effect in the time response.

Fig. 4.4 shows the results of the relaxation magnetization varying α for the values: $\phi = 1\%$, $\omega_H^* = 1$, $\lambda = 1$ and Pe $= 1$. Fig. 4.4 (a), (b) and (c) show $\alpha = 1$ and Fig. 4.4 (d),

(e) and (f) show $\alpha = 10$.
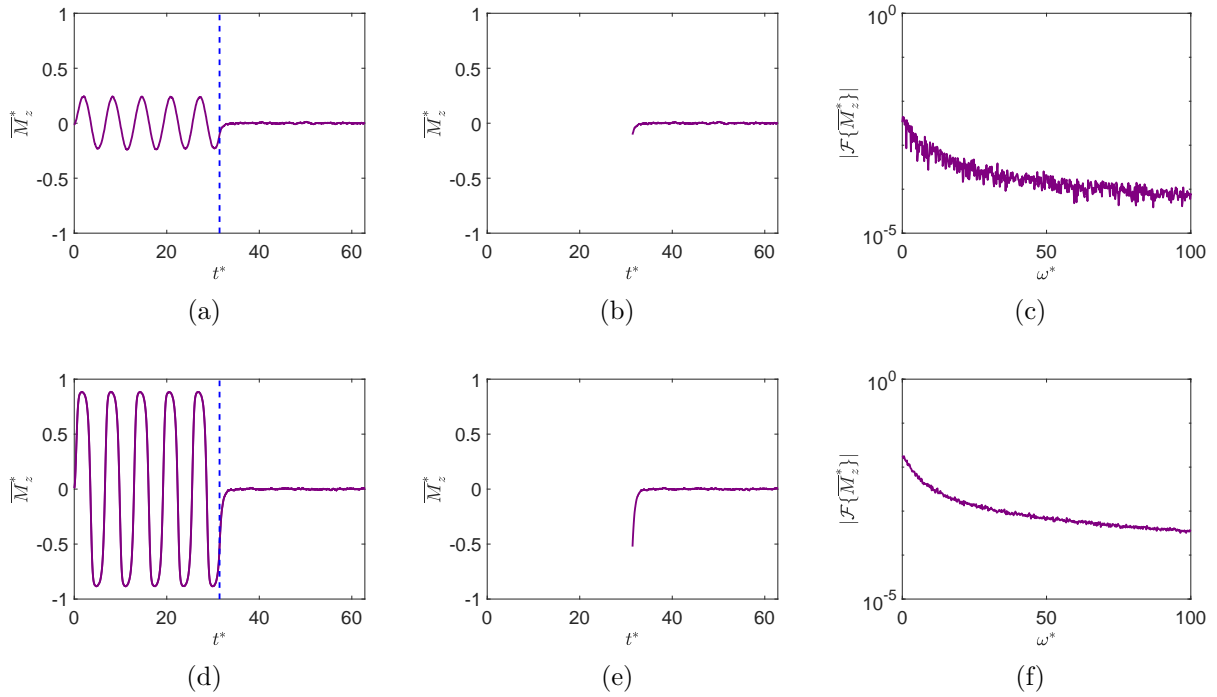
Figure 4.4 – Magnetization relaxation for $\phi = 1\%$, $\omega_H^* = 10$, $\lambda = 1$, Pe $= 6$. (a), (b) and (c): $\alpha = 1$. (d), (e) and (f): $\alpha = 10$. (a) and (d): Dimensionless time response (in purple) and the cut section used to isolate the relaxation time response (in blue). (b) and (e): Signal after the cut-off (windowed time response), representing the magnetization under relaxation. (c) and (f): Absolute value of the Fourier transform of the windowed signal in logarithm scale.

In Fig. 4.4(a), for a low value of α, the amplitude of the time response before the cut-off is low. After the cut (Fig. 4.4(b)), the Fourier transform in Fig. 4.4(c) shows a noisy spectra, due to the low value of α and α being defined as the ratio between the magnetic energy and brownian energy. Hence, with a low value of α, the brownian effect dominates the system. The maximum value of the spectra at 4.4(c) is observed at $\omega^* = 0$.

In Fig. 4.4(d), for a high value of α ($\alpha = 10$), the time response has a higher amplitude than before. After the cut (Fig. 4.4(e)), the Fourier transform in Fig. 4.4(f) shows a more smooth spectra - due to the higher value of Pe, the random contribution of the system decreased. Again, a peak is noted at $\omega^* = 0$. The variation of the Langevin parameter has not changed the system's dynamical aspects.

4.2 Parametric Analysis

A parametric analysis for each dimensionless parameter (Pe, ϕ, α, λ and ω_H^*) is now performed. For each case the system's mean magnetization response, the hysteresis curve, the phase space and the Poincaré map are obtained.

4.2.1 Péclet Number Scan

Figure 4.5 displays the results, in steady-state regime, scanning the variable Pe, varied from Pe = 1 to Pe = 10, whereas the other parameters have the values of $\alpha = 1$, $\omega_H^* = 1$, $\lambda = 1$ and $\phi = 1\%$. As the volume fraction is low ($\phi = 1\%$), periodic magnetic torques are not activated.
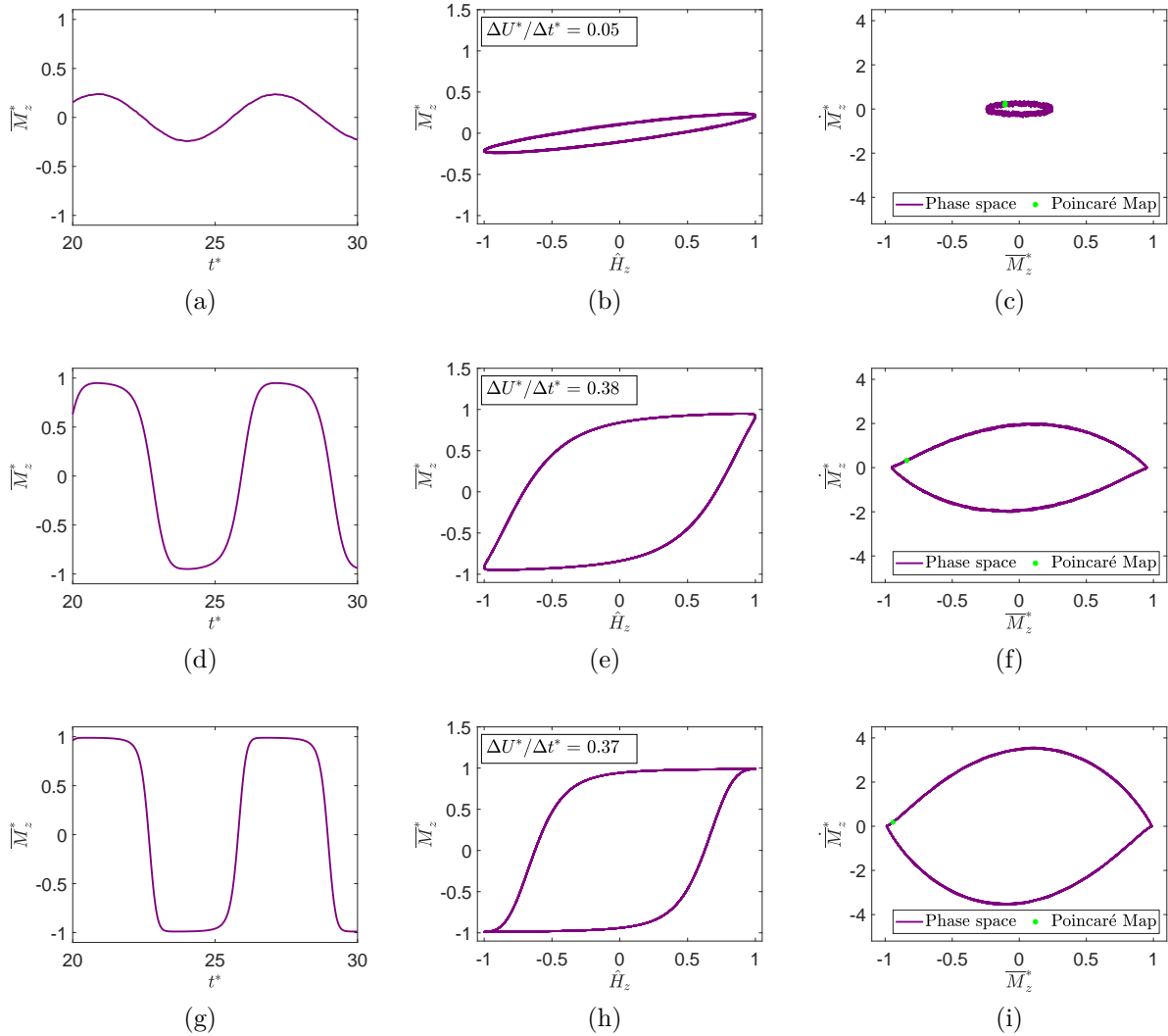
Figure 4.5 – Scan of the Péclet number (Pe) with $\alpha = 1$, $\omega_H^* = 1$, $\lambda = 1$ and $\phi = 1\%$. (a), (b) and (c): Pe = 1. (d), (e) and (f): Pe = 5. (g), (h) and (i): Pe = 10. (a), (d) and (g): Dimensionless magnetization's time response. (b), (e) and (h): Hysteresis curve and dimensionless rate of internal energy dissipation (upper left corner). (c), (f) and (i): Phase space (in purple) with Poincaré map (in green).

The first line of Fig. 4.5 shows the results of Pe = 1, the second line shows the results of Pe = 5 and the third line shows the results of Pe = 10. The first column of 4.5 displays the time response of the dimensionless magnetization, the second column displays the hysteresis curve of that simulation, as well as the dimensionless average rate of internal

energy dissipation (numerical value in the upper left corner), and the third column shows the phase space of that simulation (in purple) and the Poincaré map (in green).

The first simulation is displayed in Fig. 4.5 (a) to (c). The time response at (a) is a well-behaved sine with low amplitude, the hysteresis curve at (b) yields a small value of internal energy ($\Delta U^*/\Delta t^* = 0.05$) and the phase space at (c) outputs a Poincaré map periodic with period 1, as there is a single green point in the map, but with a significant random effect, showed by the random form of the phase space.

The second simulation, shown by Fig. 4.5 (d) to (f), for a medium value of Péclet number (Pe = 5), shows that increasing the Péclet number yields better results. The time response at (d) has a higher amplitude than (a). The hysteresis curve at (e) produces more internal energy ($\Delta U^*/\Delta t^* = 0.38$) than (b). However, the phase space at (f) still yields a periodic behavior with period 1, the same as (c).

The third simulation, shown by Fig. 4.5 (g) to (i), for a high value of Péclet number (Pe = 10), shows that increasing the Péclet number even further does not yield better results. The time response at (g) approximates a square wave. This happens because the maximum value of the magnetization (the saturation magnetization) is reached, in a way that $\overline{M}_z^*$ can not be higher than 1. The hysteresis curve at (h) produces slightly less internal energy ($\Delta U^*/\Delta t^* = 0.37$) than (e) and one can see at (h) the presence of sharp points. The phase space at (i) still yields a periodic response with period 1, the same as (c) and (i). Thus, the best case scenario for $\Delta U^*/\Delta t^*$ is reached between Pe = 1 and Pe = 10.

The graph of $\Delta U^*/\Delta t^*$ versus Pe is shown by the purple dots in Fig. 4.6. The highest value of $\Delta U^*/\Delta t^*$ is achieved by Pe = 6 (drawn attention to by the red dashed line). Thus, the value Pe = 6 is chosen for the next simulation, being the best case for the internal energy dissipation. Due to the saturation magnetization, $\Delta U^*/\Delta t^*$ can not grow indefinitely with Pe. One can deduce a power law dependence for the behavior of the graph such that

$$\frac{\Delta U^*}{\Delta t^*} = -0.3762 \, \text{Pe}^{-1.086} + 0.4214, \tag{4.4}$$

displayed by the purple line in Fig. 4.6.
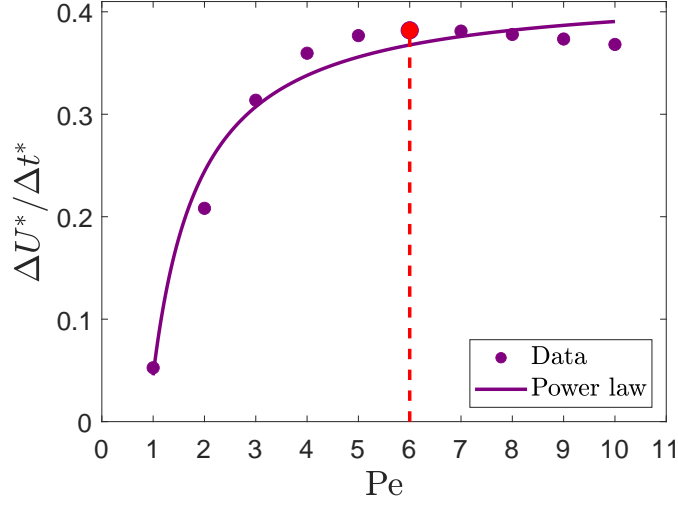
Figure 4.6 – Dimensionless average rate of internal energy versus the Péclet number (purple dots) and power law fit (purple line) for $\alpha = 1$, $\omega_H^* = 1$, $\lambda = 1$ and $\phi = 1\%$. The best case scenario is highlighted by the red line (Pe = 6).

4.2.2 Volume Fraction Scan

Results of high (15%) and low (1%) volume fraction are shown in this section. It is important to mention that a volume fraction of 15% is high in terms of biocompatibility, which is essential for FF, however, all this range is analyzed in order to have a global overview of the system dynamic behavior. For $\phi = 15\%$, the condition of periodic magnetic torques is activated in simulations, for faster convergence. For $\phi = 1\%$, the method of periodic magnetic torques is deactivated. Figure 4.7 shows the results, in the steady-state regime, for $\phi = 1\%$ and $\phi = 15\%$ with the parameters values Pe = 1, $\alpha = 1$, $\lambda = 1$, $\omega_H^* = 1$.
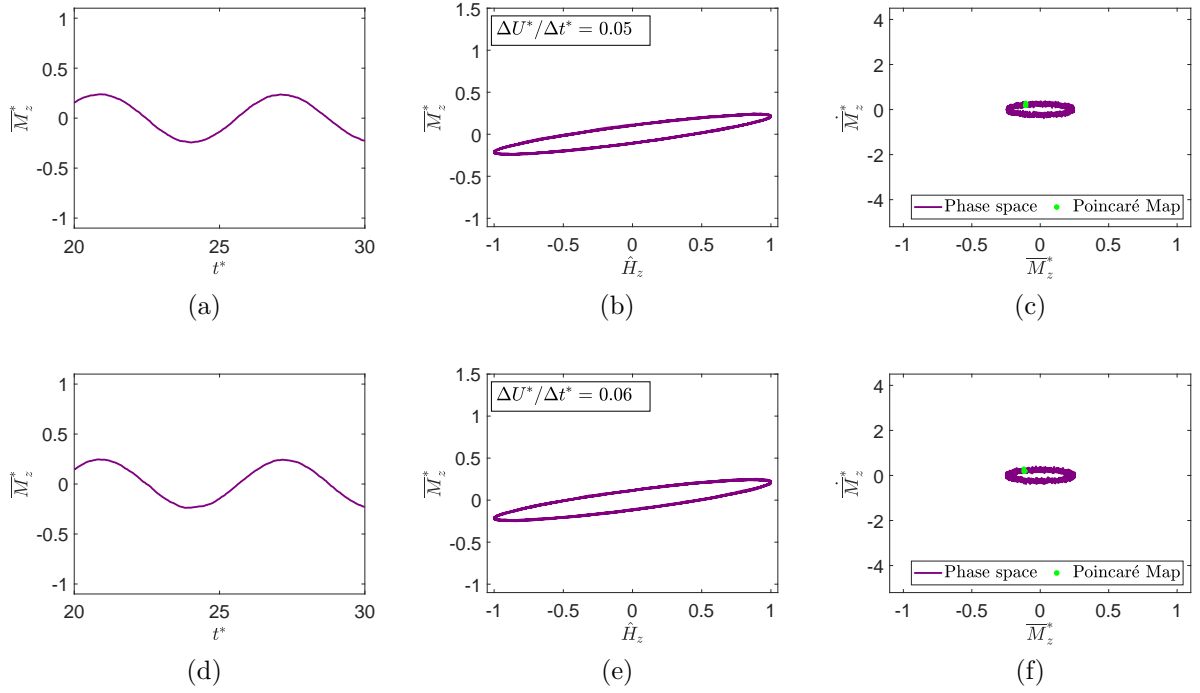
Figure 4.7 – Scan of the volume fraction parameter (ϕ) with Pe $= 1$, $\alpha = 1$, $\omega_H^* = 1$ and $\lambda = 1$. (a), (b) and (c): $\phi = 1\%$. (d), (e) and (f): $\phi = 15\%$. (a) and (d): Dimensionless magnetization's time response. (b) and (e): Hysteresis curve and dimensionless average rate of internal energy (upper left corner). (c) and (f): Phase space (in purple) with Poincaré map (in green).

In Fig. 4.7, it is observed that the variation of ϕ from 1% to 15% did not change the results significantly. The time response in Fig. 4.7 (a) and (d) remains the same. The hysteresis curve at 4.7 (b) and (e) shows a slight difference between the internal energy (from $\Delta U^*/\Delta t^* = 0.05$ to $\Delta U^*/\Delta t^* = 0.06$) and the Poincaré map at 4.7 (c) and (f) does not change.

The same simulation from Fig. 4.7 is repeated at 4.8, but with the values of Pe $= 10$ instead of Pe $= 1$.
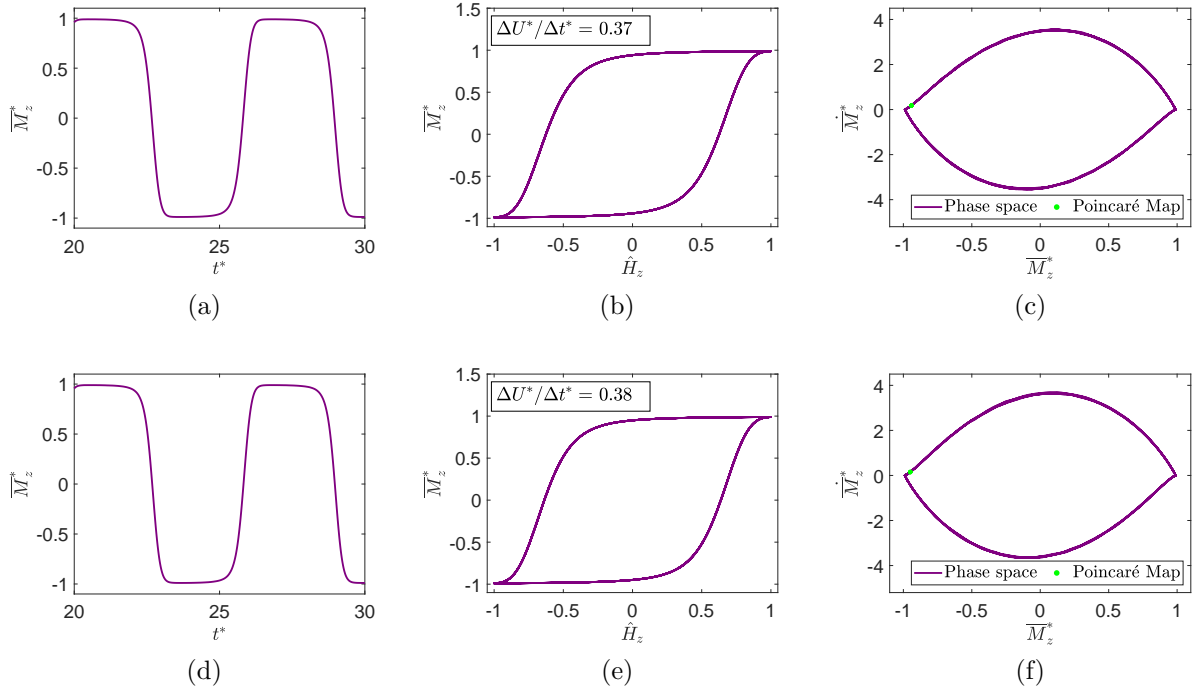
Figure 4.8 – Scan of the volume fraction parameter (ϕ) with Pe $= 10$, $\alpha = 1$, $\omega_H^* = 1$ and $\lambda = 1$. (a), (b) and (c): $\phi = 1\%$. (d), (e) and (f): $\phi = 15\%$. (a) and (d): Dimensionless magnetization's time response. (b) and (e): Hysteresis curve and dimensionless average rate of internal energy (upper left corner). (c) and (f): Phase space (in purple) with Poincaré map (in green).

Once again, at 4.8, the variation of ϕ from 1% to 15% did not changed the results. Due to cheaper and faster computation time, the value $\phi = 1\%$ is chosen in the next simulations.

4.2.3 Langevin Parameter Scan

Figure 4.9 displays the results, in steady-state regime, regarding the scan of the variable α from $\alpha = 1$ to $\alpha = 10$, for the constant values of Pe $= 6$, $\omega_H^* = 1$, $\lambda = 1$ and $\phi = 1\%$.
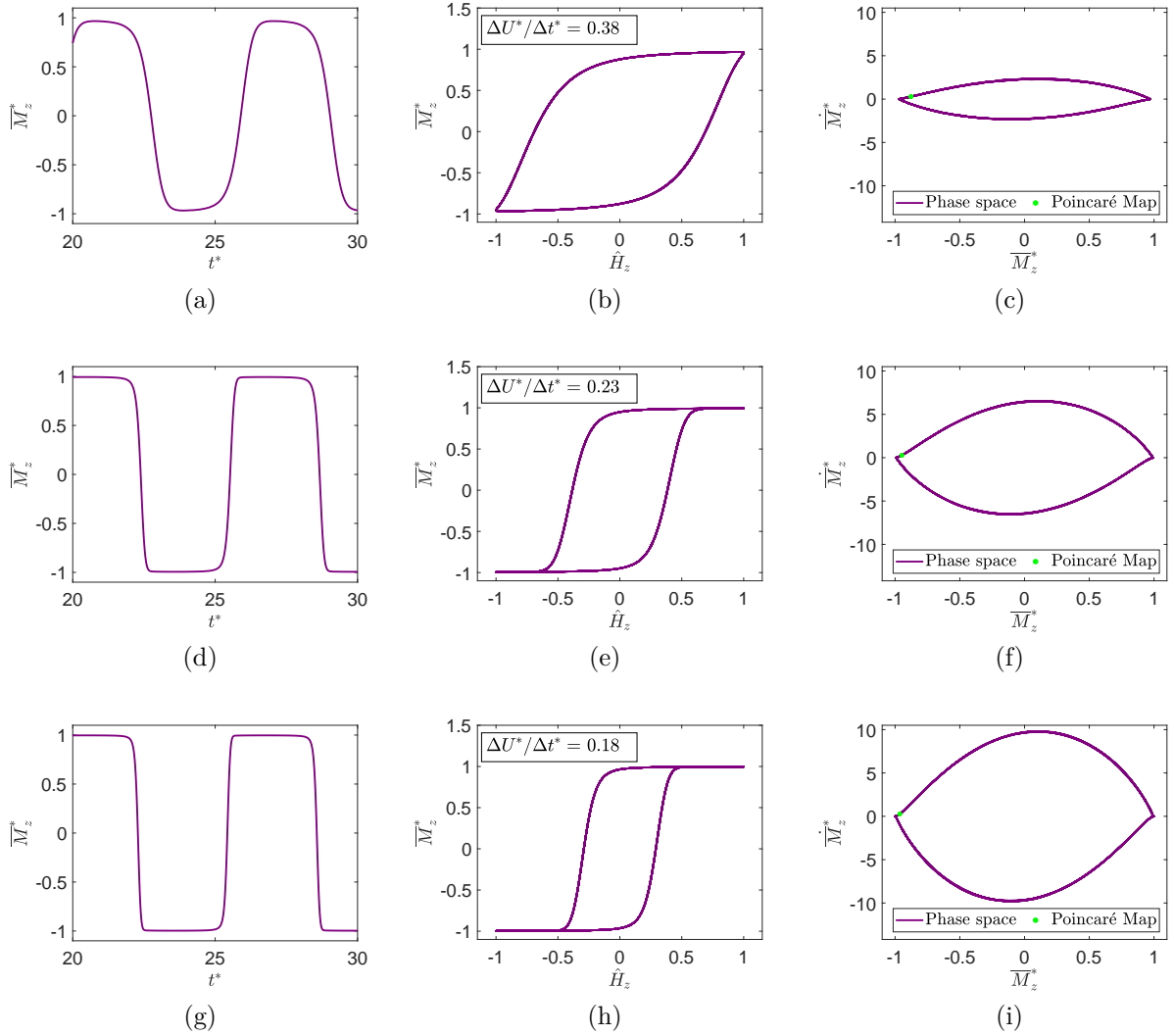
Figure 4.9 – Scan of the Langevin parameter (α) with Pe = 6, $\omega_H^* = 1$, $\lambda = 1$ and $\phi = 1\%$. (a), (b) and (c): $\alpha = 1$. (d), (e) and (f): $\alpha = 5$. (g), (h) and (i): $\alpha = 10$. (a), (d) and (g): Dimensionless magnetization's time response. (b), (e) and (h): Hysteresis curve and dimensionless average rate of internal energy (upper left corner). (c), (f) and (i): Phase space (in purple) with Poincaré map (in green).

The first simulation ($\alpha = 1$), shown by Fig. 4.9 (a) to (c), indicates a periodic behavior of the average magnetization with a value of internal energy dissipation of $\Delta U^*/\Delta t^* = 0.38$, as show by Fig. 4.9 (b). However, for the second simulation ($\alpha = 5$), shown by Fig. 4.9 (d) to (f), a lower value of internal energy dissipation is recorded ($\Delta U^*/\Delta t^* = 0.23$) in Fig. 4.9 (e). This happens due to the saturation magnetization, represented by the sharp edges of the hysterysis curve, which decreases the area under the curve of $\overline{M}_z^*$ and $\hat{H}_z$. The third simulation ($\alpha = 10$), shown by Fig. 4.9 (g) to (i), yields an even lower value of internal energy dissipation in Fig. 4.9 (h), as the saturation magnetization is reached in a faster way. Besides, at 4.9 (g), the time response approximates even further to a square wave, due to the higher intensity of the dipole-field interaction.

The graph of $\Delta U^*/\Delta t^*$ versus α is shown by the purple dots in Fig. 4.10. The maximum value is achieved by the value $\alpha = 1$. For higher values of α, the saturation magnetization is reached. It is expected that the higher the value of α, the effect of the magnetic field into the system is increased, which could benefit the value of $\Delta U^*/\Delta t^*$ for different values of parameters. Because of this, the value $\alpha = 10$ is chosen as the best case and used in the next simulations. One can deduce a power law dependence for the behavior of the graph, such that

$$\frac{\Delta U^*}{\Delta t^*} = 0.8101\alpha^{-0.1285} - 0.4273, \tag{4.5}$$

displayed by the purple line in Fig. 4.10.
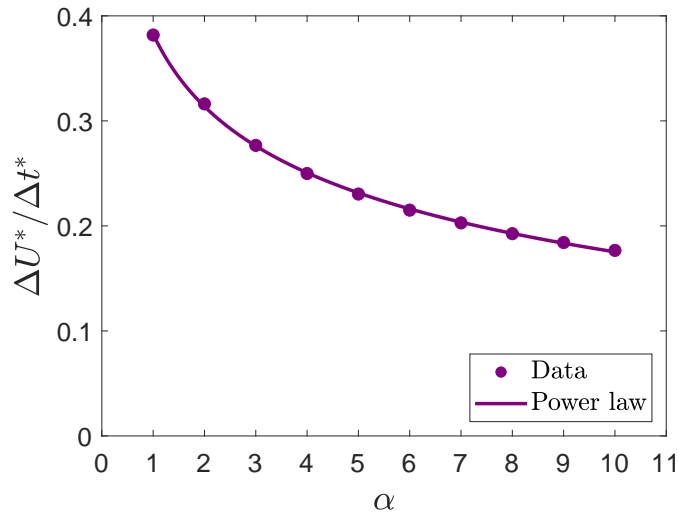
Figure 4.10 – Dimensionless average rate of internal energy versus the Langevin parameter (purple dots) and power law fit (purple line) for $\mathrm{Pe} = 6$, $\omega_H^* = 1$, $\lambda = 1$ and $\phi = 1\%$. The best case scenario is chosen by $\alpha = 10$.

4.2.4   Dipole Interaction Parameter Scan

Figure 4.9 displays the results, in steady-state regime, regarding the scan of the variable λ from $\lambda = 1$ to $\lambda = 10$, whereas the other parameters have the values of $\mathrm{Pe} = 6$, $\alpha = 10$, $\omega_H^* = 1$ and $\phi = 1\%$. For this simulation, the periodic magnetic torque condition is applied.
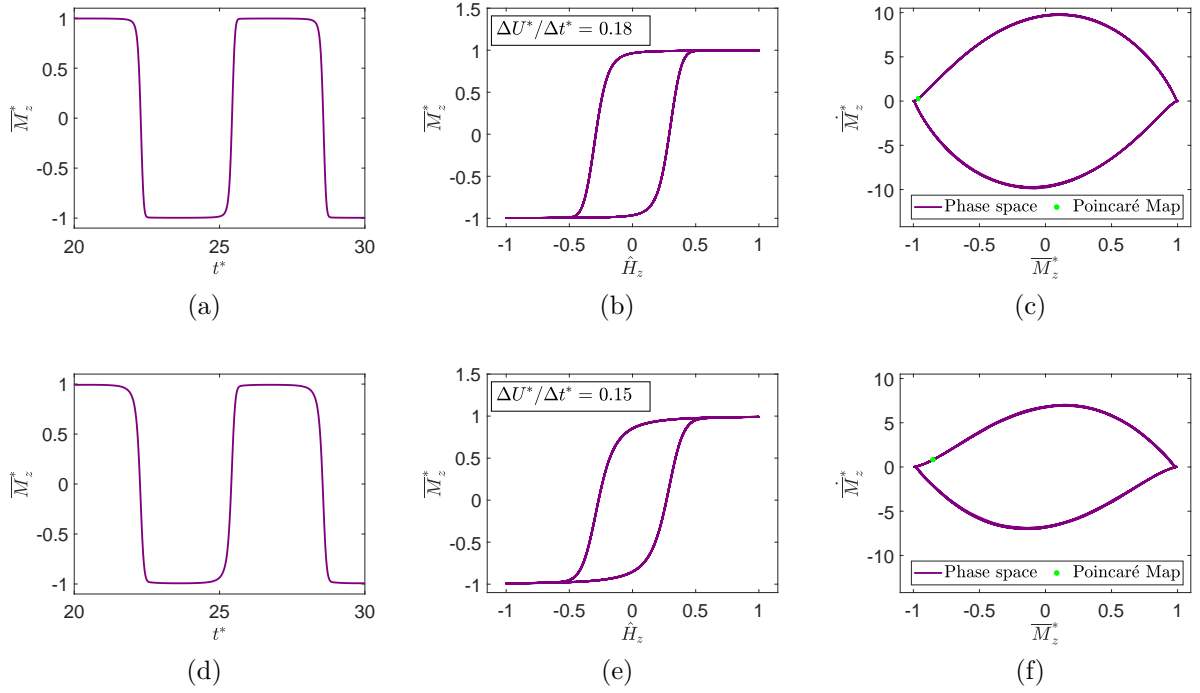
Figure 4.11 – Scan of the dipole interaction parameter (λ) with Pe = 6, $\alpha = 10$, $\omega_H^* = 1$ and $\phi = 1\%$. (a), (b) and (c): $\lambda = 1$. (d), (e) and (f): $\lambda = 10$. (a) and (d): Dimensionless magnetization's time response. (b) and (e): Hysteresis curve and dimensionless average rate of internal energy (upper left corner). (c) and (f): Phase space (in purple) with Poincaré map (in green).

The first simulation ($\lambda = 1$), shown by Fig. 4.11 (a) to (c), indicates a square wave (periodic with period-1) with internal energy dissipation of $\Delta U^*/\Delta t^* = 0.18$ for the value of $\lambda = 1$. However, for the second simulation ($\lambda = 10$), shown by Fig. 4.11 (d) to (f), a lower internal energy dissipation is obtained, $\Delta U^*/\Delta t^* = 0.15$, in Fig. 4.11 (e), as the condition of saturation magnetization is reached rapidly.

The graph of $\Delta U^*/\Delta t^*$ versus λ is shown by the purple dots in Fig. 4.12. The decreasing behavior of $\Delta U^*/\Delta t^*$ is due to the saturation magnetization, which is reached faster for higher λ. The maximum value of the internal energy dissipation is reached in $\lambda = 1$, which is chosen as the best case for the next simulations. One can deduce a power law dependence for the behavior of the graph, such that

$$\frac{\Delta U^*}{\Delta t^*} = -0.007296\lambda^{0.6488} + 0.1844, \tag{4.6}$$

displayed by the purple line in Fig. 4.12.
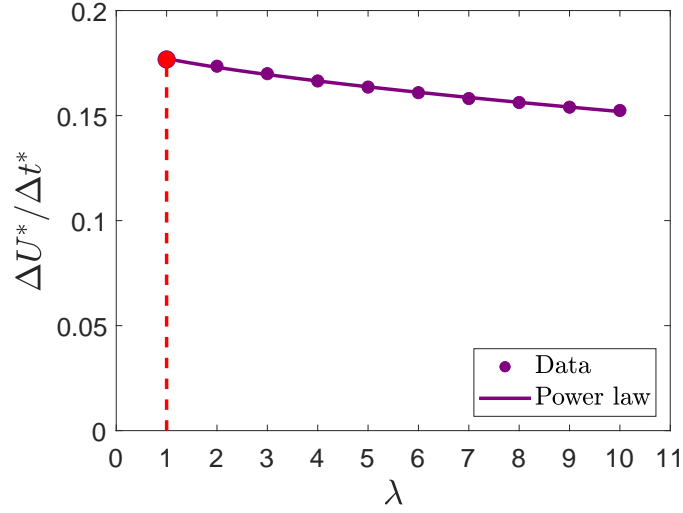
Figure 4.12 – Dimensionless average rate of internal energy versus the dipole interaction parameter (purple dots) and power law fit (purple line) for Pe = 6, $\alpha = 10$, $\omega_H^* = 1$ and $\phi = 1\%$. The best case scenario is highlighted by the red line ($\lambda = 1$).

4.2.5   Magnetic Field's Angular Frequency Scan

Figure 4.13 shows the results, in steady-state regime, of the scan of the variable ω_H^* from $\omega_H^* = 1$ to $\omega_H^* = 10$, with the values Pe = 6, $\alpha = 10$, $\lambda = 1$ and $\phi = 1\%$.
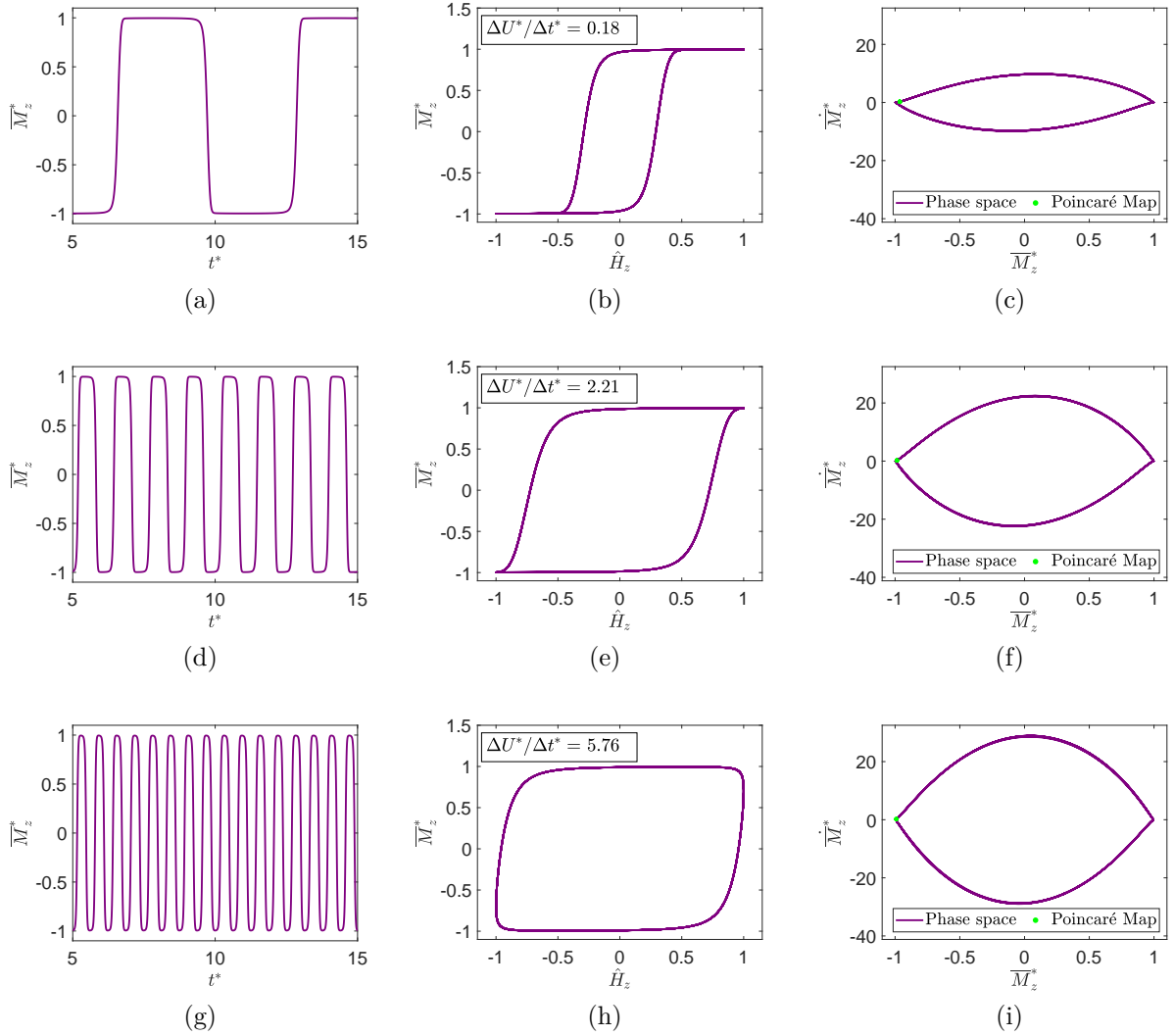
Figure 4.13 – Scan of the magnetic field's angular frequency (ω_H^*) with Pe = 6, $\alpha = 10$, $\lambda^* = 1$ and $\phi = 1\%$. (a), (b) and (c): $\omega_H^* = 1$. (d), (e) and (f): $\omega_H^* = 5$. (g), (h) and (i): $\omega_H^* = 10$. (a), (d) and (g): Dimensionless magnetization's time response. (b), (e) and (h): Hysteresis curve and dimensionless average rate of internal energy (upper left corner). (c), (f) and (i): Phase space (in purple) with Poincaré map (in green).

The first simulation in Fig. 4.13(a) to (c) shows the results of $\omega_H^* = 1$, which indicates a response with the saturation magnetization. The second simulation in Fig. 4.13(d) to (f) for $\omega_H^* = 5$ indicates that the increase of the frequency made the magnetization approximate to a sine wave instead of the square wave, as the response remains in the saturation magnetization (given by $\overline{M}_z^* = 1$ or $\overline{M}_z^* = -1$) for a shorter period of time. The third simulation in Fig. 4.13(g) to (i) for $\omega_H^* = 10$ shows that, for an ever higher frequency, the saturation magnetization is not reached, which increases the area of the hysteresis curve. The internal energy dissipation achieves a maximum value of $\Delta U^*/\Delta t^* = 5.76$ for $\omega_H^* = 10$. One can conclude that reaching the saturation magnetization is not desirable for MH.

The calculation of $\Delta U^*/\Delta t^*$ accounts the area produced by the hysteresis curve and the time of the simulation. Because of this, high values of $\Delta U^*/\Delta t^*$ indicate that or the system produced a high area in the hysteresis curve or that the system produced such area in a short period of time. The value $\Delta U^*/\Delta t^* = 5.76$ obtained for $\omega_H^* = 10$ is greater than twice the value of $\Delta U^*/\Delta t^* = 2.21$ obtained for $\omega_H^* = 5$, not because the area of the hysteresis curve doubled, but because the system completed the area in a faster way for $\omega_H^* = 10$ than $\omega_H^* = 5$.

The graph of $\Delta U^*/\Delta t^*$ versus ω_H^* is shown by the purple dots in Fig. 4.14. The graph is peaked at value $\omega_H^* = 10$ (red dot). Thus, the value $\omega_H^* = 10$ is the best analyzed case and is used for the next simulations. One can deduce a power law dependence for the behavior of the graph, such that

$$\frac{\Delta U^*}{\Delta t^*} = 0.2816\omega_H^{*\,1.326} - 0.1522, \tag{4.7}$$

displayed by the purple line in Fig. 4.14.
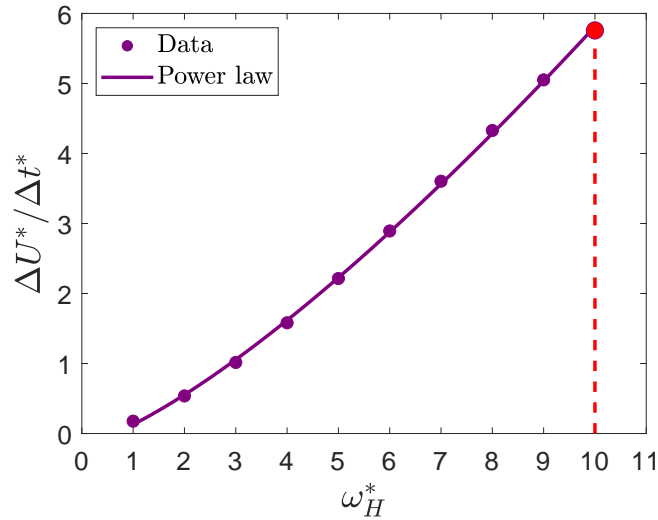
Figure 4.14 – Dimensionless average rate of internal energy versus the external magnetic field's dimensionless angular frequency (purple dots) and power law fit (purple line) for Pe = 6, $\alpha = 10$, $\lambda = 1$ and $\phi = 1\%$. The best case scenario is highlighted by the red line ($\omega_H^* = 10$).

Hence, the values at Table 1 correspond to the best scenario considering all values of analyzed parameters.

Pe	ϕ	α	λ	ω_H^*
6	1%	10	1	10

Table 1 – Values chosen for the maximum value of $\Delta U^*/\Delta t^*$ in alternating magnetic field.

Comparing the graphs of $\Delta U^*/\Delta t^*$ in Figs. 4.6, 4.10, 4.12 and 4.14, the variable ω_H^* has produced the highest rate of change on $\Delta U^*/\Delta t^*$. Thus, ω_H^* is the parameter

that has the greatest influence for the system's dissipation of internal energy with a pure alternating magnetic field.

4.3   Bifurcation Diagram

Fig. 4.15 displays the results of the ω_H^* sweep for $\alpha = 10$, $\lambda = 1$, Pe = 6 and $\phi = 1\%$. Fig. 4.15(a) shows the bifurcation diagram of $\overline{M}_z^*$ using ω_H^* as the control parameter. The sweep begins at $\omega_H^* = 1$, it waits until the system reaches steady-state condition and then it passes to the next step of the frequency, for example $\omega_H^* = 1.1$. The process is repeated until the frequency $\omega_H^* = 10$ is reached. On the bifurcation diagram, some values of frequencies are highlighted by colors (green, cyan, red and pink) and their respective phase space and Poincaré map are shown at each corner of the Fig. 4.15(a). The green dot represents the Poicaré map at frequency $\omega_H^* = 5.96$, the cyan dots the Poincaré map of $\omega_H^* = 7.43$, the red dot the Poincaré map of $\omega_H^* = 8.35$ and the pink dots the Poincaré map of $\omega_H^* = 9.27$. Fig. 4.15(b) shows the internal energy dissipation generated at each step of ω_H^* during the sweep (blue curve) and the internal energy dissipation calculated in isolated simulations (the same graph of Fig. 4.14).
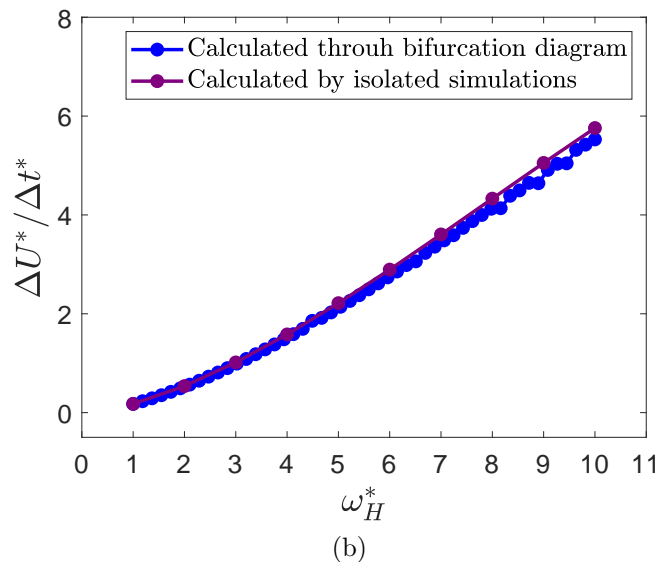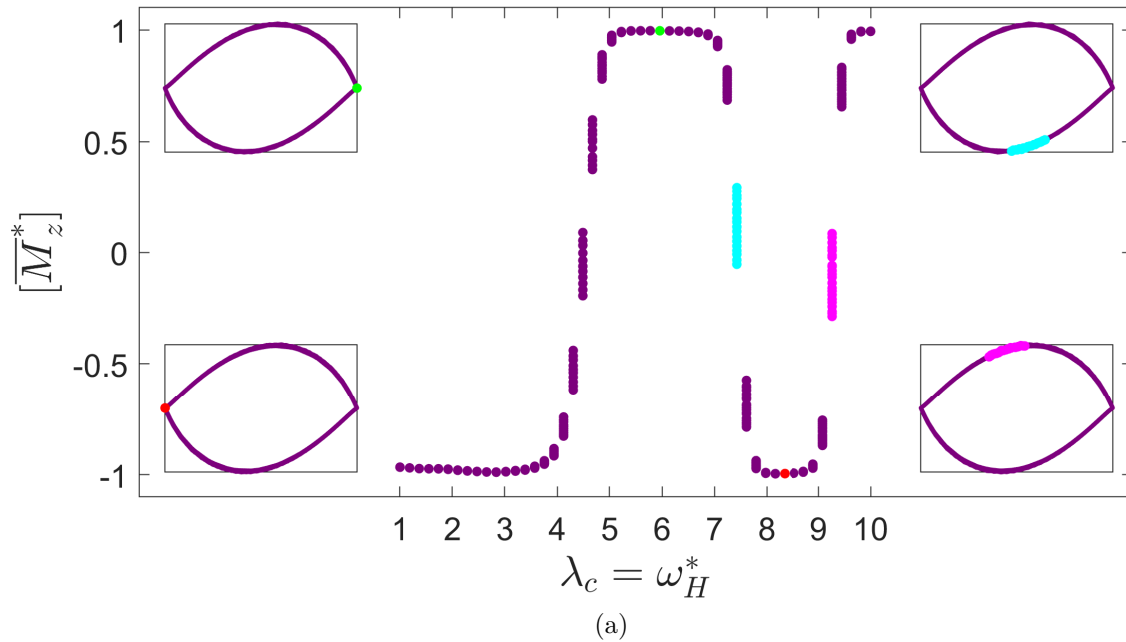
Figure 4.15 – Results of the magnetic field's angular frequency sweep in steady-state for $\alpha = 10$, $\lambda = 1$, Pe = 6 and $\phi = 1\%$. (a) Bifurcation diagram (on the center) with phase space and Poincaré map of 4 arbitraly chosen points shown at each corner. (b) Average internal energy dissipation for each point of the bifurcation diagram (in blue) and average internal energy dissipation in isolated simulations (in purple).

In Fig. 4.15(a), the bifurcation diagram begins with a periodic response with period 1 and the Poincaré map is at the right side of the phase space (green dot). Then, the number of points increases and the Poincaré map is at the lower side of the phase space (cyan dots). This fast transition of the number of points happens due to the high velocity coupled with the random contribution of system. Next, Poincaré map shows a single point once again and Poincaré map is located at the left side of the phase space (red dot). Then,

the number of points in the Poincaré map increases again and the Poincaré map is located at the upper side of the phase space (pink dots). Seeing the phase space of the selected points (green, cyan, red and pink) at each corner, one can conclude that the behavior of the system remains the same (the shape of the phase space does not change whatsoever) and the Poincaré map changes in the clockwise direction along the phase space. Thus, the changes of the number of points in the Poincaré map are due to the frequency sweep and not due to a drastically change of behavior from the system. Hence, there are no qualitative changes and no threshold values in the bifurcation diagram of Fig. 4.15(a).

In Fig. 4.15(b), the curve of $\Delta U^*/\Delta t^*$ during the frequency sweep (blue) and the one obtained in isolated simulations (purple) are very close. Although the initial point for both curves in $\omega_H^* = 1$ is exactly the same, as both have the same initial condition, the blue curve tends separate from the purple curve, due to the nonlinearities of the system.

5 Results of Alternating Magnetic Field with Shear Motion

"Do not be afraid to make mistakes. A mistake for a chess player is fatal; for a mathematician it is par for the course. What you should be terrified of is a blank sheet in front of you after having thought about a problem for a little while."

Béla Bollobás

In this chapter, it is analyzed the system's behavior under an oscillatory shear motion and an one-dimensional alternating magnetic field. Hence, let $\dot{\gamma}$ be the shear rate under the system, such that

$$\dot{\gamma}^*(t^*) = \dot{\gamma}_0^* \sin(\omega_S^* t^*), \tag{5.1}$$

in which $\dot{\gamma}_0^*$ is the shear rate dimensionless magnitude and ω_S^* is the dimensionless angular frequency associated with the dimensionless shear rate. The magnetic field behavior is the same from the previous chapter,

$$\hat{\mathbf{H}}(t^*) = \sin(\omega_H^* t^*)\hat{\mathbf{z}}. \tag{5.2}$$

Although the system is under shear movement, the magnetic field is still one-dimensional and periodic, the same behavior from Chapter 4: Results of Alternating Magnetic Field. Hence, the expression used in this chapter for the dimensionless average dissipation of internal energy is the same from Chapter 4,

$$\frac{\Delta U^*}{\Delta t^*} = \frac{1}{t_f^*} \left[\int_{\overline{M}_z^*(0),\hat{H}_z(0)}^{\overline{M}_z^*\left(t_f^*\right),\hat{H}_z\left(t_f^*\right)} \hat{H}_z \, \mathrm{d}\overline{M}_z^* \right], \tag{5.3}$$

that is, $\dfrac{\Delta U^*}{\Delta t^*}$ is calculated by the area of the hysteresis curve only in the $\hat{\mathbf{z}}$ direction. The contribution of the $\hat{\mathbf{y}}$ direction is zero, as $\hat{H}_y$ is zero and the area of $\hat{H}_y$ and $\overline{M}_y^*$ is zero,

even though $\overline{M}_y^*$ is not zero under shear movement. Thus, in this chapter, the dissipation of internal energy is calculated by the area of the hysteresis curve only in the $\hat{\mathbf{z}}$ direction.

Fig. 5.1 shows the system treated in this chapter. Besides the oscillatory magnetic field in the $\hat{\mathbf{z}}$ direction, an sinusoidal shear rate is applied in the $\hat{\mathbf{y}}$ direction.
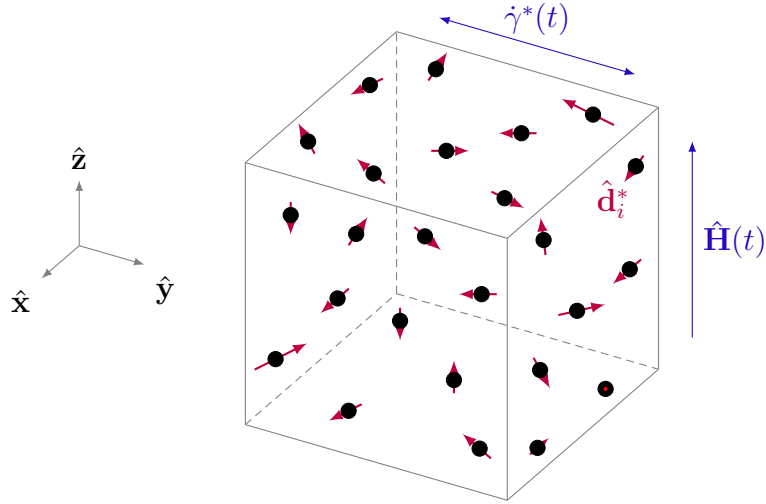
Figure 5.1 – Representation of the system analyzed in this chapter. A dimensionless shear rate motion with harmonic behavior is applied in the $\hat{\mathbf{y}}$ direction ($\dot{\gamma}^*$) and a magnetic field in the $\hat{\mathbf{z}}$ direction ($\hat{\mathbf{H}}$). Particles are represented by black dots and their dipole vector in red ($\hat{\mathbf{d}}_i$).

5.1   Parametric Analysis

A parametric analysis for $\dot{\gamma}_0^*$ and ω_S^* is performed to identify the parameters that most influences the system dynamics. For each case the system's hysteresis curve, average magnetization response in $\hat{\mathbf{z}}$ (purple graphs) and $\hat{\mathbf{y}}$ (black graphs) directions, the Fourier transform in logarithm scale of the time responses, the phase space, the Poincaré map are presented.

5.1.1   Highest Average Rate of Internal Energy Dissipation

5.1.1.1   Shear Rate's Angular Frequency Scan

Figures 5.2 and 5.3 shows the results, in steady-state regime, for ω_S^* varying from 1 to 10, with the parameters values of Pe $= 6$, $\alpha = 10$, $\omega_H^* = 10$, $\lambda = 1$, $\phi = 1\%$ and $\dot{\gamma}_0^* = 1$.

Figure 5.2 – Scan of the shear rate's angular frequency (ω_S^*) with Pe = 6, $\alpha = 10$, $\omega_H^* = 10$, $\lambda = 1$, $\phi = 1\%$ and $\dot{\gamma}_0^* = 1$. (a), (b) and (c): $\omega_S^* = 1$. (d), (e) and (f): $\omega_S^* = 5$. (g), (h) and (i): $\omega_S^* = 10$. (a), (d) and (g): Time response in $\hat{\mathbf{z}}$ direction. (b), (e) and (h): Hysteresis curve and dimensionless average rate of internal energy (upper left corner). (c), (f) and (i): Phase space in $\hat{\mathbf{z}}$ direction (in purple) with Poincaré map (in green).

In Fig. 5.2, one can be observe that the variation of ω_S^* does not change the behavior of the system in the $\hat{\mathbf{z}}$ direction. The time response, the value of $\Delta U^*/\Delta t^*$, the phase space and the Poincaré map remain the same. This happens because the value of α and Pe are too high, making the magnetic field dominant in the system response. As the Langevin parameter (α) is defined as the ration between magnetic energy and brownian energy, for a high value of $\alpha = 10$, the magnetic field predominates in the system. At the same time, once the Péclet number (Pe) is defined as the ratio between the brownian diffusion time and the convection time of the particle, for a high value of Pe = 6, the convection time prevails in the system, disturbing the relaxation time of the particles.

On the other hand, in Fig. 5.3, it is notable the changes of the system in the

$\hat{\mathbf{y}}$ direction. In Figs. 5.3(a), (d) and (g), as ω_S^* increases, the amplitude from the time response decreases. This happens because the system has less time to respond to the shear rate excitation with a higher frequency ω_S^*. From the phase spaces at Figs. 5.3(b), (e) and (h), the Poincaré map begins with a periodic response with period 5 with $\omega_S^* = 1$ and then transforms into a periodic response with period 1 for $\omega_S^* = 5$ and $\omega_S^* = 10$. Lastly, Figs. 5.3(c), (f) and (i) show the Fourier transform in logarithm scale of the time response in steady-state of the $\hat{\mathbf{z}}$ direction (in purple) and $\hat{\mathbf{y}}$ direction (in black). In all of the Fourier spectra, the peak at frequency $\omega^* = 10$ is notable in the purple curve, once it is the frequency of the magnetic field, $\omega_H^* = 10$, applied at the $\hat{\mathbf{z}}$ direction. At Figs. 5.3(c), with $\omega_S^* = 1$, one may expect a peak in $\omega^* = 1$, however, due to the noisy spectra, it is not notable. Two peaks are observed, at $\omega^* \approx 9$ and $\omega^* \approx 11$. At Figs. 5.3(f), with $\omega_S^* = 5$, a peak of the black curve is notable at $\omega^* = 5$ and $\omega^* = 15$, due to nonlinearities. At Figs. 5.3(i), with $\omega_S^* = 10$, a peak of the black curve is seen at $\omega^* = 10$.

Figure 5.3 – Scan of the shear rate's angular frequency (ω_S^*) with Pe = 6, $\alpha = 10$, $\omega_H^* = 10$, $\lambda = 1$, $\phi = 1\%$ and $\dot{\gamma}_0^* = 1$. (a), (b) and (c): $\omega_S^* = 1$. (d), (e) and (f): $\omega_S^* = 5$. (g), (h) and (i): $\omega_S^* = 10$. (a), (d) and (g): Time response in $\hat{\mathbf{y}}$ direction. (b), (e) and (h): Phase space in $\hat{\mathbf{y}}$ direction (in black) with Poincaré map (in green). (c), (f) and (i): Fourier transform in logarithm scale of the steady-state time response in $\hat{\mathbf{z}}$ direction (in purple) and in $\hat{\mathbf{y}}$ direction (in black).

The graph of $\Delta U^*/\Delta t^*$ versus ω_S^* is shown by the purple curve in Fig. 5.4. The shear's frequency is indifferent for the dissipation of internal energy considering the adopted parameters in the analysis.
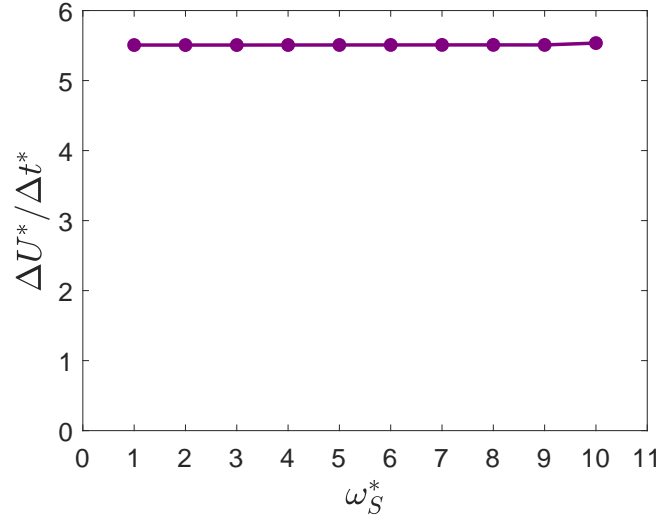
Figure 5.4 – Dimensionless average rate of internal energy versus the shear rate's dimensionless angular frequency (in purple) with alternating magnetic field for Pe $= 6$, $\alpha = 10$, $\omega_H^* = 10$, $\lambda = 1$, $\phi = 1\%$ and $\dot{\gamma}_0^* = 1$.

5.1.1.2 Shear Rate's Amplitude Scan

Figures 5.5 and 5.6 show the results, in steady-state regime, for $\dot{\gamma}_0$ varying from 1 to 10, with the other parameters values of Pe $= 6$, $\alpha = 10$, $\omega_H^* = 10$, $\lambda = 1$, $\phi = 1\%$ and $\omega_S^* = 10$.

Figure 5.5 – Scan of the shear rate's amplitude ($\dot{\gamma}_0^*$) with Pe = 6, $\alpha = 10$, $\omega_H^* = 10$, $\lambda = 1$, $\phi = 1\%$ and $\omega_S^* = 10$. (a), (b) and (c): $\dot{\gamma}_0^* = 1$. (d), (e) and (f): $\dot{\gamma}_0^* = 5$. (g), (h) and (i): $\dot{\gamma}_0^* = 10$. (a), (d) and (g): Time response in $\hat{\mathbf{z}}$ direction. (b), (e) and (h): Hysteresis curve and dimensionless average rate of internal energy (upper left corner). (c), (f) and (i): Phase space in $\hat{\mathbf{z}}$ direction (in purple) with Poincaré map (in green).

Once again, in Fig. 5.5, the variation of $\dot{\gamma}_0^*$ did not change the behavior of the system in the $\hat{\mathbf{z}}$ direction. The time response, the value of $\Delta U^*/\Delta t^*$, the phase space and the Poincaré map remain the same. This happens because the high values of α and Pe leads to the predominance of the magnetic field. Hence, the shear rate's amplitude is indifferent for the system in the $\hat{\mathbf{z}}$ direction and in the value of $\Delta U^*/\Delta t^*$ as well.

In Fig. 5.6, one can observe that the shear influences system response in $\hat{\mathbf{y}}$ direction. Figs. 5.6(a), (d) and (g), shows that with the increase of $\dot{\gamma}_0^*$, the time response amplitude at $\hat{\mathbf{y}}$ direction also increases. Due to the higher value of $\dot{\gamma}_0^*$, the MNPs line in the $\hat{\mathbf{y}}$ direction and increase the value of the magnetization in this direction. The same behavior can be seen at the phase space, in Figs. 5.6(b), (e) and (h), where the amplitude of the phase

space increases in the $\hat{\mathbf{y}}$ direction. The Poincaré map, however, shows a periodic response with period 1 in all values of $\dot{\gamma}_0^*$, indicating that the time response maintains its periodic behavior. Lastly, the Fourier transform in Figs. 5.6(c), (f) and (i) indicates the frequency $\omega^* = 10$ at the $\hat{\mathbf{z}}$ direction, due to $\omega_H^* = 10$, and a small peak at $\omega^* = 10$ at the $\hat{\mathbf{y}}$ direction, due to $\omega_S^* = 10$. At higher values of $\dot{\gamma}_0$, the frequency $\omega^* = 0$ is reported again.
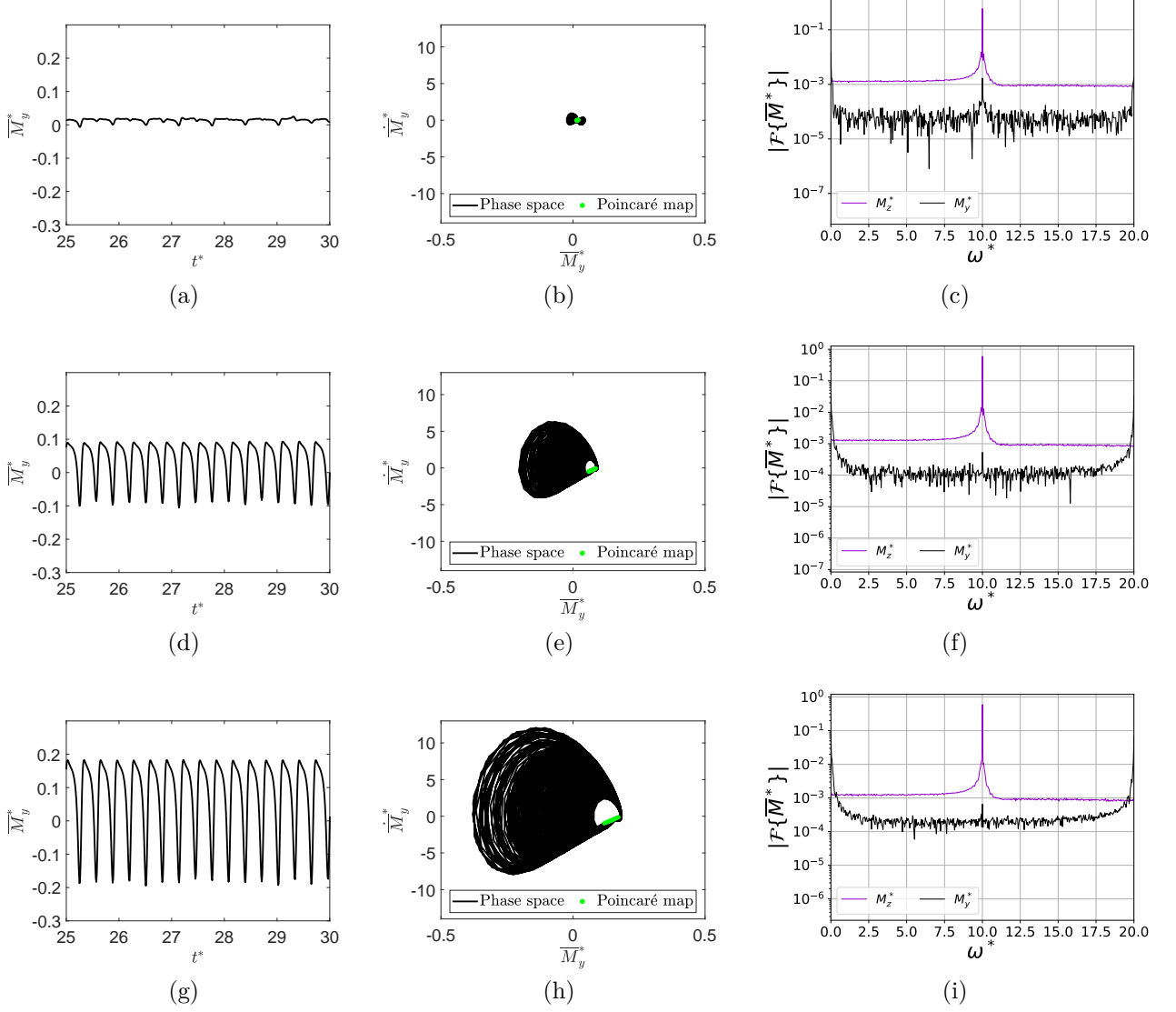
Figure 5.6 – Scan of the shear rate's amplitude ($\dot{\gamma}_0$) with Pe = 6, $\alpha = 10$, $\lambda = 1$, $\phi = 1\%$ and $\omega_S^* = 10$. (a), (b) and (c): $\dot{\gamma}_0^* = 1$. (d), (e) and (f): $\dot{\gamma}_0^* = 5$. (g), (h) and (i): $\dot{\gamma}_0^* = 10$. (a), (d) and (g): Time response in $\hat{\mathbf{y}}$ direction. (b), (e) and (h): Phase space in $\hat{\mathbf{y}}$ direction (in black) with Poincaré map (in green). (c), (f) and (i): Fourier transform in logarithm scale of the steady-state time response in $\hat{\mathbf{z}}$ direction (in purple) and in $\hat{\mathbf{y}}$ direction (in black).

The graph of $\Delta U^*/\Delta t^*$ versus $\dot{\gamma}_0^*$ is shown by the purple curve in Fig. 5.7. The shear's amplitude does not change the internal energy dissipation significantly.
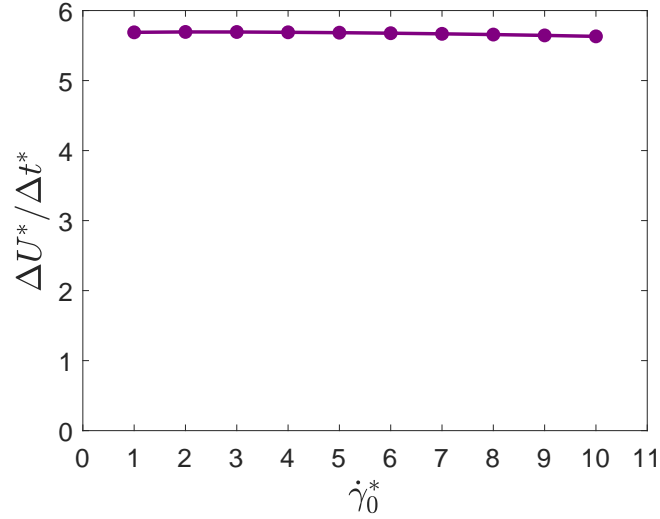
Figure 5.7 – Dimensionless average rate of internal energy versus the shear rate's dimensionless angular frequency (in purple) with alternating magnetic field for $Pe = 6$, $\alpha = 10$, $\omega_H^* = 10$, $\lambda = 1$, $\phi = 1\%$ and $\omega_S^* = 10$.

5.1.2 Low Langevin Parameter and Low Péclet Number

As previous results showed no variation for $\Delta U^*/\Delta t^*$, due to the high values of α and Pe, a scan for low values of α and Pe is now carried out.

5.1.2.1 Shear Rate's Angular Frequency Scan

Figures 5.8 and 5.9 shows the results, in steady-state regime, for ω_S^* varying from 1 to 10, with the other parameters values of $Pe = 1$, $\alpha = 1$, $\omega_H^* = 10$, $\lambda = 1$, $\phi = 1\%$ and $\dot{\gamma}_0^* = 10$.
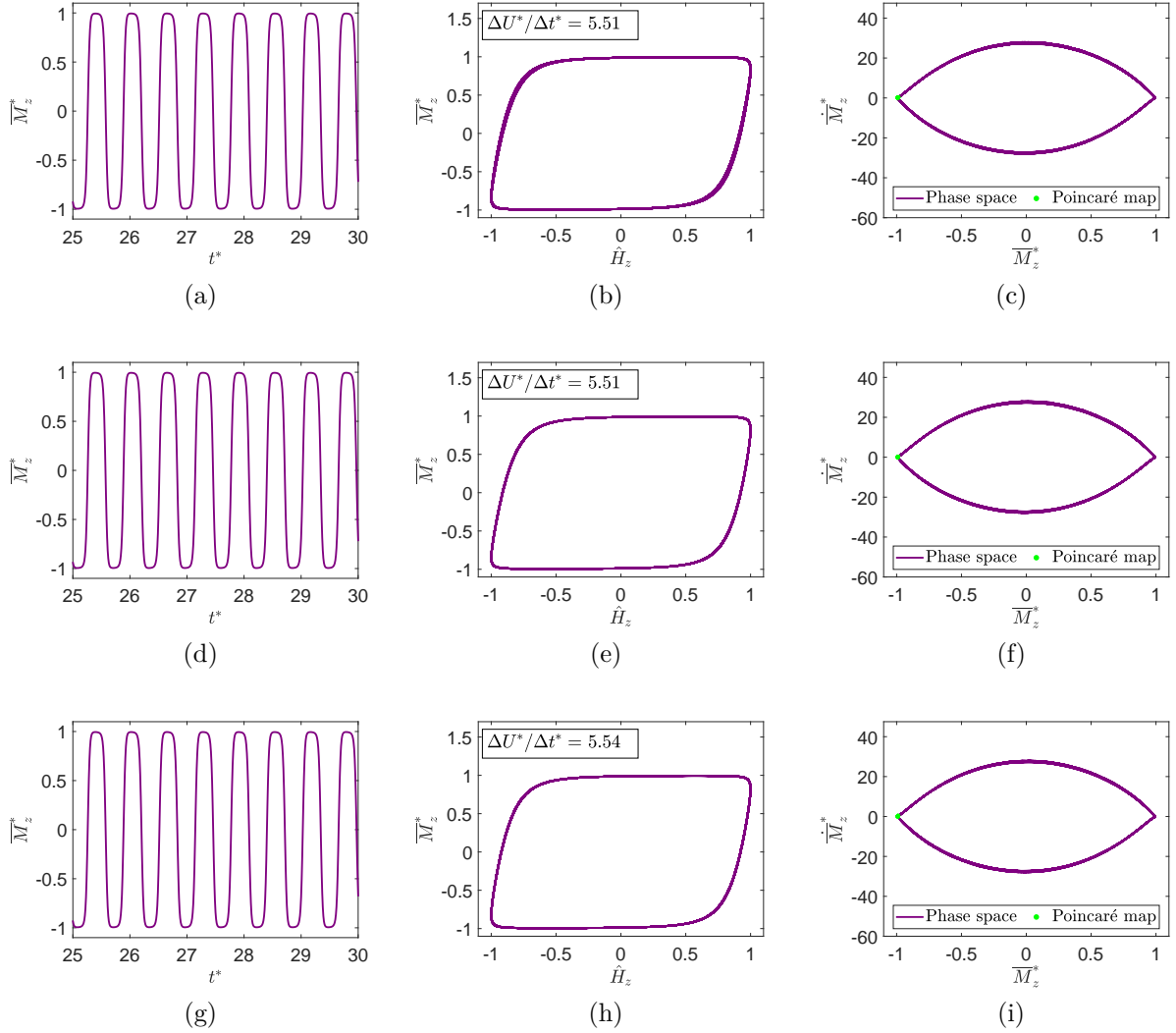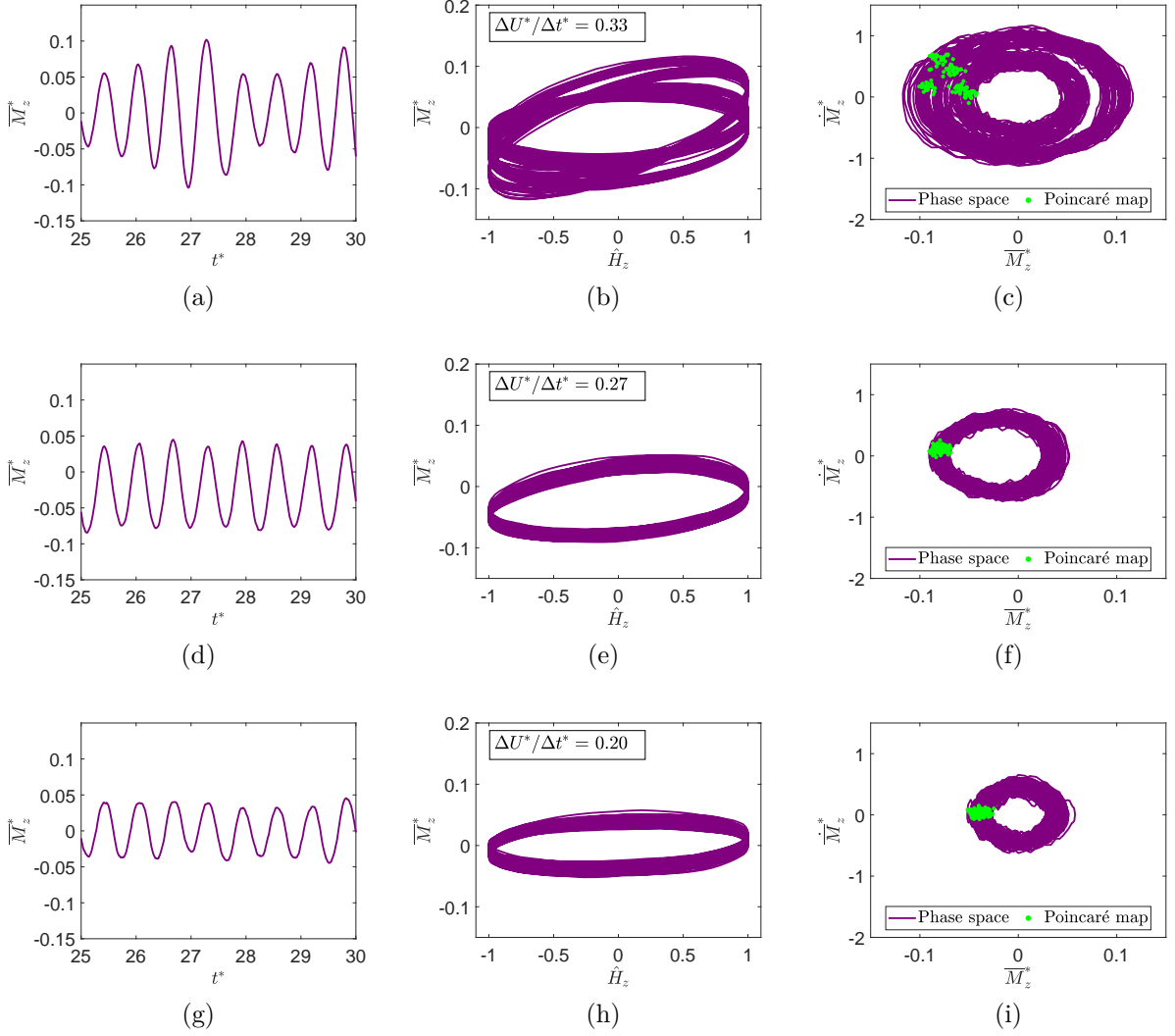
Figure 5.8 – Scan of the shear rate's angular frequency (ω_S^*) with Pe = 1, $\alpha = 1$, $\omega_H^* = 10$, $\lambda = 1$, $\phi = 1\%$ and $\dot{\gamma}_0^* = 10$. (a), (b) and (c): $\omega_S^* = 1$. (d), (e) and (f): $\omega_S^* = 5$. (g), (h) and (i): $\omega_S^* = 10$. (a), (d) and (g): Time response in $\hat{\mathbf{z}}$ direction. (b), (e) and (h): Hysteresis curve and dimensionless average rate of internal energy (upper left corner). (c), (f) and (i): Phase space in $\hat{\mathbf{z}}$ direction (in purple) with Poincaré map (in green).

In Fig. 5.8, due to the low value of Pe, the random effect in the system response is higher when compared with the previous analysis. This can be seen by the random phase space and the high noise intensity of the Poincaré map. We observe that as the value of ω_S^* increases, both the amplitude of $\overline{M}_z^*$ and the value $\Delta U^*/\Delta t^*$ decreases.

In Fig. 5.9, the amplitude of $\overline{M}_y^*$ decreases for higher values of ω_S^*. The Fourier spectrum in Fig. 5.9(c) shows the multiple frequencies of the excitation $\omega_H^* = 10$ and $\omega_S^* = 1$. The Fourier spectrum in Fig. 5.9(f) shows the frequencies $\omega_H^* = 10$ and $\omega_S^* = 5$ and Fig. 5.9(i) displays $\omega_H^* = 10$ and $\omega_S^* = 10$.
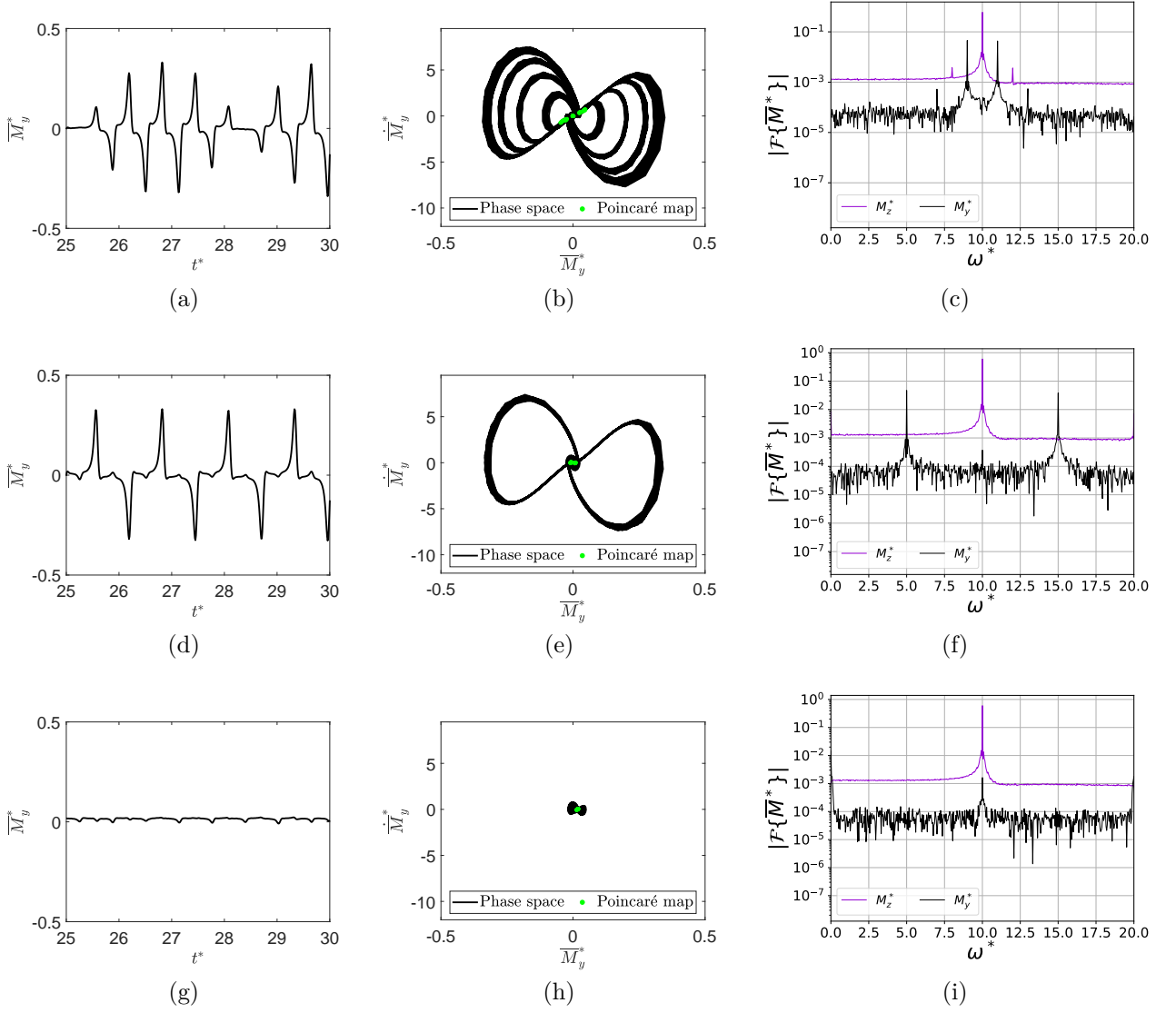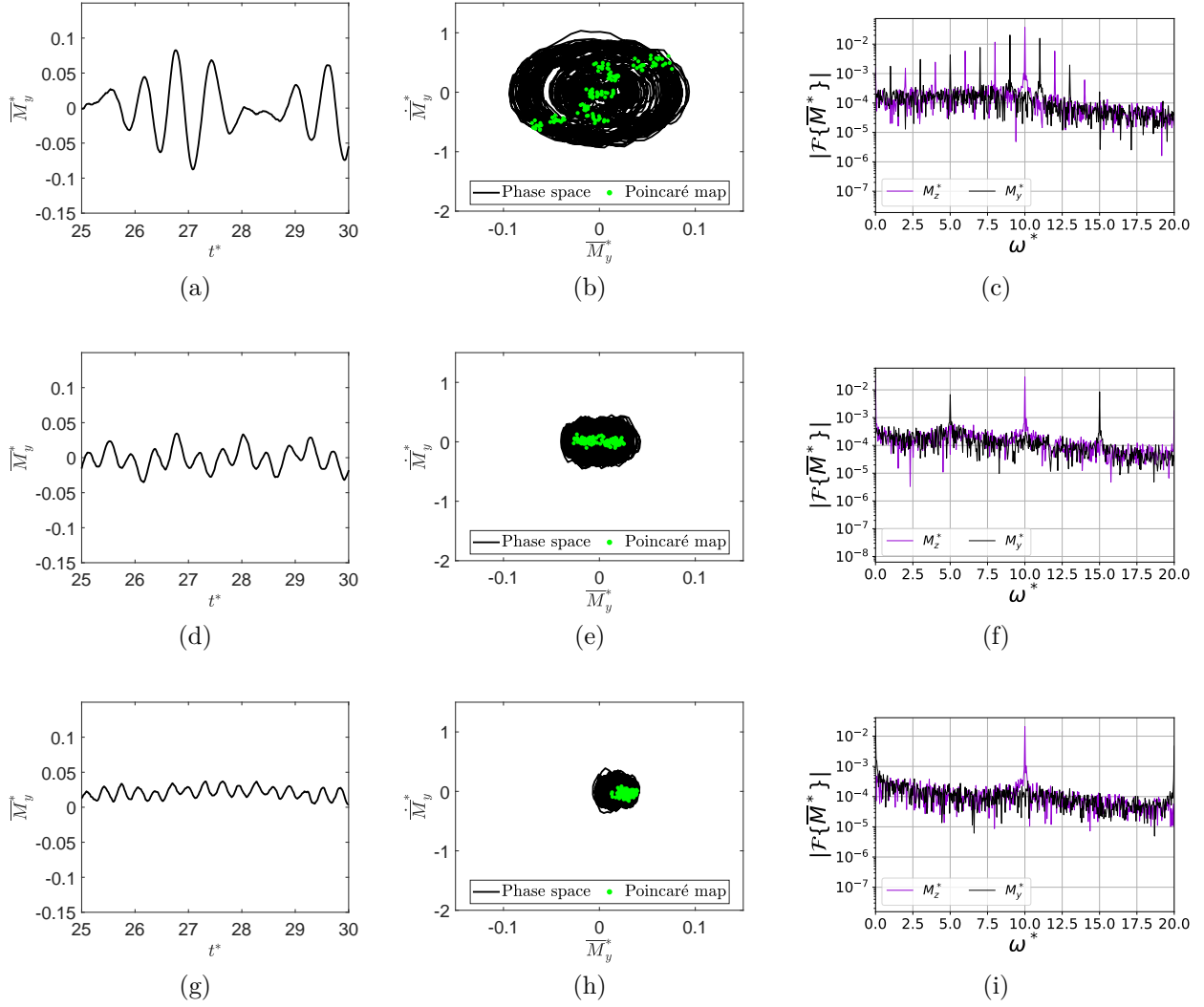
Figure 5.9 – Scan of the shear rate's angular frequency (ω_S^*) with Pe = 1, $\alpha = 1$, $\omega_H^* = 10$, $\lambda = 1$, $\phi = 1\%$ and $\dot{\gamma}_0^* = 1$. (a), (b) and (c): $\omega_H^* = 1$. (d), (e) and (f): $\omega_H^* = 5$. (g), (h) and (i): $\omega_H^* = 10$. (a), (d) and (g): Time response in $\hat{\mathbf{y}}$ direction. (b), (e) and (h): Phase space in $\hat{\mathbf{y}}$ direction (in black) with Poincaré map (in green). (c), (f) and (i): Fourier transform in logarithm scale of the steady-state time response in $\hat{\mathbf{z}}$ direction (in purple) and in $\hat{\mathbf{y}}$ direction (in black).

The graph of $\Delta U^*/\Delta t^*$ versus ω_S^* for low α and low Peis shown by the purple curve in Fig. 5.10, which reach its maximum value at $\omega_S^* = 1$ (red dot). The variation of the graph is due to the random effect into the system for low Pe.
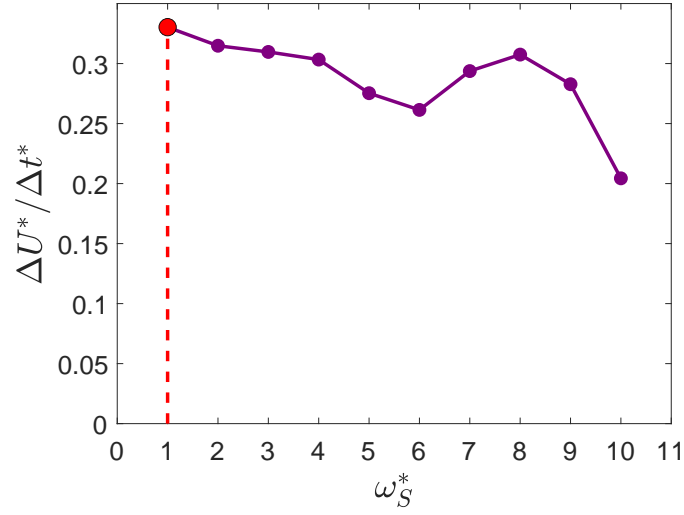
Figure 5.10 – Dimensionless average rate of internal energy versus the shear rate's dimensionless angular frequency (in purple) with alternating magnetic field for $Pe = 1$, $\alpha = 1$, $\omega_H^* = 10$, $\lambda = 1$, $\phi = 1\%$ and $\dot{\gamma}_0^* = 10$. The best case scenario is highlighted by the red line ($\omega_H^* = 10$).

5.1.2.2 Shear Rate's Amplitude Scan

Figures 5.5 and 5.6 show the results, in steady-state regime, for $\dot{\gamma}_0$ varying from 1 to 10, with the values of $Pe = 1$, $\alpha = 1$, $\omega_H^* = 10$, $\lambda = 1$, $\phi = 1\%$ and $\omega_S^* = 10$.
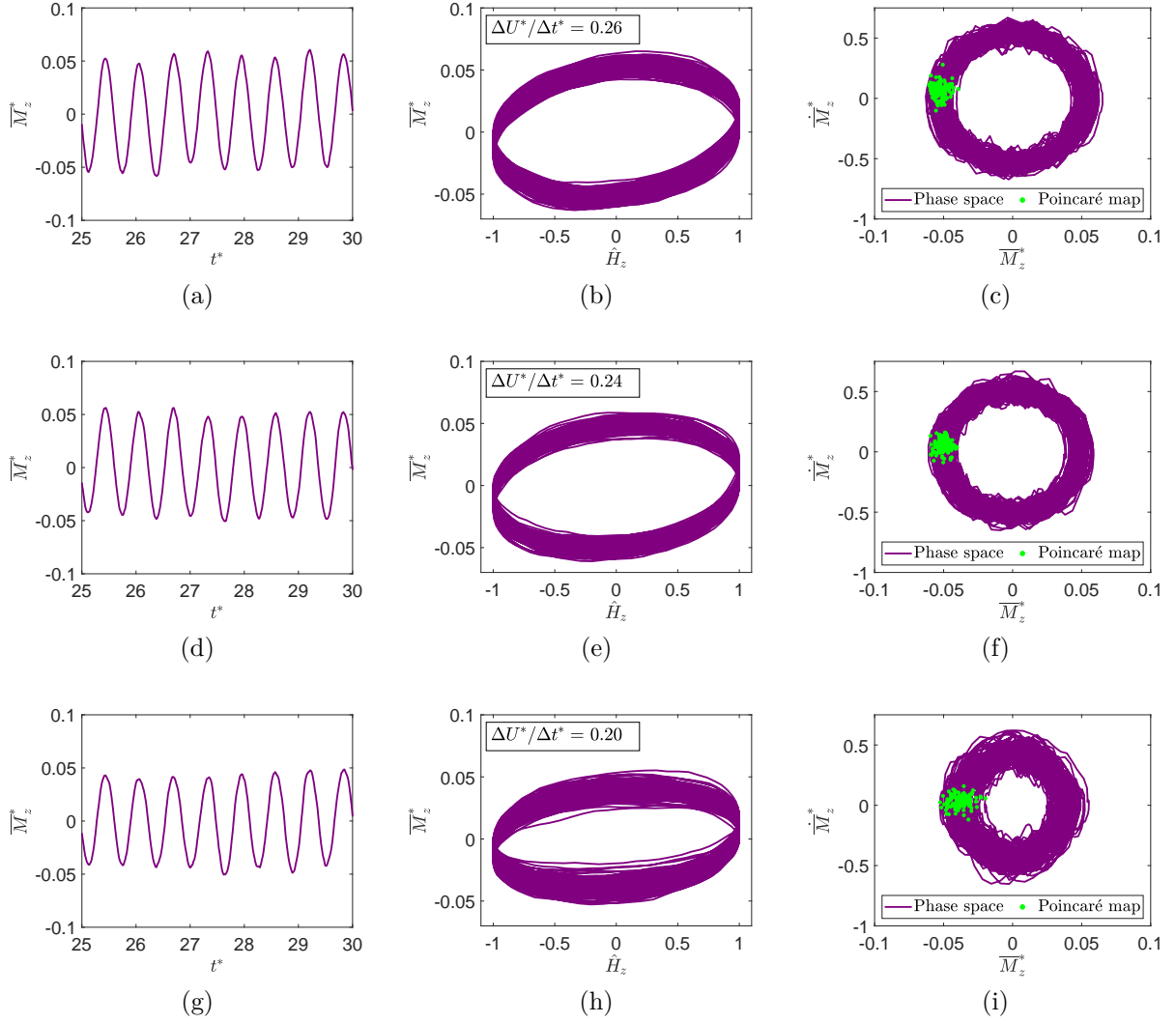
Figure 5.11 – Scan of the shear rate's amplitude ($\dot{\gamma}_0^*$) with Pe = 1, $\alpha = 1$, $\omega_H^* = 10$, $\lambda = 1$, $\phi = 1\%$ and $\omega_S^* = 10$. (a), (b) and (c): $\dot{\gamma}_0^* = 1$. (d), (e) and (f): $\dot{\gamma}_0^* = 5$. (g), (h) and (i): $\dot{\gamma}_0^* = 10$. (a), (d) and (g): Time response in $\hat{\mathbf{z}}$ direction. (b), (e) and (h): Hysteresis curve and dimensionless average rate of internal energy (upper left corner). (c), (f) and (i): Phase space in $\hat{\mathbf{z}}$ direction (in purple) with Poincaré map (in green).

In Fig. 5.11, all responses have the same behavior in the $\hat{\mathbf{z}}$ direction, but the amplitude decreases slightly for a higher $\dot{\gamma}_0^*$. The Poincaré maps show high deviation and presents a period-1 response. In Fig. 5.12(b), (e) and (h), the phase space in the $\hat{\mathbf{y}}$ direction shifts to the right side of the graph, because of the influence of the magnetic field.
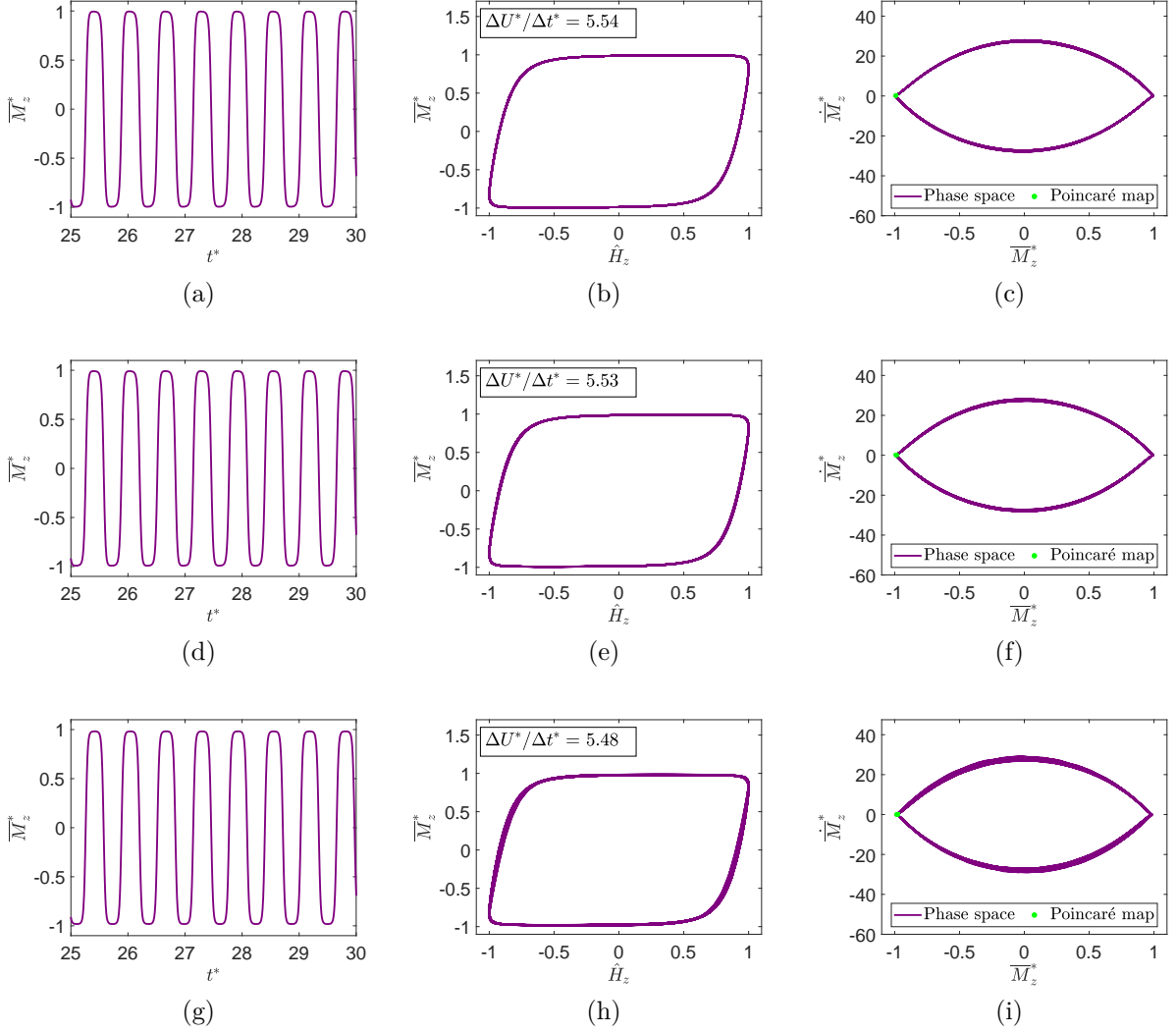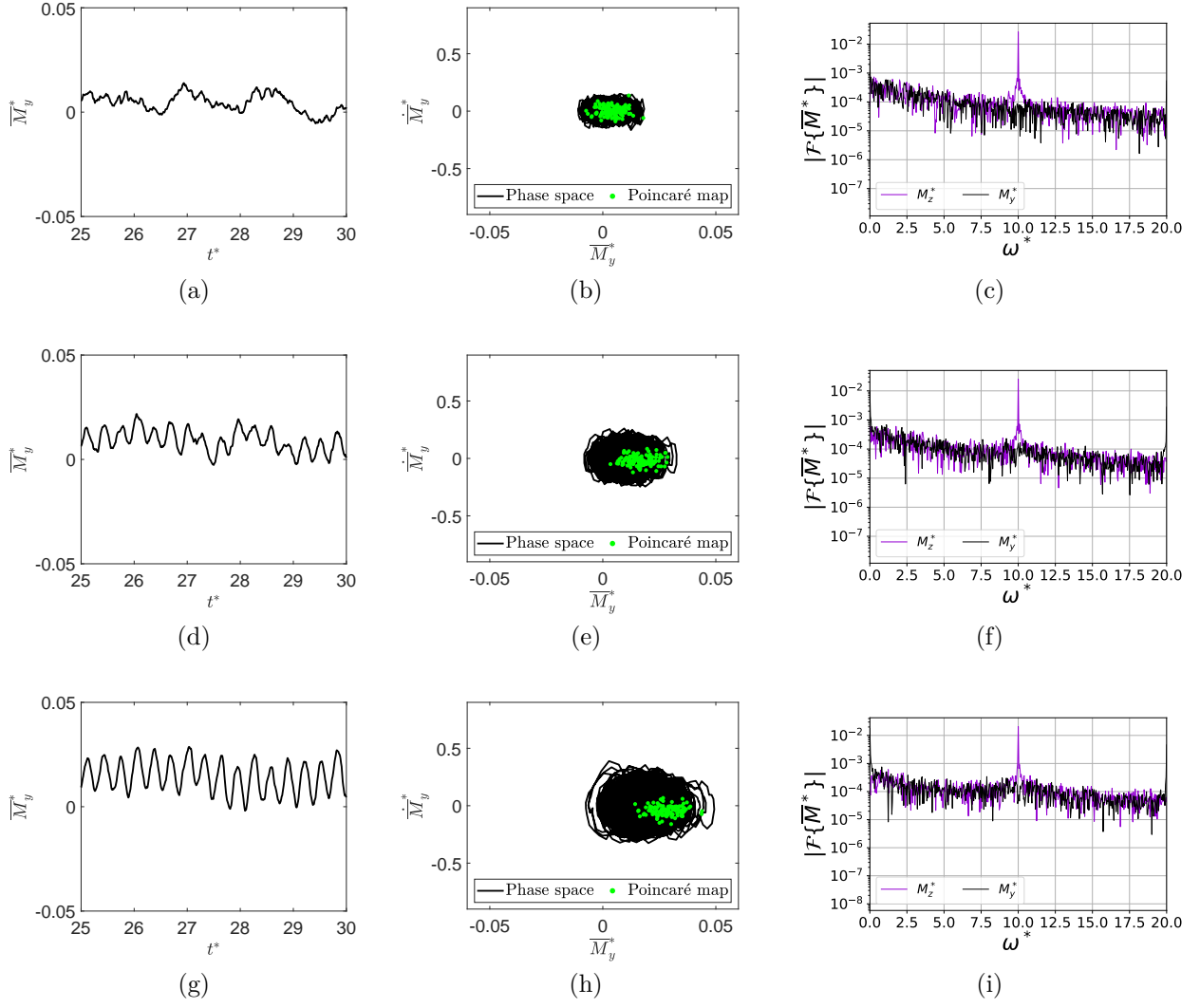
Figure 5.12 – Scan of the shear rate's amplitude ($\dot{\gamma}_0$) with Pe $= 1$, $\alpha = 1$, $\omega_H^* = 10$, $\lambda = 1$, $\phi = 1\%$ and $\omega_S^* = 10$. (a), (b) and (c): $\dot{\gamma}_0^* = 1$. (d), (e) and (f): $\dot{\gamma}_0^* = 5$. (g), (h) and (i): $\dot{\gamma}_0^* = 10$. (a), (d) and (g): Time response in $\hat{\mathbf{y}}$ direction. (b), (e) and (h): Phase space in $\hat{\mathbf{y}}$ direction (in black) with Poincaré map (in green). (c), (f) and (i): Fourier transform in logarithm scale of the steady-state time response in $\hat{\mathbf{z}}$ direction (in purple) and in $\hat{\mathbf{y}}$ direction (in black).

The graph of $\Delta U^*/\Delta t^*$ versus $\dot{\gamma}_0^*$ is shown by the purple curve in Fig. 5.7. The graph is peaked at value $\dot{\gamma}_0^* = 1$ (red dot). The value $\dot{\gamma}_0^* = 1$ presents the best case for the shear rate.
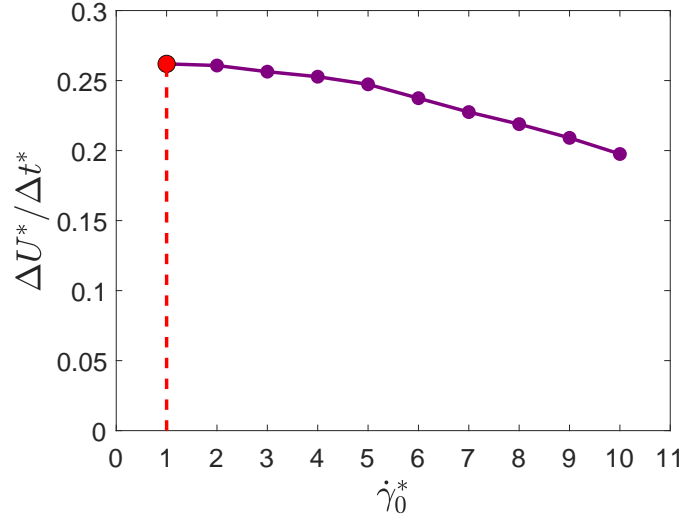
Figure 5.13 – Dimensionless average rate of internal energy versus the shear rate's dimensionless angular frequency (in purple) with alternating magnetic field for Pe = 1, $\alpha = 1$, $\omega_H^* = 10$, $\lambda = 1$, $\phi = 1\%$ and $\omega_S^* = 10$. The best case scenario is highlighted by the red line ($\dot{\gamma}_0^* = 1$).

The values of the best case scenario for the shear rate are presented at Table 2.

ω_S^*	$\dot{\gamma}_0^*$
1	1

Table 2 – Values chosen for the maximum value of $\Delta U^*/\Delta t^*$ in alternating magnetic field with shear motion.

Comparing the graphs of $\Delta U^*/\Delta t^*$ in Figs. 5.10 and 5.13, the variable ω_S^* has produced the highest rate of change on $\Delta U^*/\Delta t^*$. Thus, ω_S^* is the parameter that has the greatest influence for the system's dissipation of internal energy with an alternating magnetic field with shear motion. But analyzing the behavior of $\Delta U^*/\Delta t^*$ with and without shear rate, the maximum value of $\Delta U^*/\Delta t^*$ is obtained without shear motion. Thus, shear motion is not recommended for MH.

5.2 Bifurcation Diagram

5.2.1 Highest Internal Energy Dissipation

Fig. 5.14 shows the result of the shear rate's amplitude ($\dot{\gamma}_0^*$) sweep for $\alpha = 10$, $\lambda = 1$, Pe = 6, $\phi = 1\%$ and $\omega_S^* = 10$. Figs. 5.14(a) and (b) shows the bifurcation diagram using $\lambda_c = \dot{\gamma}_0^*$ as the control parameter. Fig. 5.14(a) displays the bifurcation diagram for $\overline{M}_z^*$ (in purple), while Fig. 5.14(b) shows the bifurcation diagram for $\overline{M}_y^*$ (in black). Fig. 5.14(c) presents the internal energy dissipation generated at each step of $\dot{\gamma}_0^*$ during the

sweep (blue curve) and the comparison with the internal energy dissipation obtained in isolated simulations (purple curve - the same graph of Fig. 5.7). Still in the Figure 5.14(c), two yellow arrows highlighted the time response of the system at that instant.

The sweep begins at $\dot{\gamma}_0^* = 1$ and ends at $\dot{\gamma}_0^* = 10$. On the bifurcation diagram of Figs. 5.14(a) and (b), some values of $\dot{\gamma}_0^*$ are highlighted by colors (green, cyan, red and pink) and their respective phase space and Poincaré map are shown at each corner of the graph.
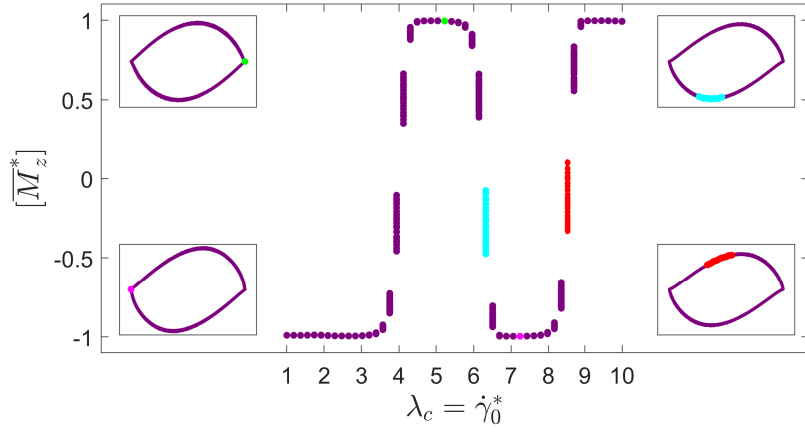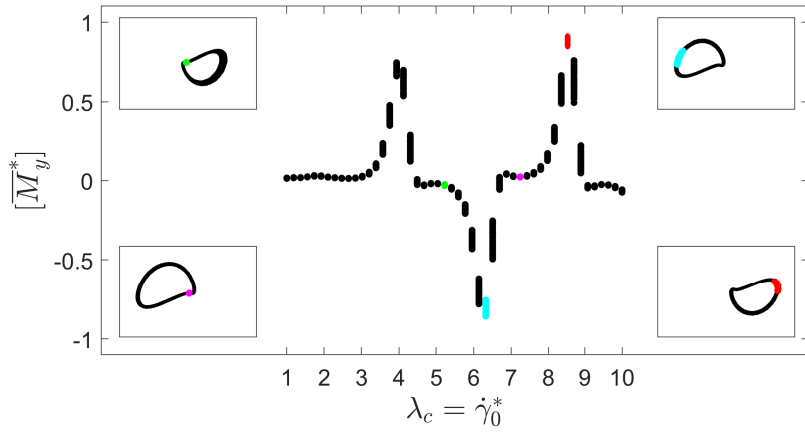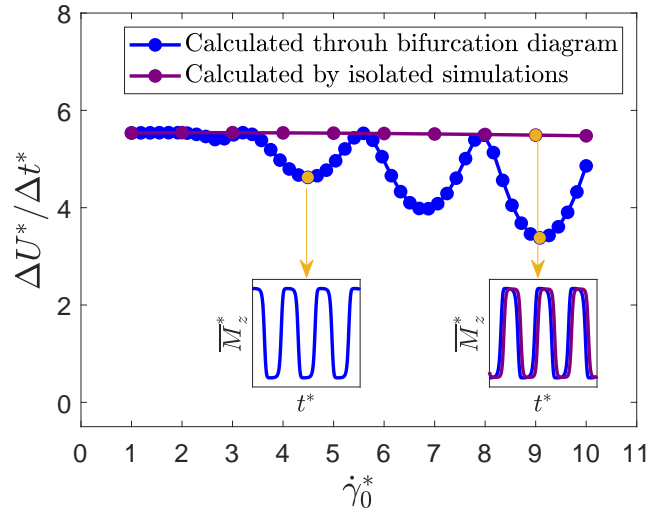
Figure 5.14 – Results of the shear rate's amplitude sweep in steady-state for $\alpha = 10$, $\omega_H^* = 10$, $\lambda = 1$, Pe = 6, $\phi = 1\%$ and $\omega_S^* = 10$. (a) Bifurcation diagram of $[\overline{M}_z^*]$ (on the center) with phase space and Poincaré map of 4 arbitraly chosen points shown at each corner. (b) Bifurcation diagram of $[\overline{M}_y^*]$ (on the center) with phase space and Poincaré map of the same 4 arbitrarily chosen points shown at each corner. (c) Average dissipation of internal energy in isolated simulations (in purple) and average dissipation of internal energy for each point of the bifurcation diagram (in blue) with time response for 2 values (in cyan).

72

In Fig. 5.14(a), the bifurcation diagram of $\overline{M}_z^*$ does not have a point of significant change. On the phase space, the shape of all the phase spaces does not change. The position of the Poincaré map changes in a clockwise way (in the order green - cyan - pink - red). As a result, there are no threshold values in the graph and the system behavior does not change for the $\dot{\gamma}_0^*$ in the $\hat{\mathbf{z}}$ direction. Indeed, Fig. 5.14(a) has the same shape of the bifurcation diagram obtained in Fig. 4.15 using $\lambda_c = \omega_H^*$ as the control variable.

In Fig. 5.14(b), the bifurcation diagram of $\overline{M}_y^*$ shows more changes than in the $\hat{\mathbf{y}}$ direction. The phase space highlighted by the green dot is facing left, while the phase space of the cyan dot is facing right, indicating an inversion has occur between such values.

In Fig. 5.14(c), both the curve of $\Delta U^*/\Delta t^*$ for the $\dot{\gamma}_0^*$ sweep (in blue) and for the fixed values of $\dot{\gamma}_0^*$ (in purple) start at the same point, indicating numerical convergence. However, as the values of $\dot{\gamma}_0^*$ changes during the sweep, the blue line moves away from the purple one, due to nonlinearities of the system. The yellow arrows show the time response at points of divergence between the blue and purple curve. Comparing the difference between the blue and purple time responses, from the rightmost yellow arrow, one can see that the responses are similar and only differ slightly by the amplitude, which explains the difference of the value in $\Delta U^*/\Delta t^*$.

5.2.2   Low Shear Rate's Frequencies

Fig. 5.15 displays the same results from the previous section, with the exception of the value $\omega_S^* = 1$, a lower frequency of the shear rate. In other words, a $\dot{\gamma}_0^*$ sweep is made with $\alpha = 10$, $\omega_H^* = 10$, $\lambda = 1$, $\text{Pe} = 6$, $\phi = 1\%$ and $\omega_S^* = 1$. Fig. 5.15 (a) and (b) display the bifurcation diagram with phase space at the $\hat{\mathbf{z}}$ and at the at the $\hat{\mathbf{y}}$ direction, respectively.
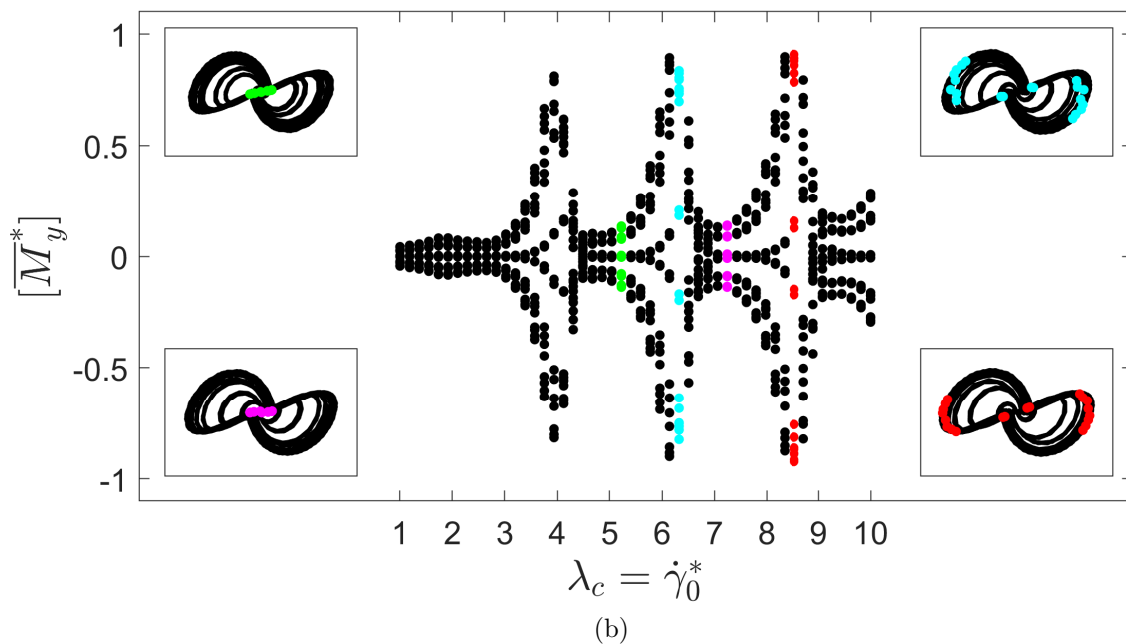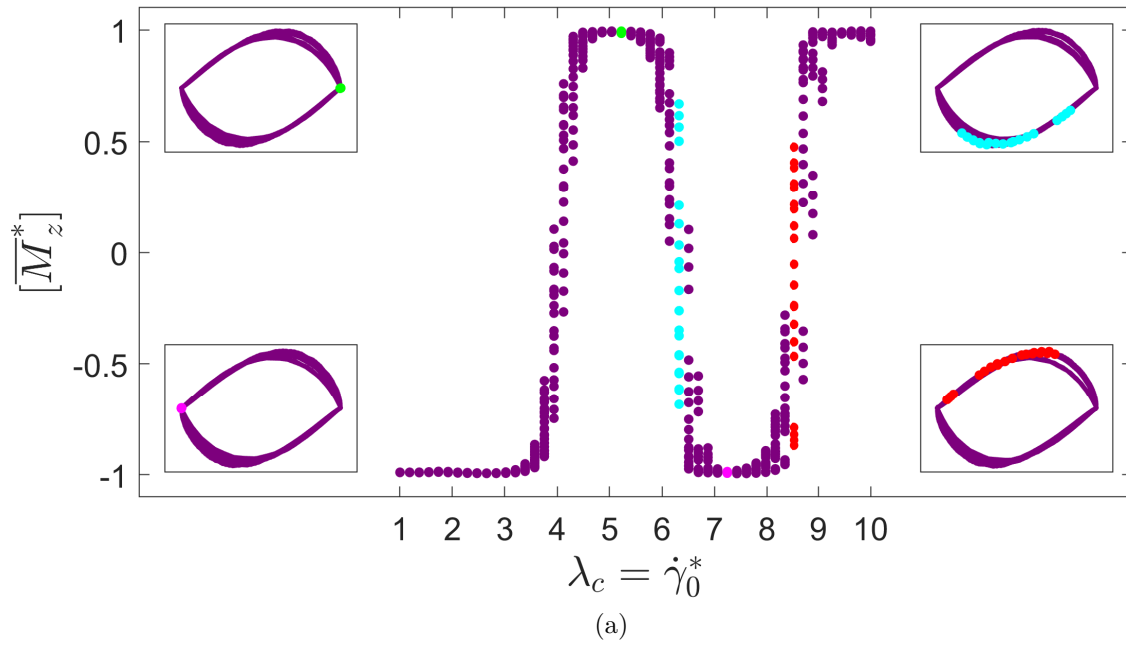
Figure 5.15 – Bifurcation diagram of the shear rate's amplitude sweep in steady-state for $\alpha = 10$, $\omega_H^* = 10$, $\lambda = 1$, Pe $= 6$, $\phi = 1\%$ and $\omega_S^* = 1$. Phase space and Poincaré map of 4 arbitraly chosen points (green, cyan, pink and red) shown at each corner. (a) Bifurcation diagram of the $\hat{\mathbf{z}}$ direction (in purple). (b) Bifurcation diagram of the $\hat{\mathbf{y}}$ direction (in black).

In Fig. 5.15(a), the bifurcation diagram of $\overline{M}_z^*$ has the same behavior of Fig. 5.14(a). The only difference is that the curves of the phase spaces are more dense in the present simulation, because, with a lower frequency of the shear rate, the system takes more time to achieve steady-state condition. Again, no threshold value of the bifurcation diagram is remarkable.

In Fig. 5.15(b), the phase spaces from all points is the same. The dots from the Poincaré map change position, due to the different frequencies $\omega_H^* = 10$ and ω_S^*. Lastly, there are no threshold values in this simulation.

Fig. 5.16 displays the same results from the previous section, with value $\omega_S^* = 5$, an intermediary value of the shear rate's frequency. In other words, a $\dot{\gamma}_0^*$ sweep is made with $\alpha = 10$, $\omega_H^* = 10$, $\lambda = 1$, $Pe = 6$, $\phi = 1\%$ and $\omega_S^* = 5$. Fig. 5.16 (a) and (b) display the bifurcation diagram with phase space at the $\hat{\mathbf{z}}$ and at the at the $\hat{\mathbf{y}}$ direction, respectively.
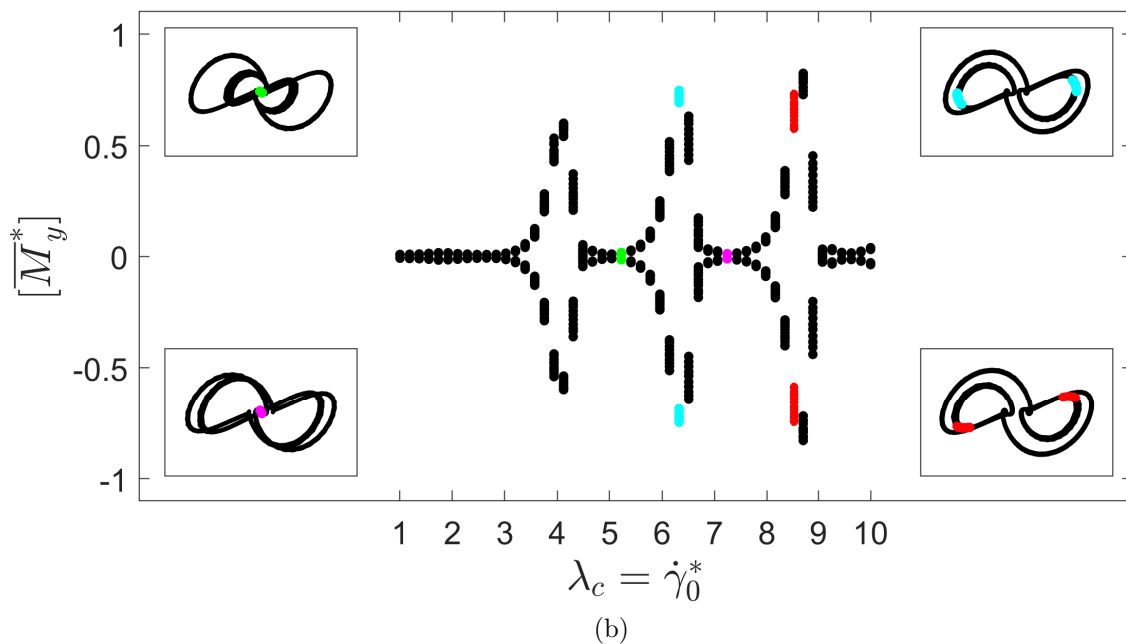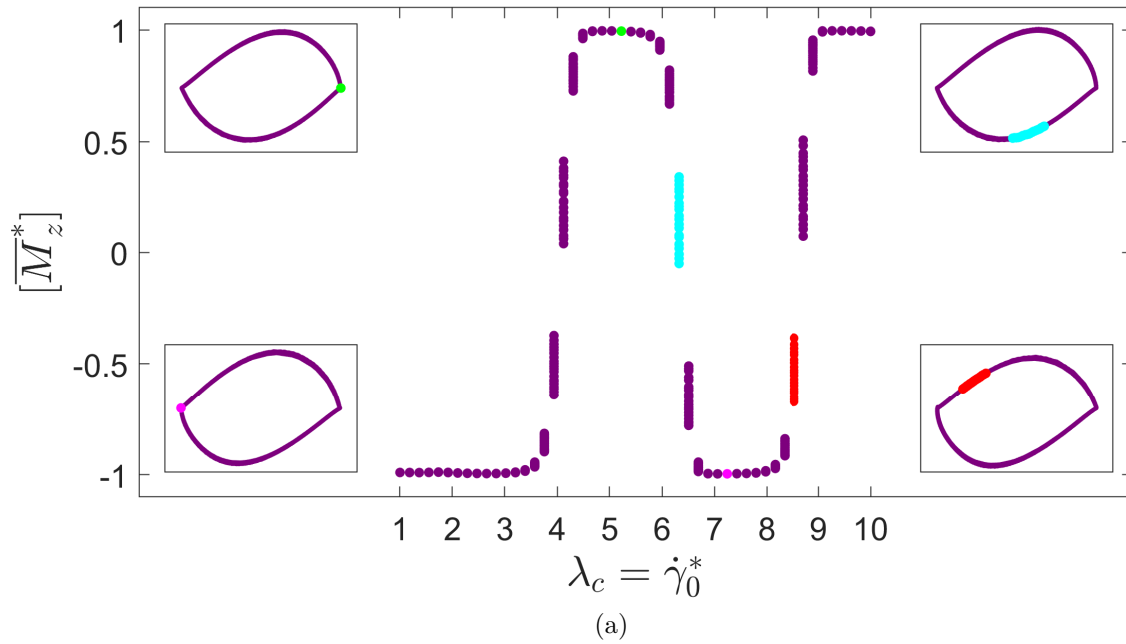
Figure 5.16 – Bifurcation diagram of the shear rate's amplitude sweep in steady-state for $\alpha = 10$, $\omega_H^* = 10$, $\lambda = 1$, Pe $= 6$, $\phi = 1\%$ and $\omega_S^* = 5$. Phase space and Poincaré map of 4 arbitraly chosen points (green, cyan, pink and red) shown at each corner. (a) Bifurcation diagram of the $\hat{\mathbf{z}}$ direction (in purple). (b) Bifurcation diagram of the $\hat{\mathbf{y}}$ direction (in black).

In Fig. 5.16(a), the bifurcation diagram of $\overline{M}_z^*$ shows that, for a intermediary frequency of the shear rate, the system has reached steady-state faster (the phase space is a thin curve). The graph of Fig. 5.16(a) is more similar to Fig. 5.14(a) than Fig. 5.15(a), because the graph of Fig. 5.15(a) has not reached the steady-state. Again, no threshold value can be deduced, as the phase space does not change and the Poincaré map only

changes position clockwise.

In Fig. 5.16(b), the phase space from the points highlighted changes significantly. The inner shape observed at the green dot phase space has increased its size in the cyan dot phase space and even more in the pink dot phase space. However, at the red dot simulation, the phase space and the Poincaré map are the same of the cyan simulation, which indicates a recurring behavior of the bifurcation diagram.

5.2.3   Low Langevin Parameter and Low Péclet Number

Most bifurcation diagrams in previous simulations have the same behavior, due to the high values of $\alpha = 10$ and $\mathrm{Pe} = 6$ and the predominance of the magnetic field. Because of this, bifurcation diagrams with low values of α and Pe is made.

Fig. 5.17 shows the bifurcation diagram for a low α and high Pe, with values $\alpha = 1$, $\mathrm{Pe} = 6$, $\omega_H^* = 10$, $\lambda = 1$, $\phi = 1\%$ and $\omega_S^* = 10$. Fig. 5.17 (a) and (b) display the bifurcation diagram with phase space at the $\hat{\mathbf{z}}$ and at the at the $\hat{\mathbf{y}}$ direction, respectively.
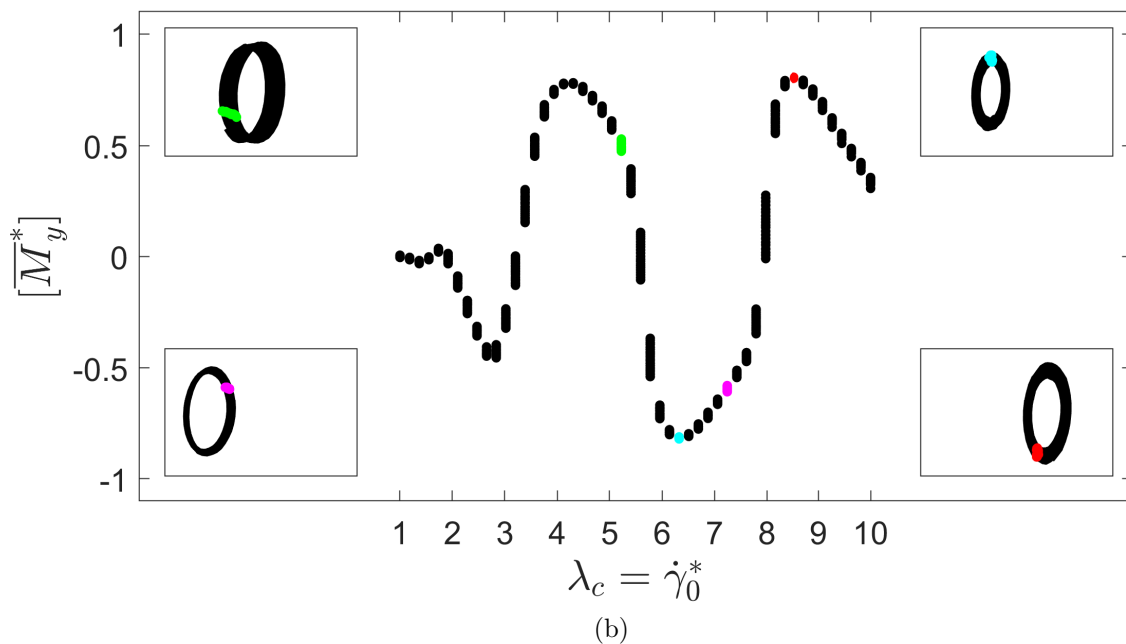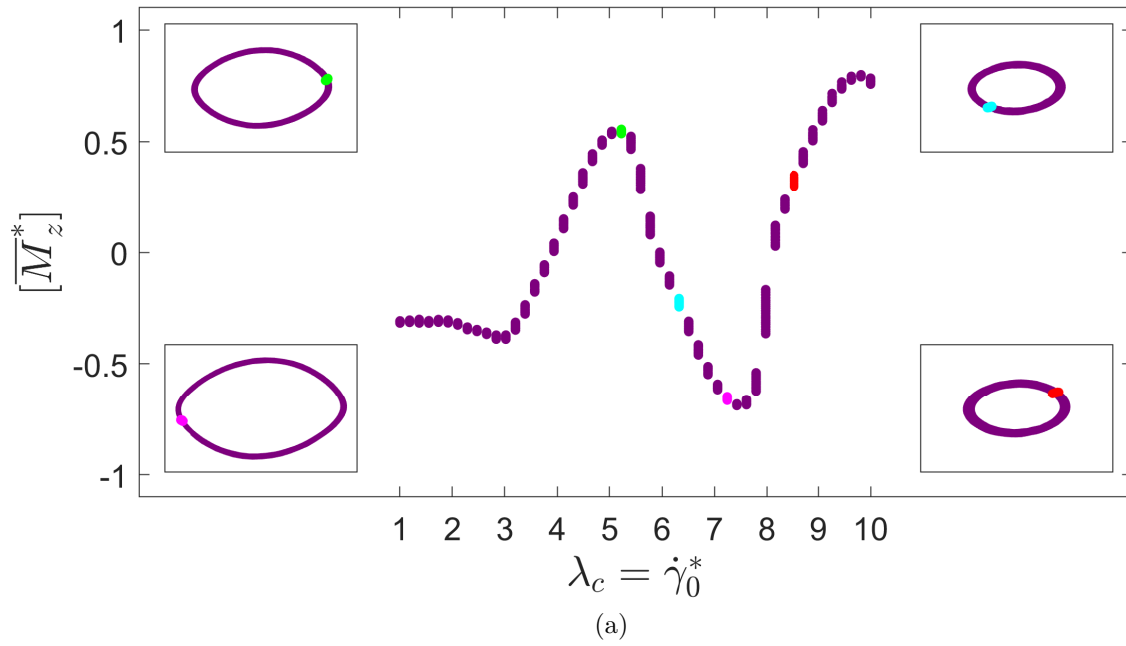
Figure 5.17 – Bifurcation diagram of the shear rate's amplitude sweep in steady-state for $\alpha = 1$, $\omega_H^* = 10$, $\lambda = 1$, $\mathrm{Pe} = 6$, $\phi = 1\%$ and $\omega_S^* = 10$. Phase space and Poincaré map of 4 arbitraly chosen points (green, cyan, pink and red) shown at each corner. (a) Bifurcation diagram of the $\hat{\mathbf{z}}$ direction (in purple). (b) Bifurcation diagram of the $\hat{\mathbf{y}}$ direction (in black).

In Figs. 5.17(a) and (b), the bifurcations diagrams do not present any threshold values. However, due to the low values of α, the rate of change of the bifurcation diagram is lower than in previous simulations.

Fig. 5.18 shows the bifurcation diagram for a low α and low Pe, with values $\alpha = 1$, $\mathrm{Pe} = 1$, $\omega_H^* = 10$, $\lambda = 1$, $\phi = 1\%$ and $\omega_S^* = 10$. Fig. 5.17 (a) and (b) display the bifurcation

diagram with phase space at the $\hat{\mathbf{z}}$ and at the at the $\hat{\mathbf{y}}$ direction, respectively.

(a)

(b)
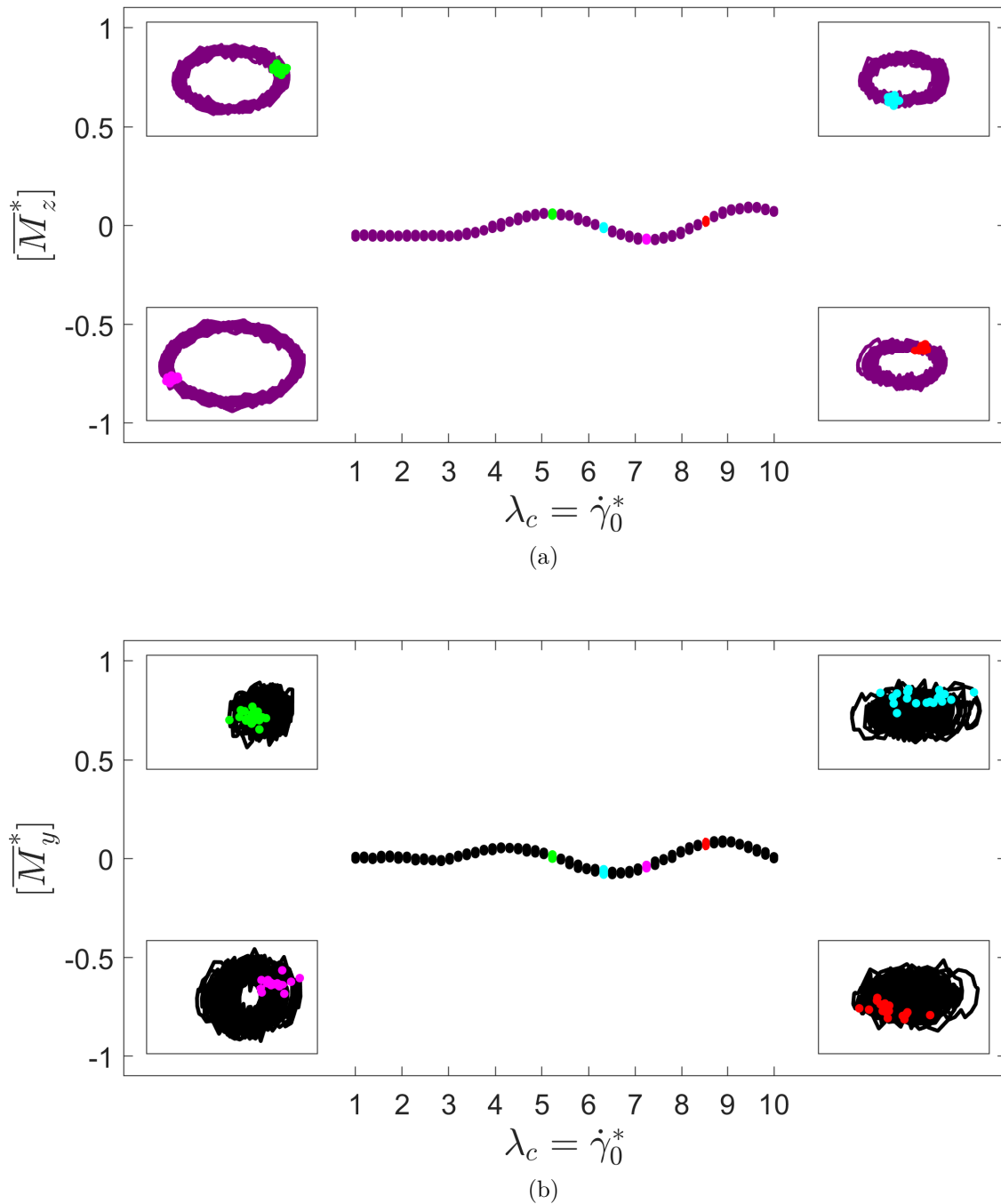
Figure 5.18 – Bifurcation diagram of the shear rate's amplitude sweep in steady-state for $\alpha = 1$, $\omega_H^* = 10$, $\lambda = 1$, Pe $= 1$, $\phi = 1\%$ and $\omega_S^* = 10$. Phase space and Poincaré map of 4 arbitrarily chosen points (green, cyan, pink and red) shown at each corner. (a) Bifurcation diagram of the $\hat{\mathbf{z}}$ direction (in purple). (b) Bifurcation diagram of the $\hat{\mathbf{y}}$ direction (in black).

In Figs. 5.18(a) and (b), once again, the bifurcations diagrams do not present any threshold values. Due to the low values of both α and Pe, the rate of change of the bifurcation diagram is lower than in previous simulations, approaching a horizontal line. Seeing the phase spaces and each corner of Figs. 5.18(a) and (b), one can note how

the phase spaces are noisier and more random. This is due the low α, which means the brownian random motion has more contribution to the dynamics of the MNPs from the system.

6 Results of Chaotic Magnetic Field

"*Young man, in mathematics you don't understand things. You just get used to them.*"

John von Neumann joking to Felix Smith

In this chapter, with the goal of obtaining chaotic responses, a two-dimensional chaotic external magnetic field is applied. At first, the Arnold equations (Bae, 2004) is used to generate a chaotic time series as follows,

$$
\begin{cases}
\dot{x}_1 = A\sin(x_3) + C\cos(x_2) \\
\dot{x}_2 = B\sin(x_1) + A\cos(x_3)\ , \\
\dot{x}_3 = C\sin(x_2) + B\cos(x_1)
\end{cases}
\tag{6.1}
$$

where A, B and C are constants and x_1, x_2 and x_3 are the state variables.

The Arnold equation represents the steady-state solution of the three-dimensional Euler equation, which describes incompressible flow of fluids on a 3D torus space (Nakamura; Sekiguchi, 2001). As reported by the author, such equation is used to impose chaotic motion to a two-wheeled mobile robot. One advantage of the Arnold equation is the control of its behavior using the constant C: if C is 0 or small, the equation displays periodic behavior; if C is large, the equation displays chaotic behavior (Okamoto; Fujii, 1995). In this work, the value $C = 0.5$ is used.

The Arnold equation is implemented in the $\hat{\mathbf{y}}$ and $\hat{\mathbf{z}}$ direction of the external magnetic field as shown in Eq. (6.2), thus, the magnetic field in the $\hat{\mathbf{y}}$-$\hat{\mathbf{z}}$ plane presents a chaotic behavior:

$$
\begin{cases}
\dot{x}_1 = A\sin(x_3) + C\cos(x_2) \\
\dot{x}_2 = B\sin(x_1) + A\cos(x_3) \\
\dot{x}_3 = C\sin(x_2) + B\cos(x_1)\ , \\
\dot{\hat{H}}_y = v\sin(x_3) \\
\dot{\hat{H}}_z = v\cos(x_3)
\end{cases}
\tag{6.2}
$$

where v is the linear velocity of mobile robot and x_3 is the steering angle of the mobile robot. The constants values chosen are $v = 1$, $A = 1$, $B = 0.5$, $C = 0.5$. The initial

conditions chosen are $x_1(0) = 0$, $x_2(0) = 0$, $x_3(0) = 0$, $\hat{H}_y(0) = 0$ and $\hat{H}_z(0) = 0$. The $\hat{\mathbf{x}}$ component of the magnetic field is always equal to zero, $\hat{H}_x = 0$. As the magnetic field is nonlinear, it can reach very high values. To prevent this, mirror mapping is applied for the values $\hat{H}_y = 1$, $\hat{H}_y = -1$, $\hat{H}_z = 1$ and $\hat{H}_z = -1$, such that the magnetic field is reflected, preserving its angle (Bae, 2004). To exemplify this, Fig. 6.1 shows the magnetic field from $\hat{\mathbf{y}}$ and $\hat{\mathbf{z}}$ directions obtained from the Arnold equation with mirror mapping. Because of the mirror mapping, for a long period of time, the magnetic field covers all space between -1 and 1, as shown in Fig. 6.1(c).

(a)

(b)

(c)
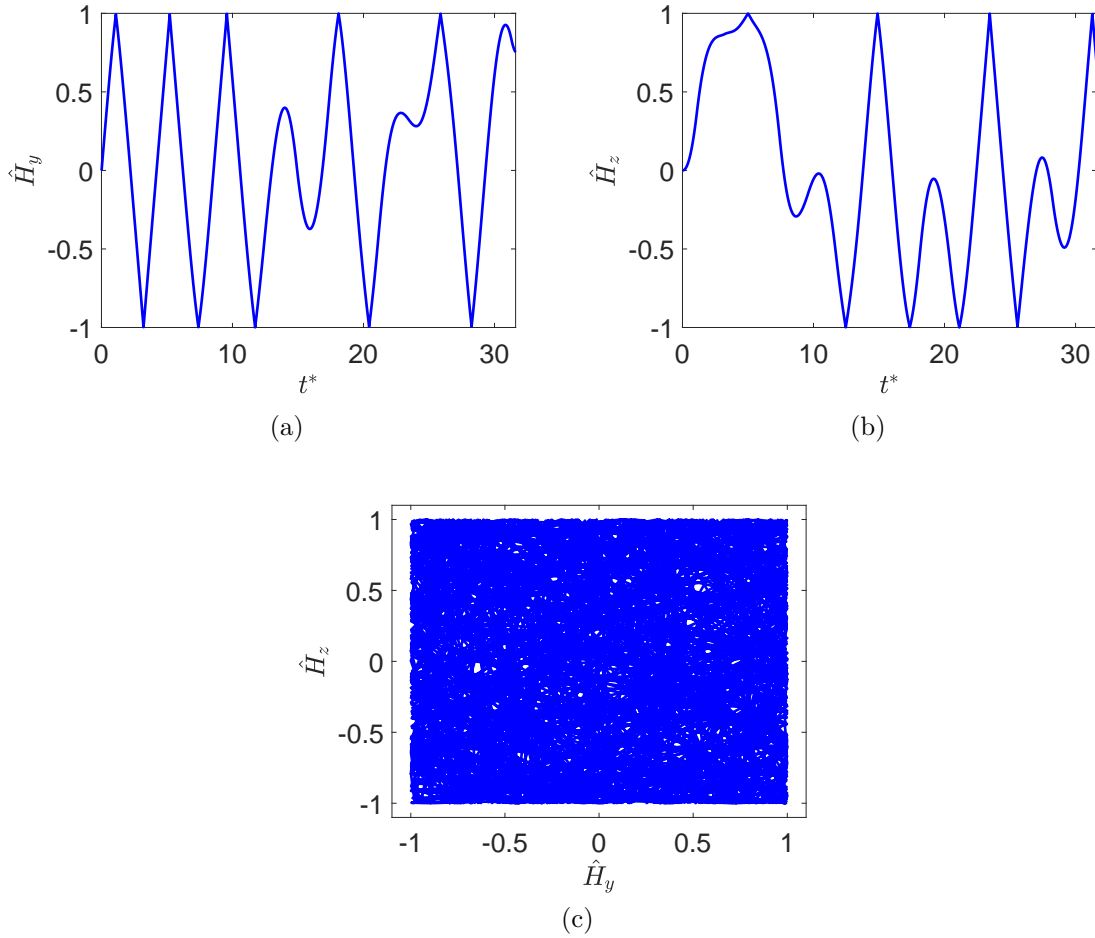
Figure 6.1 – Time evolution of the two-dimensional magnetic field ($\hat{H}_y$ and $\hat{H}_z$) under chaotic behavior from the Arnold equation. Each time the value 1 or -1 is reached by $\hat{H}_y$ or $\hat{H}_z$, magnetic field is reflected preserving its angle. (a) $\hat{H}_y$ vs t^*. (b) $\hat{H}_z$ vs t^*. (c) $\hat{H}_y$ vs $\hat{H}_z$.

As the magnetic field is two-dimensional and nonperiodic, the expression used in this chapter for the dimensionless average rate of internal energy is

$$\frac{\Delta U^*}{\Delta t^*} = \frac{1}{t_f^*} \left\{ \int_{\overline{M}_y^*(0),\hat{H}_y(0)}^{\overline{M}_y^*\left(t_f^*\right),\hat{H}_y\left(t_f^*\right)} \hat{H}_y \,\mathrm{d}\overline{M}_y^* + \int_{\overline{M}_z^*(0),\hat{H}_z(0)}^{\overline{M}_z^*\left(t_f^*\right),\hat{H}_z\left(t_f^*\right)} \hat{H}_z \,\mathrm{d}\overline{M}_z^* + \right.$$
$$\left. + \frac{\alpha}{48\phi\lambda} \left[\hat{H}_y\left(t_f^*\right)^2 + \hat{H}_z\left(t_f^*\right)^2 - \hat{H}_y\left(0\right)^2 - \hat{H}_z\left(0\right)^2 \right] \right\} \quad (6.3)$$

Hence, in this chapter, the dissipation of internal energy is calculated by the area of the hysteresis curve in the $\hat{\mathbf{y}}$ and $\hat{\mathbf{z}}$ direction and by the initial and final condition of the external magnetic field, $\hat{H}_y\left(0\right)$, $\hat{H}_z\left(0\right)$, $\hat{H}_y\left(t_f^*\right)$ and $\hat{H}_z\left(t_f^*\right)$.

Fig. 6.2 shows the system treated in this chapter. A chaotic magnetic field is applied in the $\hat{\mathbf{z}}$ and in in the $\hat{\mathbf{y}}$ directions.
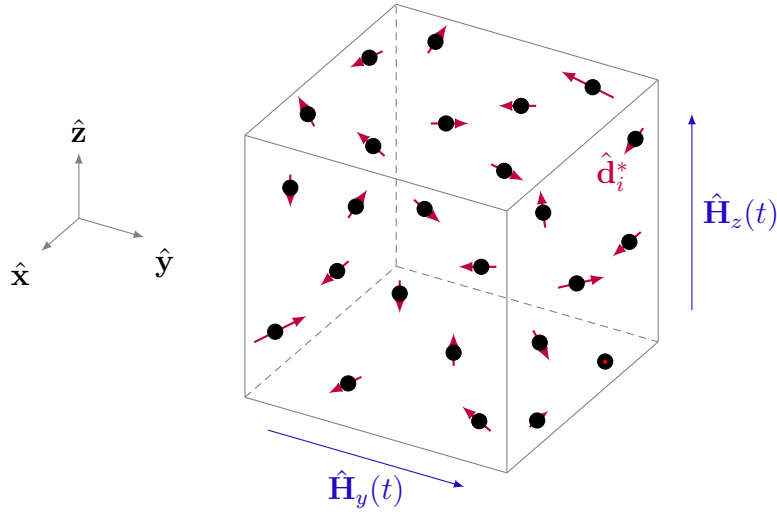
Figure 6.2 – Representation of the system analyzed in this chapter. A chaotic magnetic field is applied in the $\hat{\mathbf{z}}$ and $\hat{\mathbf{y}}$ directions ($\hat{\mathbf{H}}_y$ and $\hat{\mathbf{H}}_z$). Particles are represented by black dots and their dipole vector in red ($\hat{\mathbf{d}}_i$).

6.1   Langevin Parameter Scan

A parameter scan for α is performed. Figures 6.3 and 6.4 display the results of chaotic magnetic field, in steady-state regime, with the values Pe $= 6$, $\lambda = 1$ and $\phi = 1\%$, varying α from $\alpha = 1$ to $\alpha = 10$.
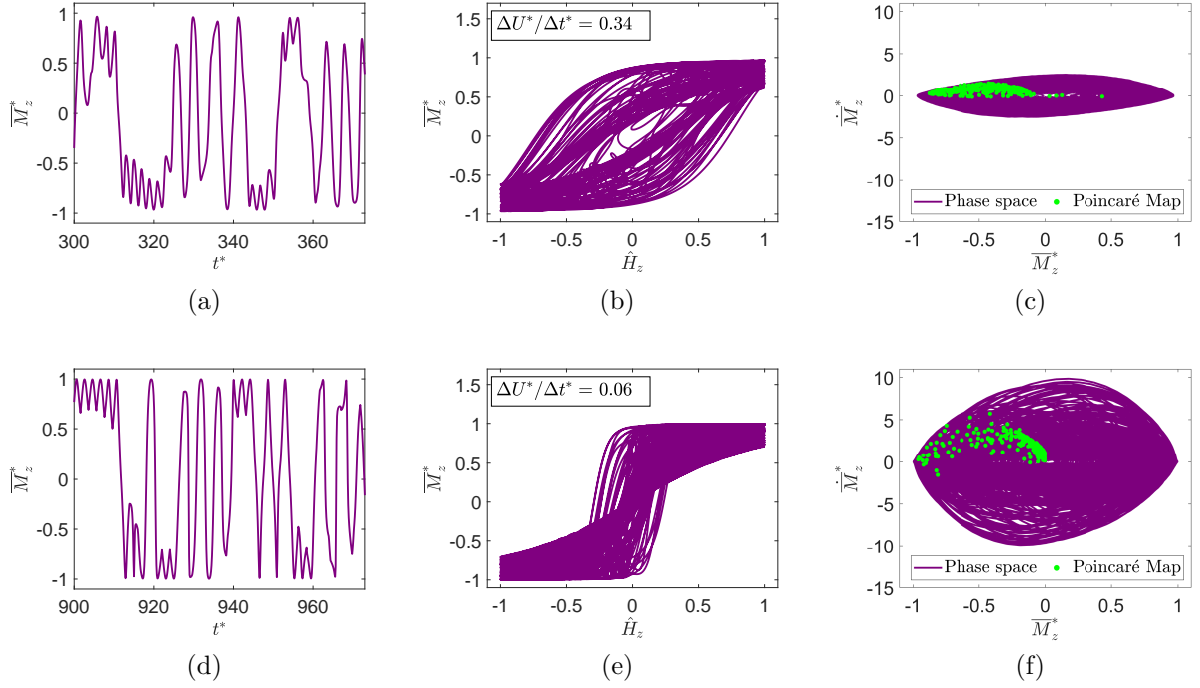
Figure 6.3 – Scan of the Langevin parameter (α) with Pe = 6 and $\phi = 1\%$ for chaotic magnetic field. (a), (b) and (c): $\alpha = 1$. (d), (e) and (f): $\alpha = 10$. (a) and (d): Time response in the $\hat{\mathbf{z}}$ direction. (b) and (e): Hysteresis curve in the $\hat{\mathbf{z}}$ direction and dimensionless average rate of internal energy (upper left corner). (c) and (f): Phase space in the $\hat{\mathbf{z}}$ direction.

In Fig. 6.3 (a) and (d), one can see that the time responses do not surpass the values -1 and 1, due to the saturation magnetization. The time response in the $\hat{\mathbf{z}}$ direction for $\alpha = 1$ in Fig. 6.3 (a) is different from the time response for $\alpha = 10$ in Fig. 6.3 (d), even though the magnetic field is the same. In Fig. 6.3 (b) and (e), the hysteresis curve are almost filled. The value of $\Delta U^*/\Delta t^*$ already considers the contribution of both hysteresis curves in the $\hat{\mathbf{z}}$ and $\hat{\mathbf{y}}$ direction and the contribution of the magnetic field. The hysteresis curve for $\alpha = 1$ in Fig. 6.3 (b) has a bigger area than the hysteresis curve for $\alpha = 1$ in Fig. 6.3 (e). Lastly, in Fig. 6.3 (c) and (f), the phase spaces are almost filled. The phase space for $\alpha = 10$ is bigger than the phase space for $\alpha = 1$. The reflection of the magnetic field's mirror mapping is observed at the sharp points of $(1, 0)$ and $(-1, 0)$ in both phase spaces.
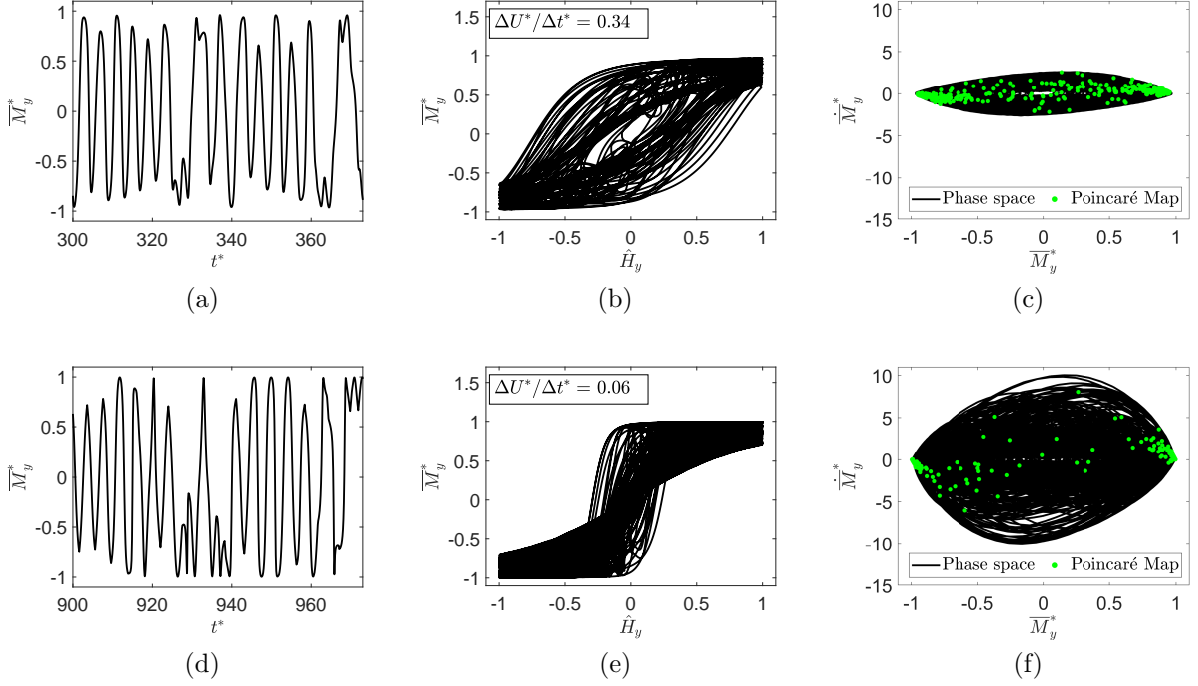
Figure 6.4 – Scan of the Langevin parameter (α) with Pe = 6 and $\phi = 1\%$ for chaotic magnetic field in the $\hat{\mathbf{y}}$ direction. (a), (b) and (c): $\alpha = 1$. (d), (e) and (f): $\alpha = 10$. (a) and (d): Time response in the $\hat{\mathbf{z}}$ direction. (b) and (e): Hysteresis curve in the $\hat{\mathbf{z}}$ direction and dimensionless average rate of internal energy (upper left corner). (c) and (f): Phase space in the $\hat{\mathbf{z}}$ direction.

In Fig. 6.4 (a) and (d), the time responses in the $\hat{\mathbf{y}}$ direction have a similar behavior from the time responses in the $\hat{\mathbf{z}}$ direction, such that both may present chaotic behavior. The hysteresis curve in the $\hat{\mathbf{y}}$ direction for $\alpha = 1$ in Fig. 6.4 (b) is bigger than the hysteresis curve in the $\hat{\mathbf{y}}$ direction for $\alpha = 10$ in Fig. 6.4 (e). Because both hysteresis curve for $\alpha = 1$ are bigger than the ones for $\alpha = 10$, the value of $\Delta U^*/\Delta t^*$ is higher for $\alpha = 1$. However, the value $\Delta U^*/\Delta t^* = 0.34$ is lower than the one obtained in alternating magnetic field. Lastly, in Fig. 6.4 (c) and (f), the phase spaces in the $\hat{\mathbf{y}}$ direction have the same behavior from the ones in the $\hat{\mathbf{z}}$ direction.

7 Conclusion and Future Work

"Unfortunately what is little recognized is that the most worthwhile scientific books are those in which the author clearly indicates what he does not know; for an author most hurts his readers by concealing difficulties."

Évariste Galois

In this work, the performance of MH is evaluated from the dissipation of internal energy of a nonlinear system of magnetic particles for different parameters and excitation. The dynamical analysis of the system is carried out by means of time responses, phase spaces, Poicaré maps and bifurcation diagrams. Three main situations are studied: pure alternating magnetic field, alternating magnetic field with alternating shear rate and chaotic magnetic field with alternating shear rate.

In the case of pure alternating magnetic field, it is observed that, under relaxation, the system has a null natural frequency. The variation of the volume fraction does not change significantly the results; a higher average rate of internal energy dissipation is obtained with high ω_H^* (the most sensitive variable for the internal energy) meaning that a more powerful magnetic field is desirable; and it is shown the average rate of internal energy dissipation decreases if the system remains in the saturation magnetization. The bifurcation diagram for ω_H^* showed no qualitative change in the system.

Concerning alternating magnetic field with alternating shear rate, the scan of the shear rate's variables for high α and high Pe indicated that the internal energy did not changed and the results in the $\hat{\mathbf{z}}$ direction remained the same as well. This is due to the predominance of the magnetic field over the dipoles of the MNPs, producing always the same amount of magnetic work. For a low α and low Pe, the results indicated that a low ω_S^* (the most sensitive variable for the internal energy) and a low $\dot{\gamma}_0^*$ increased the average rate of internal energy dissipation. The values obtained for $\Delta U^*/\Delta t^*$ with shear are lower compared to the values of pure alternating magnetic field. Moreover, the Fourier transform of the time response pointed frequencies equal to the frequencies of the magnetic field or shear rate. For a high α, the bifurcation diagram for $\dot{\gamma}_0^*$ showed the same behavior from the bifurcation diagram of ω_H^* without shear rate, due to the predominance of the magnetic field. For a low value of α and Pe, the bifurcation diagrams changed, but revealed no qualitative changes in the system.

The last analyzed case consisted in an excitation to impose chaotic behavior. With respect to chaotic magnetic field, the scan of the Langevin parameter showed that a low α increased the average rate of internal energy dissipation. From the 3 excitation considered, the pure alternating magnetic field produced the best dynamical behavior for MH.

For future work, it is suggested investigating the dynamical response of the particulate system considering hydrodynamic interactions with mobility formulation (Gontijo; Cunha, 2017), (Gontijo; Cunha, 2017). For this condition, the existence of the liquid carrier between magnetic particles is assumed. The forces upon each particle is calculated by the mobility matrix and the translation of particles affects greatly the dynamic of neighboring particles. With this, the results produced are more precise than the ones obtained in this work. However, because of the high number of lattices, the computational times of the simulations are high.

Bibliography

Arias, L. S. et al. Iron oxide nanoparticles for biomedical applications: a perspective on synthesis, drugs, antimicrobial activity, and toxicity. *Antibiotics*, Multidisciplinary Digital Publishing Institute, v. 7, n. 2, p. 46, 2018. Quoted 2 times on pages xiv and 3.

Bae, Y. Obstacle avoidance method in the chaotic robot. In: IEEE. *The 23rd Digital Avionics Systems Conference (IEEE Cat. No. 04CH37576)*. 2004. v. 2, p. 12–D. Quoted 2 times on pages 81 and 82.

Barbosa, W. et al. Chaos control applied to piezoelectric vibration-based energy harvesting systems. *The European Physical Journal Special Topics*, Springer, v. 224, n. 14, p. 2787–2801, 2015. Quoted on page 36.

Beenakker, C. Ewald sum of the Rotne-Prager tensor. *The Journal of chemical physics*, American Institute of Physics, v. 85, n. 3, p. 1581–1582, 1986. Quoted 2 times on pages 31 and 33.

Bibo, A. et al. Electromagnetic ferrofluid-based energy harvester. *Physics Letters A*, Elsevier, v. 376, n. 32, p. 2163–2166, 2012. Quoted on page 4.

Blanco-Andujar, C. et al. Current outlook and perspectives on nanoparticle-mediated magnetic hyperthermia. In: *Iron oxide nanoparticles for biomedical applications.* : Elsevier, 2018. p. 197–245. Quoted on page 2.

Bottenberg, W. et al. The dependence of loudspeaker design parameters on the properties of magnetic fluids. *Journal of the Audio Engineering Society*, Audio Engineering Society, v. 28, n. 1/2, p. 17–25, 1980. Quoted on page 4.

Carrey, J. et al. Simple models for dynamic hysteresis loop calculations of magnetic single-domain nanoparticles: Application to magnetic hyperthermia optimization. *Journal of Applied Physics*, American Institute of Physics, v. 109, n. 8, p. 083921, 2011. Quoted on page 1.

Coisson, M. et al. Hysteresis losses and specific absorption rate measurements in magnetic nanoparticles for hyperthermia applications. *Biochimica et Biophysica Acta (BBA)-General Subjects*, Elsevier, v. 1861, n. 6, p. 1545–1558, 2017. Quoted on page 2.

Cunha, F. et al. Modeling and direct simulation of velocity fluctuations and particle-velocity correlations in sedimentation. *J. Fluids Eng.*, v. 124, n. 4, p. 957–968, 2002. Quoted 4 times on pages xv, 16, 31, and 32.

Einstein, A. *Investigations on the Theory of the Brownian Movement.* : Courier Corporation, 1956. Quoted 2 times on pages 15 and 16.

Ewald, P. P. Die Berechnung optischer und elektrostatischer Gitterpotentiale. *Annalen der physik*, Wiley Online Library, v. 369, n. 3, p. 253–287, 1921. Quoted on page 31.

Finlayson, B. A. Spin-up of ferrofluids: The impact of the spin viscosity and the langevin function. *Physics of Fluids*, American Institute of Physics, v. 25, n. 7, p. 073101, 2013. Quoted on page 2.

Gilchrist, R. et al. Selective inductive heating of lymph nodes. *Annals of surgery*, Lippincott, Williams, and Wilkins, v. 146, n. 4, p. 596, 1957. Quoted on page 2.

Gontijo, R.; Cunha, F. Dynamic numerical simulations of magnetically interacting suspensions in creeping flow. *Powder technology*, Elsevier, v. 279, p. 146–165, 2015. Quoted 15 times on pages xiv, xv, 2, 8, 10, 11, 12, 14, 15, 16, 17, 24, 30, 31, and 33.

Gontijo, R.; Cunha, F. Numerical simulations of magnetic suspensions with hydrodynamic and dipole-dipole magnetic interactions. *Phys. Fluids*, AIP Publishing LLC, v. 29, n. 6, p. 062004, 2017. Quoted on page 87.

Gontijo, R. G. *Micromecânica e microhidrodinâmica de suspensões magnéticas*. 2013. Tese (Doutorado) — Departamento de Engenharia Mecânica, Universidade de Brasília, Brasília, DF, Publicação ENM.TD - 19A, 262p. Quoted on page 2.

Gontijo, R. G.; Cunha, F. R. On the interplay between hydrodynamic and dipolar particle interactions in suspensions. In: *APS Division of Fluid Dynamics Meeting Abstracts*. 2017. p. E36–003. Quoted on page 87.

Guimarães, A. et al. The influence of hydrodynamic effects on the complex susceptibility response of magnetic fluids undergoing oscillatory fields: New insights for magnetic hyperthermia. *Physics of Fluids*, AIP Publishing LLC, v. 32, n. 1, p. 012008, 2020. Quoted 2 times on pages 15 and 16.

Hajdu, S. I. A note from history: landmarks in history of cancer, part 1. *Cancer*, Wiley Online Library, v. 117, n. 5, p. 1097–1102, 2011. Quoted on page 1.

Haw, C. Y. et al. Hydrothermal synthesis of magnetite nanoparticles as mri contrast agents. *Ceramics International*, Elsevier, v. 36, n. 4, p. 1417–1422, 2010. Quoted on page 2.

Hildebrandt, B. et al. The cellular and molecular basis of hyperthermia. *Critical reviews in oncology/hematology*, Elsevier, v. 43, n. 1, p. 33–56, 2002. Quoted on page 1.

Hilger, I. et al. Towards breast cancer treatment by magnetic heating. *Journal of Magnetism and Magnetic Materials*, Elsevier, v. 293, n. 1, p. 314–319, 2005. Quoted on page 3.

Hsu, A. et al. Ferrofluid levitated micro/milli-robots. In: IEEE. *2018 International Conference on Manipulation, Automation and Robotics at Small Scales (MARSS)*. 2018. p. 1–7. Quoted on page 4.

Huang, C. et al. Damping applications of ferrofluids: a review. *Journal of Magnetics*, The Korean Magnetics Society, v. 22, n. 1, p. 109–121, 2017. Quoted 3 times on pages 2, 4, and 30.

Huang, W. et al. Study on the ferrofluid lubrication with an external magnetic field. *Tribology Letters*, Springer, v. 41, n. 1, p. 145–151, 2011. Quoted on page 4.

Ito, A. et al. Heat-inducible tnf-α gene therapy combined with hyperthermia using magnetic nanoparticles as a novel tumor-targeted therapy. *Cancer gene therapy*, Nature Publishing Group, v. 8, n. 9, p. 649–654, 2001. Quoted on page 3.

Johannsen, M. et al. Magnetic nanoparticle hyperthermia for prostate cancer. *International Journal of Hyperthermia*, Taylor & Francis, v. 26, n. 8, p. 790–795, 2010. Quoted on page 3.

Kakavandi, B. et al. Pb (II) adsorption onto a magnetic composite of activated carbon and superparamagnetic Fe_3O_4 nanoparticles: experimental and modeling study. *CLEAN–Soil, Air, Water*, Wiley Online Library, v. 43, n. 8, p. 1157–1166, 2015. Quoted on page 4.

Kamiyama, S. et al. Study on regulating characteristics of magnetic fluid active damper. *Energy conversion and management*, Elsevier, v. 43, n. 3, p. 281–287, 2002. Quoted on page 4.

Kole, M.; Khandekar, S. Engineering applications of ferrofluids: A review. *Journal of Magnetism and Magnetic Materials*, Elsevier, p. 168222, 2021. Quoted on page 4.

Kondo, S. et al. Vibrating properties of a magnetic-fluid tuned liquid column damper with different u-pipes. In: Trans Tech Publ. *Materials Science Forum*. 2016. v. 856, p. 21–25. Quoted on page 4.

Landeghem, F. K. van et al. Post-mortem studies in glioblastoma patients treated with thermotherapy using magnetic nanoparticles. *Biomaterials*, Elsevier, v. 30, n. 1, p. 52–57, 2009. Quoted on page 3.

Laroze, D. et al. Chaotic convection in a ferrofluid. *Communications in Nonlinear Science and Numerical Simulation*, Elsevier, v. 18, n. 9, p. 2436–2447, 2013. Quoted on page 4.

Lee, S.-J. et al. Synthesis and characterization of superparamagnetic maghemite nanoparticles prepared by coprecipitation technique. *Journal of Magnetism and Magnetic Materials*, Elsevier, v. 282, p. 147–150, 2004. Quoted on page 2.

Liu, J. Analysis of a porous elastic sheet damper with a magnetic fluid. *Journal of Tribology*, 2009. Quoted on page 4.

Liu, X. et al. Comprehensive understanding of magnetic hyperthermia for improving antitumor therapeutic efficacy. *Theranostics*, Ivyspring International Publisher, v. 10, n. 8, p. 3793, 2020. Quoted 2 times on pages 1 and 2.

Maity, D. et al. Synthesis of magnetite nanoparticles via a solvent-free thermal decomposition route. *Journal of Magnetism and Magnetic Materials*, Elsevier, v. 321, n. 9, p. 1256–1259, 2009. Quoted on page 2.

Malvar, S. et al. Nonlinear motion of an oscillating bubble immersed in a magnetic fluid. *J. Engin. Mathe.*, Springer, v. 108, n. 1, p. 143–170, 2018. Quoted on page 4.

Nakamura, Y.; Sekiguchi, A. The chaotic mobile robot. *IEEE Transactions on Robotics and Automation*, IEEE, v. 17, n. 6, p. 898–904, 2001. Quoted on page 81.

Neuberger, T. et al. Superparamagnetic nanoparticles for biomedical applications: possibilities and limitations of a new drug delivery system. *Journal of Magnetism and Magnetic materials*, Elsevier, v. 293, n. 1, p. 483–496, 2005. Quoted on page 3.

Nkurikiyimfura, I. et al. Heat transfer enhancement by magnetic nanofluids—a review. *Renewable and Sustainable Energy Reviews*, Elsevier, v. 21, p. 548–561, 2013. Quoted on page 4.

Nogueira, H. P. et al. Efficient Cr (VI) removal from wastewater by activated carbon superparamagnetic composites. *Microchemical Journal*, Elsevier, v. 149, p. 104025, 2019. Quoted on page 4.

Odenbach, S. *Colloidal magnetic fluids: basics, development and application of ferrofluids.* : Springer, 2009. v. 763. Quoted 2 times on pages 1 and 10.

Ohno, K.-i. et al. Analysis of liquid sloshing of a tuned magnetic fluid damper for single and co-axial cylindrical containers. *Journal of Magnetism and Magnetic Materials*, Elsevier, v. 323, n. 10, p. 1389–1393, 2011. Quoted on page 4.

Okamoto, H.; Fujii, H. *Nonlinear Dynamics, Iwanami Lectures of Applied Mathematics (in Japanese) Iwanami.* : Tokyo, 1995. Quoted on page 81.

Papell, S. Low viscosity magnetic fluid obtained by the colloidal suspension of magnetic particles patent. 1965. Quoted on page 2.

Peiravi, M. et al. Magnetic hyperthermia: Potentials and limitations. *Journal of the Indian Chemical Society*, Elsevier, v. 99, n. 1, p. 100269, 2022. Quoted on page 1.

Pérez, L. et al. Thermal convection thresholds in a oldroyd magnetic fluid. *Journal of Magnetism and Magnetic Materials*, Elsevier, v. 323, n. 6, p. 691–698, 2011. Quoted on page 4.

Périgo, E. A. et al. Fundamentals and advances in magnetic hyperthermia. *Applied Physics Reviews*, AIP Publishing LLC, v. 2, n. 4, p. 041302, 2015. Quoted on page 1.

Poland, D. *Statistical Mechanics (McQuarrie, Donald A.).* : ACS Publications, 1977. Quoted on page 15.

Polyak, B.; Friedman, G. Magnetic targeting for site-specific drug delivery: applications and clinical potential. *Expert opinion on drug delivery*, Taylor & Francis, v. 6, n. 1, p. 53–70, 2009. Quoted on page 3.

Rosensweig, R. E. Heating magnetic fluid with alternating magnetic field. *J. M. M. M.*, Elsevier, v. 252, p. 370–374, 2002. Quoted 3 times on pages 1, 21, and 22.

Rosensweig, R. E. *Ferrohydrodynamics.* : Courier Corporation, 2013. Quoted on page 10.

ROURE NETO, G. A. *Macroscopic quantities of dilute non-brownian: magnetic suspensions in a shear flow.* 2018. Dissertação (Mestrado) — Departamento de Engenharia Mecânica, Universidade de Brasília, Brasília, DF, Publicação DM-280, 138p. Quoted on page 2.

Sadhukha, T. et al. Inhalable magnetic nanoparticles for targeted hyperthermia in lung cancer therapy. *Biomaterials*, Elsevier, v. 34, n. 21, p. 5163–5171, 2013. Quoted on page 3.

Scherer, C.; Neto, A. M. F. Ferrofluids: properties and applications. *Brazilian journal of physics*, SciELO Brasil, v. 35, n. 3A, p. 718–727, 2005. Quoted on page 4.

Seydel, R. *Practical bifurcation and stability analysis.* : Springer Science & Business Media, 2009. v. 5. Quoted 2 times on pages 34 and 35.

Sezer, N. et al. Superparamagnetic nanoarchitectures: Multimodal functionalities and applications. *Journal of Magnetism and Magnetic Materials*, Elsevier, p. 168300, 2021. Quoted 2 times on pages 2 and 3.

Shin, K.; Hammond, J. *Fundamentals of signal processing for sound and vibration engineers.* : John Wiley & Sons, 2008. Quoted 2 times on pages 36 and 38.

Silva, A. C. d. et al. Magnetohyperthermia for treatment of gliomas: experimental and clinical studies. *Einstein (São Paulo)*, SciELO Brasil, v. 8, p. 361–367, 2010. Quoted on page 3.

Stratton, J. A. *Electromagnetic theory.* : John Wiley & Sons, 2007. v. 33. Quoted on page 20.

Tang, Y.-d. et al. Effect of mass transfer and diffusion of nanofluid on the thermal ablation of malignant cells during magnetic hyperthermia. *Applied Mathematical Modelling*, Elsevier, v. 83, p. 122–135, 2020. Quoted on page 1.

Thiesen, B.; Jordan, A. Clinical applications of magnetic nanoparticles for hyperthermia. *International journal of hyperthermia*, Taylor & Francis, v. 24, n. 6, p. 467–474, 2008. Quoted on page 1.

Wang, S. et al. A ferrofluid-based planar damper with magnetic spring. *Journal of Magnetics*, v. 23, n. 3, p. 405–408, 2018. Quoted on page 4.

Wang, Z.-Y. et al. Nanosized As_2O_3/Fe_2O_3 complexes combined with magnetic fluid hyperthermia selectively target liver cancer cells. *World journal of gastroenterology: WJG*, Baishideng Publishing Group Inc, v. 15, n. 24, p. 2995, 2009. Quoted on page 3.

Wiggins, S. et al. *Introduction to applied nonlinear dynamical systems and chaos.* : Springer, 2003. v. 2. Quoted on page 34.

Zhu, S. et al. Low-frequency vibration control of floating slab tracks using dynamic vibration absorbers. *Vehicle System Dynamics*, Taylor & Francis, v. 53, n. 9, p. 1296–1314, 2015. Quoted on page 4.

Appendix

A Proof of the Dimensionless Governing Equations

In this chapter, the demonstration of the dimensionless governing equation, obtained from Newton's second law, is shown. The nondimensionalization variables chosen are shown at Eq. (A.1),

$$t^* = \frac{tU_s}{a}, \quad \mathbf{u}_i^* = \frac{\mathbf{u}_i}{U_s}, \quad \boldsymbol{\omega}_i^* = \frac{\boldsymbol{\omega}_i a}{U_s} \quad \text{and} \quad \mathbf{g}^* = \frac{\mathbf{g}}{g}. \tag{A.1}$$

A.1 Translation Governing Equation

The translational governing equation is

$$\mathcal{M}\frac{\mathrm{d}\mathbf{u}_i}{\mathrm{d}t} = -6\pi\eta a\mathbf{u}_i + \frac{4}{3}\pi a^3 \Delta\rho\mathbf{g} + \mathbf{F}_{\mathbf{B}i} + \mathbf{F}_{\mathbf{m}i} + \mathbf{F}_{\mathbf{r}i} + \mathbf{F}_{\mathbf{c}i}, \tag{A.2}$$

Applying Eq. (A.1) into Eqs. (A.2) yields Eq.(A.3),

$$\left(\frac{\mathcal{M}U_s}{a}\right)\frac{\mathrm{d}}{\mathrm{d}t^*}\left(U_s\mathbf{u}_i^*\right) = -6\pi\eta aU_s\mathbf{u}_i^* + \left(\frac{4}{3}\pi a^3 \Delta\rho g\right)\mathbf{g}^* + \mathbf{F}_{\mathbf{B}i} + \mathbf{F}_{\mathbf{m}i} + \mathbf{F}_{\mathbf{r}i} + \mathbf{F}_{\mathbf{c}i}, \tag{A.3}$$

Dividing Eq. (A.3) by $6\pi\eta aU_s$, one obtain

$$\left(\frac{\mathcal{M}U_s^2}{6\pi\eta a^2 U_s}\right)\frac{\mathrm{d}\mathbf{u}_i^*}{\mathrm{d}t^*} = -\mathbf{u}_i^* + \left(\frac{4\pi a^3 \Delta\rho g}{18\pi\eta aU_s}\right)\mathbf{g}^* + \frac{1}{6\pi\eta aU_s}\left(\mathbf{F}_{\mathbf{B}i} + \mathbf{F}_{\mathbf{m}i} + \mathbf{F}_{\mathbf{r}i} + \mathbf{F}_{\mathbf{c}i}\right)$$

$$\implies \left(\frac{\mathcal{M}U_s}{6\pi\eta a^2}\right)\frac{\mathrm{d}\mathbf{u}_i^*}{\mathrm{d}t^*} = -\mathbf{u}_i^* + \left(\frac{2a^2 \Delta\rho g}{9\eta U_s}\right)\mathbf{g}^* + \frac{1}{6\pi\eta aU_s}\left(\mathbf{F}_{\mathbf{B}i} + \mathbf{F}_{\mathbf{m}i} + \mathbf{F}_{\mathbf{r}i} + \mathbf{F}_{\mathbf{c}i}\right)$$

$$\implies \left(\frac{\mathcal{M}U_s}{6\pi\eta a^2}\right)\frac{\mathrm{d}\mathbf{u}_i^*}{\mathrm{d}t^*} = -\mathbf{u}_i^* + \left(\frac{U_s}{U_s}\right)\mathbf{g}^* + \frac{1}{6\pi\eta aU_s}\left(\mathbf{F}_{\mathbf{B}i} + \mathbf{F}_{\mathbf{m}i} + \mathbf{F}_{\mathbf{r}i} + \mathbf{F}_{\mathbf{c}i}\right), \tag{A.4}$$

Let $\text{St} = \dfrac{\mathcal{M}U_s}{6\pi\eta a^2}$ be the translational Stokes number and the forces $\mathbf{F}_{\mathbf{B}i}^{*} = \dfrac{\mathbf{F}_{\mathbf{B}i}}{6\pi\eta a U_s}$, $\mathbf{F}_{\mathbf{m}i}^{*} = \dfrac{\mathbf{F}_{\mathbf{m}i}}{6\pi\eta a U_s}$, $\mathbf{F}_{\mathbf{r}i}^{*} = \dfrac{\mathbf{F}_{\mathbf{r}i}}{6\pi\eta a U_s}$ and $\mathbf{F}_{\mathbf{c}i}^{*} = \dfrac{\mathbf{F}_{\mathbf{c}i}}{6\pi\eta a U_s}$ the dimensionless forces. Thus, the dimensionless form of the translational equation is

$$\text{St}\,\frac{\mathrm{d}\mathbf{u}_i^{*}}{\mathrm{d}t^{*}} = -\mathbf{u}_i^{*} + \mathbf{g}^{*} + \mathbf{F}_{\mathbf{B}i}^{*} + \mathbf{F}_{\mathbf{m}i}^{*} + \mathbf{F}_{\mathbf{r}i}^{*} + \mathbf{F}_{\mathbf{c}i}^{*}, \tag{A.5}$$

A.1.1   Dimensionless Brownian Force

The brownian force is given by

$$\mathbf{F}_{\mathbf{B}i} = 6\pi\eta a \left(6\frac{\mathcal{D}_t}{\delta\tau}\right)^{1/2} \boldsymbol{\xi} \tag{A.6}$$

In this way, the dimensionless brownian force is

$$\mathbf{F}_{\mathbf{B}i}^{*} = \frac{\mathbf{F}_{\mathbf{B}i}}{6\pi\eta a U_s} = \frac{1}{6\pi\eta a U_s}\left[6\pi\eta a \left(6\frac{\mathcal{D}_t}{\delta\tau}\right)^{1/2} \boldsymbol{\xi}\right] = \frac{1}{U_s}\left(6\frac{\mathcal{D}_t}{\delta\tau}\right)^{1/2} \boldsymbol{\xi}$$
$$= \left(6\frac{\mathcal{D}_t}{U_s^2\delta\tau}\right)^{1/2} \boldsymbol{\xi} \tag{A.7}$$

By Eq. (A.1), the dimensionless time step, $\delta\tau^{*}$, is defined by

$$\delta\tau^{*} = \frac{\delta\tau U_s}{a} \tag{A.8}$$

Applying Eq. (A.8) into (A.7) results in

$$\mathbf{F}_{\mathbf{B}i}^{*} = \left(6\frac{\mathcal{D}_t}{U_s^2 a\delta\tau^{*}/U_s}\right)^{1/2} \boldsymbol{\xi} = \left(6\frac{\mathcal{D}_t}{U_s a\delta\tau^{*}}\right)^{1/2} \boldsymbol{\xi} = \left(\frac{6}{\frac{U_s a}{\mathcal{D}_t}\delta\tau^{*}}\right)^{1/2} \boldsymbol{\xi} \tag{A.9}$$

Let $\text{Pe} = \dfrac{U_s a}{\mathcal{D}_t}$ be the translational Peclet number. Thus,

$$\mathbf{F}_{\mathbf{B}i}^{*} = \left(\frac{6}{\text{Pe }\delta\tau^{*}}\right)^{1/2} \boldsymbol{\xi} \tag{A.10}$$

A.1.2   Dimensionless Magnetic Force

The magnetic force is given by

$$
\mathbf{F}_{\mathbf{m}i} = \left\{ \frac{3\mu_0 m^2}{4\pi} \sum_{\substack{j=1 \\ j \neq i}}^{N} \frac{1}{r_{ij}^4} \left[\left(\hat{\mathbf{d}}_i \cdot \hat{\mathbf{d}}_j \right) \hat{\mathbf{r}}_{ij} + \left(\hat{\mathbf{d}}_i \cdot \hat{\mathbf{r}}_{ij} \right) \hat{\mathbf{d}}_j + \left(\hat{\mathbf{d}}_j \cdot \hat{\mathbf{r}}_{ij} \right) \hat{\mathbf{d}}_i + \right.\right.
$$
$$
\left.\left. - 5 \left(\hat{\mathbf{d}}_i \cdot \hat{\mathbf{r}}_{ij} \right) \left(\hat{\mathbf{d}}_j \cdot \hat{\mathbf{r}}_{ij} \right) \hat{\mathbf{r}}_{ij} \right] \right\} + \mu_0 m H \left(\hat{\mathbf{d}}_i \cdot \nabla \hat{\mathbf{H}} \right), \quad \text{(A.11)}
$$

So, the dimensionless magnetic force is

$$
\mathbf{F}_{\mathbf{m}i}^* = \frac{\mathbf{F}_{\mathbf{m}i}}{6\pi \eta a U_s}
$$
$$
= \frac{1}{6\pi \eta a U_s} \left\{ \left[\frac{3\mu_0 m^2}{4\pi} \sum_{\substack{j=1 \\ j \neq i}}^{N} \frac{1}{r_{ij}^4} \left[\left(\hat{\mathbf{d}}_i \cdot \hat{\mathbf{d}}_j \right) \hat{\mathbf{r}}_{ij} + \left(\hat{\mathbf{d}}_i \cdot \hat{\mathbf{r}}_{ij} \right) \hat{\mathbf{d}}_j + \left(\hat{\mathbf{d}}_j \cdot \hat{\mathbf{r}}_{ij} \right) \hat{\mathbf{d}}_i + \right.\right.\right.
$$
$$
\left.\left.\left. - 5 \left(\hat{\mathbf{d}}_i \cdot \hat{\mathbf{r}}_{ij} \right) \left(\hat{\mathbf{d}}_j \cdot \hat{\mathbf{r}}_{ij} \right) \hat{\mathbf{r}}_{ij} \right] \right] + \mu_0 m H \left(\hat{\mathbf{d}}_i \cdot \nabla \hat{\mathbf{H}} \right) \right\} \quad \text{(A.12)}
$$

Multiply and divide Eq. (A.12) by $K_b T$,

$$
\mathbf{F}_{\mathbf{m}i}^* = \frac{K_b T}{6\pi \eta a U_s} \left\{ \left[\frac{3\mu_0 m^2}{4\pi K_b T} \sum_{\substack{j=1 \\ j \neq i}}^{N} \frac{1}{r_{ij}^4} \left[\left(\hat{\mathbf{d}}_i \cdot \hat{\mathbf{d}}_j \right) \hat{\mathbf{r}}_{ij} + \left(\hat{\mathbf{d}}_i \cdot \hat{\mathbf{r}}_{ij} \right) \hat{\mathbf{d}}_j + \left(\hat{\mathbf{d}}_j \cdot \hat{\mathbf{r}}_{ij} \right) \hat{\mathbf{d}}_i + \right.\right.\right.
$$
$$
\left.\left.\left. - 5 \left(\hat{\mathbf{d}}_i \cdot \hat{\mathbf{r}}_{ij} \right) \left(\hat{\mathbf{d}}_j \cdot \hat{\mathbf{r}}_{ij} \right) \hat{\mathbf{r}}_{ij} \right] \right] + \left(\mu_0 m H \right) K_b T \left(\hat{\mathbf{d}}_i \cdot \nabla \hat{\mathbf{H}} \right) \right\} \quad \text{(A.13)}
$$

Since $\mathcal{D}_t = \dfrac{K_b T}{6\pi \eta a}$, one obtain

$$
\mathbf{F}_{\mathbf{m}i}^* = \left(\frac{\mathcal{D}_t}{U_s} \right) \left\{ \left[\frac{3\mu_0 m^2}{4\pi K_b T} \sum_{\substack{j=1 \\ j \neq i}}^{N} \frac{1}{r_{ij}^4} \left[\left(\hat{\mathbf{d}}_i \cdot \hat{\mathbf{d}}_j \right) \hat{\mathbf{r}}_{ij} + \left(\hat{\mathbf{d}}_i \cdot \hat{\mathbf{r}}_{ij} \right) \hat{\mathbf{d}}_j + \left(\hat{\mathbf{d}}_j \cdot \hat{\mathbf{r}}_{ij} \right) \hat{\mathbf{d}}_i + \right.\right.\right.
$$
$$
\left.\left.\left. - 5 \left(\hat{\mathbf{d}}_i \cdot \hat{\mathbf{r}}_{ij} \right) \left(\hat{\mathbf{d}}_j \cdot \hat{\mathbf{r}}_{ij} \right) \hat{\mathbf{r}}_{ij} \right] \right] + \left(\frac{\mu_0 m H}{K_b T} \right) \left(\hat{\mathbf{d}}_i \cdot \nabla \hat{\mathbf{H}} \right) \right\} \quad \text{(A.14)}
$$

Next, the dimensionless forms of r_{ij} and ∇ are given. The distance between particles, r_{ij}, has unit of m, such that its dimensionless form is

$$
r_{ij}^* = \frac{r_{ij}}{a} \implies r_{ij} = a r_{ij}^* \quad \text{(A.15)}
$$

in which r_{ij}^* is the dimensionless distance between particles.

The gradient operator, ∇, has unit of m^{-1}. In this way, its dimensionless form is

$$\nabla^* = a\nabla \implies \nabla = \frac{\nabla^*}{a} \tag{A.16}$$

The substitution of Eqs. (A.15) and (A.16) into (A.14) produces

$$\mathbf{F_{m}}_i^* = \left(\frac{\mathcal{D}_t}{U_s}\right) \left\{ \left[\frac{3\mu_0 m^2}{4\pi K_b T} \sum_{\substack{j=1 \\ j\neq i}}^{N} \frac{1}{\left(ar_{ij}^*\right)^4} \left[\left(\hat{\mathbf{d}}_i \cdot \hat{\mathbf{d}}_j\right) \hat{\mathbf{r}}_{ij} + \left(\hat{\mathbf{d}}_i \cdot \hat{\mathbf{r}}_{ij}\right) \hat{\mathbf{d}}_j + \left(\hat{\mathbf{d}}_j \cdot \hat{\mathbf{r}}_{ij}\right) \hat{\mathbf{d}}_i + \right. \right. $$
$$\left. \left. - 5\left(\hat{\mathbf{d}}_i \cdot \hat{\mathbf{r}}_{ij}\right)\left(\hat{\mathbf{d}}_j \cdot \hat{\mathbf{r}}_{ij}\right) \hat{\mathbf{r}}_{ij} \right] \right] + \left(\frac{\mu_0 mH}{K_b T}\right) \left(\hat{\mathbf{d}}_i \cdot \frac{\nabla^*}{a}\hat{\mathbf{H}}\right) \right\} \tag{A.17}$$

Factoring a,

$$\implies \mathbf{F_{m}}_i^* = \left(\frac{\mathcal{D}_t}{U_s a}\right) \left\{ \left[\frac{3\mu_0 m^2}{4\pi K_b T a^3} \sum_{\substack{j=1 \\ j\neq i}}^{N} \frac{1}{r_{ij}^{*\,4}} \left[\left(\hat{\mathbf{d}}_i \cdot \hat{\mathbf{d}}_j\right) \hat{\mathbf{r}}_{ij} + \left(\hat{\mathbf{d}}_i \cdot \hat{\mathbf{r}}_{ij}\right) \hat{\mathbf{d}}_j + \left(\hat{\mathbf{d}}_j \cdot \hat{\mathbf{r}}_{ij}\right) \hat{\mathbf{d}}_i + \right. \right. $$
$$\left. \left. - 5\left(\hat{\mathbf{d}}_i \cdot \hat{\mathbf{r}}_{ij}\right)\left(\hat{\mathbf{d}}_j \cdot \hat{\mathbf{r}}_{ij}\right) \hat{\mathbf{r}}_{ij} \right] \right] + \left(\frac{\mu_0 mH}{K_b T}\right) \left(\hat{\mathbf{d}}_i \cdot \nabla^*\hat{\mathbf{H}}\right) \right\} \tag{A.18}$$

Applying $\text{Pe} = \dfrac{U_s a}{\mathcal{D}_t}$,

$$\mathbf{F_{m}}_i^* = \frac{1}{\text{Pe}} \left\{ \left[\frac{3\mu_0 m^2}{4\pi K_b T a^3} \sum_{\substack{j=1 \\ j\neq i}}^{N} \frac{1}{r_{ij}^{*\,4}} \left[\left(\hat{\mathbf{d}}_i \cdot \hat{\mathbf{d}}_j\right) \hat{\mathbf{r}}_{ij} + \left(\hat{\mathbf{d}}_i \cdot \hat{\mathbf{r}}_{ij}\right) \hat{\mathbf{d}}_j + \left(\hat{\mathbf{d}}_j \cdot \hat{\mathbf{r}}_{ij}\right) \hat{\mathbf{d}}_i + \right. \right. $$
$$\left. \left. - 5\left(\hat{\mathbf{d}}_i \cdot \hat{\mathbf{r}}_{ij}\right)\left(\hat{\mathbf{d}}_j \cdot \hat{\mathbf{r}}_{ij}\right) \hat{\mathbf{r}}_{ij} \right] \right] + \left(\frac{\mu_0 mH}{K_b T}\right) \left(\hat{\mathbf{d}}_i \cdot \nabla^*\hat{\mathbf{H}}\right) \right\} \tag{A.19}$$

$$\implies \mathbf{F_{m}}_i^* = \frac{1}{\text{Pe}} \left\{ \left[\frac{24\mu_0 m^2}{4\pi K_b T \left(8a^3\right)} \sum_{\substack{j=1 \\ j\neq i}}^{N} \frac{1}{r_{ij}^{*\,4}} \left[\left(\hat{\mathbf{d}}_i \cdot \hat{\mathbf{d}}_j\right) \hat{\mathbf{r}}_{ij} + \left(\hat{\mathbf{d}}_i \cdot \hat{\mathbf{r}}_{ij}\right) \hat{\mathbf{d}}_j + \left(\hat{\mathbf{d}}_j \cdot \hat{\mathbf{r}}_{ij}\right) \hat{\mathbf{d}}_i + \right. \right. $$
$$\left. \left. - 5\left(\hat{\mathbf{d}}_i \cdot \hat{\mathbf{r}}_{ij}\right)\left(\hat{\mathbf{d}}_j \cdot \hat{\mathbf{r}}_{ij}\right) \hat{\mathbf{r}}_{ij} \right] \right] + \left(\frac{\mu_0 mH}{K_b T}\right) \left(\hat{\mathbf{d}}_i \cdot \nabla^*\hat{\mathbf{H}}\right) \right\} \tag{A.20}$$

$$\implies \mathbf{F_{m}}_i^* = \frac{1}{\text{Pe}} \left\{ \left[24 \left(\frac{\mu_0 m^2}{4\pi K_b T \left(2a\right)^3}\right) \sum_{\substack{j=1 \\ j\neq i}}^{N} \frac{1}{r_{ij}^{*\,4}} \left[\left(\hat{\mathbf{d}}_i \cdot \hat{\mathbf{d}}_j\right) \hat{\mathbf{r}}_{ij} + \left(\hat{\mathbf{d}}_i \cdot \hat{\mathbf{r}}_{ij}\right) \hat{\mathbf{d}}_j + \left(\hat{\mathbf{d}}_j \cdot \hat{\mathbf{r}}_{ij}\right) \hat{\mathbf{d}}_i + \right. \right. $$
$$\left. \left. - 5\left(\hat{\mathbf{d}}_i \cdot \hat{\mathbf{r}}_{ij}\right)\left(\hat{\mathbf{d}}_j \cdot \hat{\mathbf{r}}_{ij}\right) \hat{\mathbf{r}}_{ij} \right] \right] + \left(\frac{\mu_0 mH}{K_b T}\right) \left(\hat{\mathbf{d}}_i \cdot \nabla^*\hat{\mathbf{H}}\right) \right\} \tag{A.21}$$

Define $\alpha = \dfrac{\mu_0 mH}{K_b T}$ as the Langevin parameter and $\lambda = \dfrac{\mu_0 m^2}{4\pi K_b T \left(2a\right)^3}$ as the dipolar interaction parameter.

$$\mathbf{F}_{\mathbf{m}i}^* = \frac{1}{\mathrm{Pe}} \left\{ \left[24\left(\lambda\right) \sum_{\substack{j=1 \\ j \neq i}}^{N} \frac{1}{r_{ij}^{*\,4}} \left[\left(\hat{\mathbf{d}}_i \cdot \hat{\mathbf{d}}_j\right) \hat{\mathbf{r}}_{ij} + \left(\hat{\mathbf{d}}_i \cdot \hat{\mathbf{r}}_{ij}\right) \hat{\mathbf{d}}_j + \left(\hat{\mathbf{d}}_j \cdot \hat{\mathbf{r}}_{ij}\right) \hat{\mathbf{d}}_i + \right.\right.$$
$$\left.\left. - 5 \left(\hat{\mathbf{d}}_i \cdot \hat{\mathbf{r}}_{ij}\right) \left(\hat{\mathbf{d}}_j \cdot \hat{\mathbf{r}}_{ij}\right) \hat{\mathbf{r}}_{ij} \right] \right] + \left(\alpha\right) \left(\hat{\mathbf{d}}_i \cdot \nabla^* \hat{\mathbf{H}}\right) \right\} \quad \text{(A.22)}$$

$$\implies \mathbf{F}_{\mathbf{m}i}^* = \frac{24\lambda}{\mathrm{Pe}} \left\{ \sum_{\substack{j=1 \\ j \neq i}}^{N} \frac{1}{r_{ij}^{*\,4}} \left[\left(\hat{\mathbf{d}}_i \cdot \hat{\mathbf{d}}_j\right) \hat{\mathbf{r}}_{ij} + \left(\hat{\mathbf{d}}_i \cdot \hat{\mathbf{r}}_{ij}\right) \hat{\mathbf{d}}_j + \left(\hat{\mathbf{d}}_j \cdot \hat{\mathbf{r}}_{ij}\right) \hat{\mathbf{d}}_i + \right.\right.$$
$$\left.\left. - 5 \left(\hat{\mathbf{d}}_i \cdot \hat{\mathbf{r}}_{ij}\right) \left(\hat{\mathbf{d}}_j \cdot \hat{\mathbf{r}}_{ij}\right) \hat{\mathbf{r}}_{ij} \right] \right\} + \frac{\alpha}{\mathrm{Pe}} \left(\hat{\mathbf{d}}_i \cdot \nabla^* \hat{\mathbf{H}}\right) \quad \text{(A.23)}$$

Considering that $\hat{\mathbf{H}} = \hat{\mathbf{H}}(t)$, that is, the dimensionless external magnetic field only depends on the time and not on the position, $\nabla^* \hat{\mathbf{H}} = \mathbf{0}$, where $\mathbf{0}$ is the zero second order tensor. As a consequence,

$$\implies \mathbf{F}_{\mathbf{m}i}^* = \frac{24\lambda}{\mathrm{Pe}} \left\{ \sum_{\substack{j=1 \\ j \neq i}}^{N} \frac{1}{r_{ij}^{*\,4}} \left[\left(\hat{\mathbf{d}}_i \cdot \hat{\mathbf{d}}_j\right) \hat{\mathbf{r}}_{ij} + \left(\hat{\mathbf{d}}_i \cdot \hat{\mathbf{r}}_{ij}\right) \hat{\mathbf{d}}_j + \left(\hat{\mathbf{d}}_j \cdot \hat{\mathbf{r}}_{ij}\right) \hat{\mathbf{d}}_i + \right.\right.$$
$$\left.\left. - 5 \left(\hat{\mathbf{d}}_i \cdot \hat{\mathbf{r}}_{ij}\right) \left(\hat{\mathbf{d}}_j \cdot \hat{\mathbf{r}}_{ij}\right) \hat{\mathbf{r}}_{ij} \right] \right\} \quad \text{(A.24)}$$

A.1.3 Dimensionless Repulsive Force

The repulsive force is

$$\mathbf{F}_{\mathbf{r}i} = C_1 \left(6\pi\eta a\right) u_i \exp\left(-\frac{\epsilon_{ij}}{C_2}\right) \hat{\mathbf{r}}_{ij}. \quad \text{(A.25)}$$

Thus, the dimensionless repulsive force is

$$\mathbf{F}_{\mathbf{r}i}^* = \frac{\mathbf{F}_{\mathbf{r}i}}{6\pi\eta a U_s} = C_1 \left(\frac{u_i}{U_s}\right) \exp\left(-\frac{\epsilon_{ij}}{C_2}\right) \hat{\mathbf{r}}_{ij} \quad \text{(A.26)}$$

Since the dimensionless velocity magnitude is $u_i^* = \dfrac{u_i}{U_s}$, one obtain

$$\mathbf{F_r}_i^* = C_1 u_i^* \exp\left(-\frac{\epsilon_{ij}}{C_2}\right) \hat{\mathbf{r}}_{ij} \tag{A.27}$$

in which $u_i^* = \|\mathbf{u}_i^*\|$.

Define the dimensionless quantity ϵ_{ij}^*,

$$\epsilon_{ij}^* = \frac{\epsilon_{ij}}{a} = \left|\frac{r_{ij}}{a} - 2\right| \implies \epsilon_{ij} = a\epsilon_{ij}^*, \tag{A.28}$$

in this way, by the substitution of Eq.(A.28) into (A.27),

$$\mathbf{F_r}_i^* = C_1 u_i^* \exp\left(-\frac{a\epsilon_{ij}^*}{C_2}\right) \hat{\mathbf{r}}_{ij} = C_1 u_i^* \exp\left(-\frac{\epsilon_{ij}^*}{C_2/a}\right) \hat{\mathbf{r}}_{ij} \tag{A.29}$$

Let $C_2^* = \dfrac{C_2}{a}$ be the dimensionless calibration constant of the repulsive force for the range of the field. So,

$$\mathbf{F_r}_i^* = C_1 u_i^* \exp\left(-\frac{\epsilon_{ij}^*}{C_2^*}\right) \hat{\mathbf{r}}_{ij} \tag{A.30}$$

A.1.4   Dimensionless Contact Force

The contact force is

$$\mathbf{F_c}_i = C_3 \varepsilon b^{1/2} \epsilon_{ij}^{3/2}\ \hat{\mathbf{r}}_{ij}. \tag{A.31}$$

$$\epsilon_{ij} = |r_{ij} - 2a| \tag{A.32}$$

$$b = \frac{a}{2} \tag{A.33}$$

So, the dimensionless contact force is

$$\mathbf{F_c}_i^* = \frac{\mathbf{F_c}_i}{6\pi\eta a U_s} = \frac{C_3 \varepsilon b^{1/2}}{6\pi\eta a U_s}\epsilon_{ij}^{3/2}\ \hat{\mathbf{r}}_{ij}. \tag{A.34}$$

Using the dimensionless quantity $\epsilon_{ij}^* = \epsilon_{ij}/a$ and applying the formula for monodisperse suspensions $b = a/2$,

$$\mathbf{F_c}_i^* = \frac{C_3 \varepsilon}{6\pi\eta a U_s}\left(\frac{a}{2}\right)^{1/2}\left(a\epsilon_{ij}^*\right)^{3/2}\ \hat{\mathbf{r}}_{ij} = \left(\frac{C_3}{\sqrt{2}}\right)\frac{\varepsilon}{6\pi\eta a U_s}\left(a^{1/2}a^{3/2}\right)\epsilon_{ij}^{*\,3/2}\ \hat{\mathbf{r}}_{ij}. \tag{A.35}$$

Let $C_4 = \dfrac{C_3}{\sqrt{2}}$ be the calibration constant for the dimensionless contact force. Thus,

$$\mathbf{F_{c}}_i^* = C_4 \frac{\varepsilon a^2}{6\pi\eta a U_s} \epsilon_{ij}^{*\,3/2}\, \hat{\mathbf{r}}_{ij}. \tag{A.36}$$

Let $P_c = \dfrac{C_4 \varepsilon a^2}{6\pi\eta a U_s}$ be the dimensionless contact parameter that quantify the relation between the contact force and hydrodynamic drag force. So,

$$\mathbf{F_{c}}_i^* = P_c \epsilon_{ij}^{*\,3/2}\, \hat{\mathbf{r}}_{ij}. \tag{A.37}$$

The value $P_c = 100$ has been adopted for all simulations.

A.2 Rotational Governing Equation

The rotational governing equation is

$$\mathcal{I}\frac{\mathrm{d}\boldsymbol{\omega}_i}{\mathrm{d}t} = -8\pi\eta a^3 \boldsymbol{\omega}_i + \mathbf{T_{B}}_i + \mathbf{T_{m}}_i \tag{A.38}$$

The substitution of Eq. (A.1) into (A.38) yields

$$\left(\frac{\mathcal{I}U_s}{a}\right)\frac{\mathrm{d}}{\mathrm{d}t^*}\left(\frac{U_s}{a}\boldsymbol{\omega}_i^*\right) = -\left(\frac{8\pi\eta a^3 U_s}{a}\right)\boldsymbol{\omega}_i^* + \mathbf{T_{B}}_i + \mathbf{T_{m}}_i \tag{A.39}$$

Divide Eq. (A.39) by $8\pi\eta a^2 U_s$,

$$\left(\frac{\mathcal{I}U_s}{8\pi\eta a^3 U_s}\right)\frac{\mathrm{d}}{\mathrm{d}t^*}\left(\frac{U_s}{a}\boldsymbol{\omega}_i^*\right) = -\boldsymbol{\omega}_i^* + \frac{1}{8\pi\eta a^2 U_s}\left(\mathbf{T_{B}}_i + \mathbf{T_{m}}_i\right) \tag{A.40}$$

$$\implies \left(\frac{\mathcal{I}U_s}{8\pi\eta a^4}\right)\frac{\mathrm{d}\boldsymbol{\omega}_i^*}{\mathrm{d}t^*} = -\boldsymbol{\omega}_i^* + \frac{1}{8\pi\eta a^2 U_s}\left(\mathbf{T_{B}}_i + \mathbf{T_{m}}_i\right) \tag{A.41}$$

Let $\mathrm{St}_r = \dfrac{\mathcal{I}U_s}{8\pi\eta a^4}$ be the rotational Stokes number and the torques $\mathbf{T_{B}}_i^* = \dfrac{\mathbf{T_{B}}_i}{8\pi\eta a^2 U_s}$ and $\mathbf{T_{m}}_i^* = \dfrac{\mathbf{T_{m}}_i}{8\pi\eta a^2 U_s}$ the dimensionless torques. Thus, the dimensionless rotational equation is

$$\mathrm{St}_r \frac{\mathrm{d}\boldsymbol{\omega}_i^*}{\mathrm{d}t^*} = -\boldsymbol{\omega}_i^* + \mathbf{T_{B}}_i^* + \mathbf{T_{m}}_i^*. \tag{A.42}$$

A.2.1 Dimensionless Brownian Torque

The brownian torque is given by

$$\mathbf{T}_{\mathbf{B}i} = 8\pi\eta a^3 \left(6\frac{\mathcal{D}_r}{\delta\tau}\right)^{1/2} \boldsymbol{\xi} \tag{A.43}$$

So, the dimensionless brownian torque is

$$\mathbf{T}_{\mathbf{B}i}^* = \frac{\mathbf{T}_{\mathbf{B}i}}{8\pi\eta a^2 U_s} = \frac{1}{8\pi\eta a^2 U_s}\left[8\pi\eta a^3 \left(6\frac{\mathcal{D}_r}{\delta\tau}\right)^{1/2}\boldsymbol{\xi}\right] = \frac{a}{U_s}\left(6\frac{\mathcal{D}_r}{\delta\tau}\right)^{1/2}\boldsymbol{\xi} \tag{A.44}$$

$$= \left(6\frac{a^2\mathcal{D}_r}{U_s^2\delta\tau}\right)^{1/2}\boldsymbol{\xi} \tag{A.45}$$

By the substitution of Eq. (A.8) in (A.45),

$$\mathbf{T}_{\mathbf{B}i}^* = \left(6\frac{a^2\mathcal{D}_r}{U_s^2 a\delta\tau^*/U_s}\right)^{1/2}\boldsymbol{\xi} = \left(6\frac{a\mathcal{D}_r}{U_s\delta\tau^*}\right)^{1/2}\boldsymbol{\xi} = \left(\frac{6}{\frac{U_s}{a\mathcal{D}_r}\delta\tau^*}\right)^{1/2}\boldsymbol{\xi} \tag{A.46}$$

Let $\mathrm{Pe}_r = \dfrac{U_s}{a\mathcal{D}_r}$ be the rotational Peclet number. Thus,

$$\mathbf{T}_{\mathbf{B}i}^* = \left(\frac{6}{\mathrm{Pe}_r\ \delta\tau^*}\right)^{1/2}\boldsymbol{\xi} \tag{A.47}$$

A.2.2 Dimensionless Magnetic Torque

The magnetic torque is given by

$$\mathbf{T}_{\mathbf{m}i} = \left\{\frac{3\mu_0 m^2}{4\pi}\sum_{\substack{j=1\\j\neq i}}^{N}\frac{1}{r_{ij}^3}\left[-\frac{1}{3}\left(\hat{\mathbf{d}}_i\times\hat{\mathbf{d}}_j\right) + \left(\hat{\mathbf{d}}_j\cdot\hat{\mathbf{r}}_{ij}\right)\left(\hat{\mathbf{d}}_i\times\hat{\mathbf{r}}_{ij}\right)\right]\right\} + \mu_0 mH\hat{\mathbf{d}}_i\times\hat{\mathbf{H}}. \tag{A.48}$$

Thus, the dimensionless magnetic torque is

$$\mathbf{T}_{\mathbf{m}i}^* = \frac{\mathbf{T}_{\mathbf{m}i}}{8\pi\eta a^2 U_s}$$

$$= \frac{1}{8\pi\eta a^2 U_s}\left\{\left[\frac{3\mu_0 m^2}{4\pi}\sum_{\substack{j=1\\j\neq i}}^{N}\frac{1}{r_{ij}^3}\left[-\frac{1}{3}\left(\hat{\mathbf{d}}_i\times\hat{\mathbf{d}}_j\right) + \left(\hat{\mathbf{d}}_j\cdot\hat{\mathbf{r}}_{ij}\right)\left(\hat{\mathbf{d}}_i\times\hat{\mathbf{r}}_{ij}\right)\right]\right] + \right.$$

$$\left. + \mu_0 mH\hat{\mathbf{d}}_i\times\hat{\mathbf{H}}\right\} \tag{A.49}$$

Multiply and divide Eq. (A.49) by $K_b T$,

$$\mathbf{T}_{\mathbf{m}_i^*} = \frac{K_b T}{8\pi\eta a^2 U_s} \left\{ \left[\frac{3\mu_0 m^2}{4\pi K_b T} \sum_{\substack{j=1 \\ j\neq i}}^{N} \frac{1}{r_{ij}^3} \left[-\frac{1}{3}\left(\hat{\mathbf{d}}_i \times \hat{\mathbf{d}}_j\right) + \left(\hat{\mathbf{d}}_j \cdot \hat{\mathbf{r}}_{ij}\right)\left(\hat{\mathbf{d}}_i \times \hat{\mathbf{r}}_{ij}\right) \right] \right] + \right.$$
$$\left. + \left(\frac{\mu_0 m H}{K_b T}\right) \hat{\mathbf{d}}_i \times \hat{\mathbf{H}} \right\} \quad (A.50)$$

Applying $\mathcal{D}_r = \dfrac{K_b T}{8\pi\eta a^3}$,

$$\mathbf{T}_{\mathbf{m}_i^*} = \frac{\mathcal{D}_r a}{U_s} \left\{ \left[\frac{3\mu_0 m^2}{4\pi K_b T} \sum_{\substack{j=1 \\ j\neq i}}^{N} \frac{1}{r_{ij}^3} \left[-\frac{1}{3}\left(\hat{\mathbf{d}}_i \times \hat{\mathbf{d}}_j\right) + \left(\hat{\mathbf{d}}_j \cdot \hat{\mathbf{r}}_{ij}\right)\left(\hat{\mathbf{d}}_i \times \hat{\mathbf{r}}_{ij}\right) \right] \right] + \right.$$
$$\left. + \left(\frac{\mu_0 m H}{K_b T}\right) \hat{\mathbf{d}}_i \times \hat{\mathbf{H}} \right\} \quad (A.51)$$

Substituting $\mathrm{Pe}_r = \dfrac{U_s}{\mathcal{D}_r a}$,

$$\mathbf{T}_{\mathbf{m}_i^*} = \frac{1}{\mathrm{Pe}_r} \left\{ \left[\frac{3\mu_0 m^2}{4\pi K_b T} \sum_{\substack{j=1 \\ j\neq i}}^{N} \frac{1}{r_{ij}^3} \left[-\frac{1}{3}\left(\hat{\mathbf{d}}_i \times \hat{\mathbf{d}}_j\right) + \left(\hat{\mathbf{d}}_j \cdot \hat{\mathbf{r}}_{ij}\right)\left(\hat{\mathbf{d}}_i \times \hat{\mathbf{r}}_{ij}\right) \right] \right] + \right.$$
$$\left. + \left(\frac{\mu_0 m H}{K_b T}\right) \hat{\mathbf{d}}_i \times \hat{\mathbf{H}} \right\} \quad (A.52)$$

Using the dimensionless form, $r_{ij} = a r_{ij}^*$, yields

$$\mathbf{T}_{\mathbf{m}_i^*} = \frac{1}{\mathrm{Pe}_r} \left\{ \left[\frac{3\mu_0 m^2}{4\pi K_b T} \sum_{\substack{j=1 \\ j\neq i}}^{N} \frac{1}{\left(a r_{ij}^*\right)^3} \left[-\frac{1}{3}\left(\hat{\mathbf{d}}_i \times \hat{\mathbf{d}}_j\right) + \left(\hat{\mathbf{d}}_j \cdot \hat{\mathbf{r}}_{ij}\right)\left(\hat{\mathbf{d}}_i \times \hat{\mathbf{r}}_{ij}\right) \right] \right] + \right.$$
$$\left. + \left(\frac{\mu_0 m H}{K_b T}\right) \hat{\mathbf{d}}_i \times \hat{\mathbf{H}} \right\} \quad (A.53)$$

$$\implies \mathbf{T}_{\mathbf{m}_i^*} = \frac{1}{\mathrm{Pe}_r} \left\{ \left[\frac{3\mu_0 m^2}{4\pi K_b T a^3} \sum_{\substack{j=1 \\ j\neq i}}^{N} \frac{1}{r_{ij}^{*3}} \left[-\frac{1}{3}\left(\hat{\mathbf{d}}_i \times \hat{\mathbf{d}}_j\right) + \left(\hat{\mathbf{d}}_j \cdot \hat{\mathbf{r}}_{ij}\right)\left(\hat{\mathbf{d}}_i \times \hat{\mathbf{r}}_{ij}\right) \right] \right] + \right.$$
$$\left. + \left(\frac{\mu_0 m H}{K_b T}\right) \hat{\mathbf{d}}_i \times \hat{\mathbf{H}} \right\} \quad (A.54)$$

$$\implies \mathbf{T}_{\mathbf{m}_i^*} = \frac{1}{\mathrm{Pe}_r} \left\{ \left[24\left(\frac{\mu_0 m^2}{4\pi K_b T (2a)^3}\right) \sum_{\substack{j=1 \\ j\neq i}}^{N} \frac{1}{r_{ij}^{*3}} \left[-\frac{1}{3}\left(\hat{\mathbf{d}}_i \times \hat{\mathbf{d}}_j\right) + \left(\hat{\mathbf{d}}_j \cdot \hat{\mathbf{r}}_{ij}\right)\left(\hat{\mathbf{d}}_i \times \hat{\mathbf{r}}_{ij}\right) \right] \right] + \right.$$
$$\left. + \left(\frac{\mu_0 m H}{K_b T}\right) \hat{\mathbf{d}}_i \times \hat{\mathbf{H}} \right\} \quad (A.55)$$

Applying $\alpha = \dfrac{\mu_0 m H}{K_b T}$ as the Langevin parameter and $\lambda = \dfrac{\mu_0 m^2}{4\pi K_b T \left(2a\right)^3}$ as the dipolar interaction parameter,

$$\implies \mathbf{T_{m_i}^*} = \frac{1}{\mathrm{Pe}_r}\left\{\left[24\left(\lambda\right)\sum_{\substack{j=1\\j\neq i}}^{N}\frac{1}{r_{ij}^{*\,3}}\left[-\frac{1}{3}\left(\hat{\mathbf{d}}_i\times\hat{\mathbf{d}}_j\right)+\left(\hat{\mathbf{d}}_j\cdot\hat{\mathbf{r}}_{ij}\right)\left(\hat{\mathbf{d}}_i\times\hat{\mathbf{r}}_{ij}\right)\right]\right]+\right.$$
$$\left.+\left(\alpha\right)\hat{\mathbf{d}}_i\times\hat{\mathbf{H}}\right\}\quad (A.56)$$

$$\implies \mathbf{T_{m_i}^*} = \frac{24\lambda}{\mathrm{Pe}_r}\left\{\sum_{\substack{j=1\\j\neq i}}^{N}\frac{1}{r_{ij}^{*\,3}}\left[-\frac{1}{3}\left(\hat{\mathbf{d}}_i\times\hat{\mathbf{d}}_j\right)+\left(\hat{\mathbf{d}}_j\cdot\hat{\mathbf{r}}_{ij}\right)\left(\hat{\mathbf{d}}_i\times\hat{\mathbf{r}}_{ij}\right)\right]\right\}+$$
$$+\frac{\alpha}{\mathrm{Pe}_r}\left(\hat{\mathbf{d}}_i\times\hat{\mathbf{H}}\right)\quad (A.57)$$